

TSUNAMI MAXIMUM RUNUP AND FOCUSING THROUGH EARTHQUAKE  
SOURCE PARAMETERS

A THESIS SUBMITTED TO  
THE GRADUATE SCHOOL OF NATURAL AND APPLIED SCIENCES  
OF  
MIDDLE EAST TECHNICAL UNIVERSITY

BY

NAEIMEH SHARGHIVAND

IN PARTIAL FULFILLMENT OF THE REQUIREMENTS  
FOR  
THE DEGREE OF DOCTOR OF PHILOSOPHY  
IN  
ENGINEERING SCIENCES

AUGUST 2022



Approval of the thesis:

**TSUNAMI MAXIMUM RUNUP AND FOCUSING THROUGH  
EARTHQUAKE SOURCE PARAMETERS**

submitted by **NAEIMEH SHARGHIVAND** in partial fulfillment of the requirements  
for the degree of **Doctor of Philosophy in Engineering Sciences Department,**  
**Middle East Technical University** by,

Prof. Dr. Halil Kalıpçılar  
Dean, Graduate School of **Natural and Applied Sciences**

\_\_\_\_\_

Prof. Dr. Murat Dicleli  
Head of Department, **Engineering Sciences**

\_\_\_\_\_

Prof. Dr. Mehmet Zülfü Aşık  
Supervisor, **Engineering Sciences Dept., METU**

\_\_\_\_\_

**Examining Committee Members:**

Prof. Dr. Ahmet Cevdet Yalçın  
Civil Engineering Dept., METU

\_\_\_\_\_

Prof. Dr. Mehmet Zülfü Aşık  
Engineering Sciences Dept., METU

\_\_\_\_\_

Assist. Prof. Dr. Senih Gürses  
Engineering Sciences Dept., METU

\_\_\_\_\_

Prof. Dr. Utku Kânoğlu  
Aerospace Engineering Dept., DEU

\_\_\_\_\_

Assist. Prof. Dr. Baran Aydın  
Civil Engineering Dept., ATU

\_\_\_\_\_

Date: 11.08.2022

**I hereby declare that all information in this document has been obtained and presented in accordance with academic rules and ethical conduct. I also declare that, as required by these rules and conduct, I have fully cited and referenced all material and results that are not original to this work.**

Name, Surname: Naeimeh Sharghivand

Signature :

## **ABSTRACT**

### **TSUNAMI MAXIMUM RUNUP AND FOCUSING THROUGH EARTHQUAKE SOURCE PARAMETERS**

Sharghivand, Naeimeh

Ph.D., Department of Engineering Sciences

Supervisor: Prof. Dr. Mehmet Zülfü Aşık

August 2022, 85 pages

In this study, the *N*-wave profile is fitted to the seafloor deformation for a large set of earthquake scenarios, i.e., assuming that the seafloor deformation resulting from an earthquake instantaneously transfers to the sea surface. Hence, the *N*-wave parameters are identified with respect to the earthquake source parameters allowing to express the initial tsunami profile in terms of the earthquake source parameters. Then, the maximum tsunami runup is presented through the earthquake fault plane parameters using the maximum runup formula. The results are tested against field runup measurements for several events observing good agreement. Then, propagating the finite crest length initial profile defined using earthquake source parameters, the tsunami focusing –abnormal wave height in the leading depression side of an *N*-wave– is related to the earthquake source parameters. A tsunami can be much more hazardous for the target coastline when the focusing point is close to the shorelines. The results presented here can help better understand the unusual observations witnessed in the fields.

Keywords: *N-wave, Earthquake source parameters, Rapid tsunami runup forecast, Tsunami early warning, Tsunami Focusing, Tsunami amplification*

## ÖZ

### DEPREM KAYNAK PARAMETRELERİ İLE TSUNAMİ RUNUP VE ODAKLANMA TAHMİNİ

Sharghivand, Naeimeh

Doktora, Mühendislik Bilimleri Bölümü

Tez Yöneticisi: Prof. Dr. Mehmet Zülfü Aşık

Ağustos 2022 , 85 sayfa

Bu çalışmada, depremden kaynaklanan deniz tabanı deformasyonunun anında deniz yüzeyine aktarıldığı varsayılarak, geniş bir deprem senaryosu seti için  $N$ -dalga profili deniz tabanı deformasyonuna uydurulmuştur. Dolayısıyla,  $N$ -dalgası parametreleri deprem kaynağı parametreleri cinsinden belirlenerek başlangıç tsunami profilini ifade etmekte kullanılmıştır. Ardından, maksimum tsunami tırmanma formülü kullanılarak, maksimum tsunami tırmanması deprem fay parametreleri ile sunulmuştur. Sonuçların, tsunami saha çalışma ölçümlerine karşı test edilerek, arazi tsunami tırmanma verileri ile uyum içerisinde olduğu gözlenmiştir. Daha sonra, deprem kaynağı parametreleri kullanılarak tanımlanan sonlu uzunluktaki tsunami başlangıç profilinin yayılması, tsunami odaklaması – $N$ -dalgasının çöküntü tarafındaki anormal dalga yüksekliği– deprem kaynağı parametreleriyle ilişkilendirilmiştir. Odak noktası kıyı şeridine yakın olduğunda, tsunami hedef kıyı şeridi için çok daha tehlikeli olacaktır. Burada sunulan sonuçlar, tanık olunan olağandışı gözlemlerin daha iyi anlaşılmasına yardımcı olabilir.

Anahtar Kelimeler: *N-dalgası, Deprem kaynak parametreleri, Hızlı tsunami runup tahmini, Erken tsunami uyarısı, Tsunami Odaklanması, Tsunami amplifikasyonu*



*To Ramez and my mother....*

## ACKNOWLEDGMENTS

I would like to express my sincere gratitude to my supervisor, Prof. Dr. Utku Kânoğlu for his invaluable support, guidance, and insightful comments. I also would like to extend my deepest gratitude to Prof. Dr. Mehmet Zülfü Aşık who has supported me with valuable knowledge and guidance since the beginning of my thesis monitoring and evaluation committee in 2018. During the last semester of my Ph.D. study, Prof. Dr. Utku Kânoğlu started a new position at Dokuz Eylül University and was not officially able to supervise. Prof. Dr. Mehmet Zülfü Aşık stepped in and endorsed to supervise me alongside with supervision of Prof. Dr. Utku Kânoğlu during the last steps of my study. I thank Prof. Dr. Mehmet Zülfü Aşık for stepping in.

My deepest gratitude also goes to Prof. Dr. Ahmet Cevdet Yalçın, who always supported me whenever I faced challenges and strengthened me during my studies with his invaluable advice and motivation.

I am beyond thankful to Assist. Prof. Dr. Baran Aydın for all his contribution and continuous support. His valuable guidance brightened my way of moving forward.

Besides, as an examining committee member, I would like to thank Assist. Prof. Dr. Senih Gürses for his valuable time participating in my thesis defense.

I would like to express my gratitude to my former employer Dolfen Consulting Engineering family and colleagues especially to Ms. Yasemin Özgen and Dr. Işıkhan Güler, for their continuous support and encouragement during this study. It was a valuable opportunity to be a part of your team. I also extend my thanks to my office-mate Zergün Fenerci for her friendship and for sharing all the busy days, success, and joys.

I would like to extend my special thanks to Gözde Güney Doğan Bingöl and Cem Bingöl for their support and invaluable friendship, who were always there for me. We shared many delightful times and were always together in any challenging time.

I would like to express my gratitude to Elmira Pourreza and Vahid Berenji for all their valuable support and friendship. I am grateful that we always shared both critical times and joys.

I would like to thank Serkan Özen for his valuable friendship and continuous support since the beginning of our graduate study in 2011.

I would like to extend my special thanks to Fatemeh Asoudeh, who has always been my intimate friend and always been there for me no matter how far apart we are.

I would like to thank Bora Yalçiner, Hasan Gökhan Güler, Ebru Kirezci, Çağıl Kirezci, Ayşe Duha Metin, and Denizcan Aydın for their valuable friendship. Even though now we are scattered around the world, we have gathered good memories on the long journey of this study.

I am thankful to my brothers Amir, Behrouz, and Hadi Sharghivand and their beloved families for all their love and support. My special thanks also go to my sweet and lovely nephews.

I would like to express my gratitude to my dear extended family Homa, Ali, and Sevin Mohammadi for their support, understanding, and kindness.

I would like to offer my heartfelt thanks to my mother, Azam Sabounpaz, who has always supported and loved me in every moment of my life. Her pure and unconditional love was always my source of strength during this study and during every challenging time of my life. I would never survive without her love.

I would like to extend my deepest heartfelt gratitude to my husband, Ramez Mohammadi, who was always by my side in this long journey, at the beginning as a supportive and trustworthy friend and at the end of the study as my life. We shared many joyful times as friends, especially playing billiard and dart. As a husband, he was again by my side, this time, at any moment and under any circumstances. In the middle of all the challenging times, when I was near to getting disappointed, he always strengthened me, pushed me to think positively, and was the reason for my peace. I am grateful for all his patience, support, encouragement, and love. This study would not be possible without you.

## TABLE OF CONTENTS

ABSTRACT . . . . .	v
ÖZ . . . . .	vii
ACKNOWLEDGMENTS . . . . .	x
TABLE OF CONTENTS . . . . .	xii
LIST OF TABLES . . . . .	xiv
LIST OF FIGURES . . . . .	xv
CHAPTERS	
1 INTRODUCTION . . . . .	1
2 TSUNAMI INITIAL PROFILE AND MAXIMUM RUNUP THROUGH EARTHQUAKE SOURCE PARAMETERS . . . . .	9
2.1 <i>N</i> -wave through Earthquake Source Parameters . . . . .	10
2.1.1 Scaling parameter, $\varepsilon_{1D}$ . . . . .	12
2.1.2 Off-shore wave amplitude, $H$ . . . . .	14
2.1.3 Distance $X_2 - X_1$ . . . . .	17
2.1.4 Steepness parameter, $p_0$ . . . . .	21
2.2 Maximum Runup through Earthquake Source Parameters . . . . .	25
2.3 Field Validation . . . . .	27
3 IMPACTS OF EARTHQUAKE SOURCE PARAMETERS ON TSUNAMI FOCUSING . . . . .	33

3.1	Review of Analytical Solution . . . . .	37
3.2	Two-dimensional $N$ -wave through Earthquake Source Parameters . .	39
3.3	Earthquake Source Scenarios . . . . .	39
3.4	Results and Discussions . . . . .	41
3.4.1	Focusing through the slip amount . . . . .	42
3.4.2	Focusing through the fault depth . . . . .	45
3.4.3	Focusing through the dip angle . . . . .	52
3.4.4	Focusing through the fault length . . . . .	58
3.4.5	Focusing through the fault width . . . . .	62
3.4.6	Focusing through the tsunami aspect ratio . . . . .	66
4	CONCLUSIONS . . . . .	69
	REFERENCES . . . . .	71
	CURRICULUM VITAE . . . . .	81

## LIST OF TABLES

### TABLES

Table 2.1	Range of earthquake source scenarios used in fitting database. . . . .	11
Table 2.2	The source parameters and beach slopes used for the events. Here, $M_w$ , $u$ , $W$ , $d$ , and $\delta$ indicate the moment magnitude, the slip amount, the fault width, the fault depth, and the dip angle, respectively; $\tan \beta$ represents the nearshore beach slope and $h$ is the ocean depth. $R_{REP}$ is calculated using Eq. 2.25 and $R_{Mean}$ and $R_{Ext}$ show the mean and extreme field runup measurements for the events. . . . .	31
Table 3.1	Range of earthquake source scenarios used in propagation database.	40

## LIST OF FIGURES

### FIGURES

Figure 2.1	Definition sketch for the fault plane parameters: $\phi$ , $\lambda$ , and $\delta$ are the strike, the rake, and the dip angles, respectively; $L$ , $W$ , $d$ , and $u$ are the fault length, the fault width, the fault depth, and the fault slip amount, respectively. . . . .	10
Figure 2.2	Definition sketch for the canonical problem and $N$ -wave parameters. . . . .	11
Figure 2.3	Examples of $\varepsilon_{1D}$ and fault depth relationships for different fault widths and dip angles; and corresponding regression lines. . . . .	13
Figure 2.4	Examples of $a_1(W, \delta)$ and $a_2(W, \delta)$ relationships with fault width for different dip angles; and corresponding regression lines. . . . .	14
Figure 2.5	Relationships of $a_3(\delta)$ to $a_6(\delta)$ with dip angle; and corresponding regression lines. . . . .	15
Figure 2.6	Examples of $H$ and fault depth relationships for different fault widths and dip angles; and corresponding regression lines. . . . .	16
Figure 2.7	Examples of $b_1(W, \delta)$ and $b_2(W, \delta)$ relationships with fault width for different dip angles; and corresponding regression lines. . . . .	17
Figure 2.8	Relationships of $b_3(\delta)$ to $b_6(\delta)$ with dip angle; and corresponding regression lines. . . . .	18
Figure 2.9	Examples of $X_2$ and fault depth relationships for different fault widths and dip angles; and corresponding regression lines. . . . .	19

Figure 2.10	Examples of $c_1(W, \delta)$ and $c_2(W, \delta)$ relationships with fault width for different dip angles; and corresponding regression lines. . . . .	20
Figure 2.11	Relationships of $c_3(\delta)$ to $c_6(\delta)$ with dip angle and corresponding regression lines. . . . .	20
Figure 2.12	Examples of $p_0$ and fault depth relationships for different fault widths and dip angles; and corresponding regression lines. . . . .	22
Figure 2.13	Examples of $a_1(W, \delta)$ and $a_2(W, \delta)$ relationships with fault width for different dip angles; and corresponding regression lines. . . . .	22
Figure 2.14	Relationships of $k_3(\delta)$ to $k_6(\delta)$ with dip angle; and corresponding regression lines. . . . .	23
Figure 2.15	An example of two-dimensional NEP profile (blue solid line) compared with the individually fitted $N$ -wave profile (red dashed line) and Okada (1985)'s displacement model (black solid line) using the submarine earthquake source as $L = 200$ km, $W = 50$ km, $d = 40$ km, $u = 10$ m, $\delta = 20^\circ$ , $\lambda = 90^\circ$ , and $\phi = 270^\circ$ . The Root Mean Squared Errors (RMSEs) between NEP and Okada profiles from top to bottom are calculated as 0.26 m, 0.13 m, and 0.02 m, respectively. . . . .	24
Figure 2.16	Comparison of runup estimates calculated using REP (Eq. 2.25) with those calculated using the parameters in fitting database. The earthquake source scenarios are defined by varying parameters as $W = 20, 50, 100$ , and $150$ km, $d = 10, 20, 30$ and $40$ km, $u = 1, 5$ , and $10$ m, $\delta = 10$ to $30^\circ$ with $5^\circ$ increments, and the beach slope of $1/20$ . . . . .	26
Figure 2.17	Leading depression initial waveform through NEP and Okada (1985) for (a) Nicaragua 1992; (b) Indonesia, Java 1994; (c) Mexico, Colima 1995; (d) Sumatra 2004; (e) Chile, Maule 2010; (f) Japan, Tohoku 2011; and (g) Aegean Sea, Türkiye 2020. The fault plane parameters for the events and references are given in Table 2.2. . . . .	29



Figure 2.18	Comparison of runup values calculated using REP (Eq. 2.25) with mean (not-filled symbols) and extreme (filled symbols) field runup measurements. The fault plane parameters for the events and references are given in Table 2.2. . . . .	30
Figure 3.1	Evolution and focusing of a finite-crested $N$ -wave profile; (a) initial wave, (b,c) evolution, and (d) focusing. After Kânoğlu et al. (2013). . . . .	35
Figure 3.2	Location of the focusing point $F$ for an $N$ -wave-type initial surface displacement. After Marchuk & Titov (1989). . . . .	36
Figure 3.3	Definition of the focusing parameters: $\tilde{\eta}_f$ : dimensionless focusing amplitude and $ \tilde{x}_f $ : dimensionless focusing distance. Dashed and solid lines indicate an example of the initial tsunami wave and maximum wave envelope along the bisector, respectively. The earthquake source parameters are: $\phi = 270^\circ$ , $\lambda = 90^\circ$ , $\delta = 15^\circ$ , $u = 10$ m, $L = 200$ km, $W = 50$ km, and $d = 20$ km. . . . .	36
Figure 3.4	Relation of the focusing amplitude to the slip amount. The fault length is $L = 300$ km and the fault depth is $d = 20$ km. . . . .	43
Figure 3.5	Relation of the focusing amplitude to the slip amount. The fault length is $L = 300$ km and the fault depth is $d = 40$ km. . . . .	43
Figure 3.6	Relation of the focusing distance to the slip amount. The fault length is $L = 300$ km and the fault depth is $d = 20$ km. . . . .	44
Figure 3.7	Relation of the focusing distance to the slip amount. The fault length is $L = 300$ km and the fault depth is $d = 40$ km. . . . .	44
Figure 3.8	Relation of the focusing amplitude to the fault depth. The fault length is $L = 100$ km and the slip amount $u = 10$ m. . . . .	45
Figure 3.9	Relation of the focusing amplitude to the fault depth. The fault length is $L = 200$ km and the slip amount $u = 10$ m. . . . .	46

Figure 3.10	Relation of the focusing amplitude to the fault depth. The fault length is $L = 300$ km and the slip amount $u = 10$ m. . . . .	46
Figure 3.11	Relation of the focusing amplitude to the fault depth. The fault length is $L = 400$ km and the slip amount $u = 10$ m. . . . .	47
Figure 3.12	Relation of the focusing amplitude to the fault depth. The fault length is $L = 500$ km and the slip amount $u = 10$ m. . . . .	47
Figure 3.13	Relation of the focusing amplitude to the fault depth. The dip angle is $\delta = 15^\circ$ , and the slip amount $u = 10$ m. . . . .	48
Figure 3.14	Relation of the focusing distance to the fault depth. The fault length is $L = 100$ km and the slip amount $u = 10$ m. . . . .	48
Figure 3.15	Relation of the focusing distance to the fault depth. The fault length is $L = 200$ km and the slip amount $u = 10$ m. . . . .	49
Figure 3.16	Relation of the focusing distance to the fault depth. The fault length is $L = 300$ km and the slip amount $u = 10$ m. . . . .	49
Figure 3.17	Relation of the focusing distance to the fault depth. The fault length is $L = 400$ km and the slip amount $u = 10$ m. . . . .	50
Figure 3.18	Relation of the focusing distance to the fault depth. The fault length is $L = 500$ km and the slip amount $u = 10$ m. . . . .	50
Figure 3.19	Relation of the focusing distance to the fault depth. The dip angle is $\delta = 15^\circ$ , and the slip amount $u = 10$ m. . . . .	51
Figure 3.20	Relation of the focusing amplitude to the dip angle. The fault length is $L = 100$ km and the slip amount $u = 10$ m. . . . .	52
Figure 3.21	Relation of the focusing amplitude to the dip angle. The fault length is $L = 200$ km and the slip amount $u = 10$ m. . . . .	53
Figure 3.22	Relation of the focusing amplitude to the dip angle. The fault length is $L = 300$ km and the slip amount $u = 10$ m. . . . .	53

Figure 3.23	Relation of the focusing amplitude to the dip angle. The fault length is $L = 400$ km and the slip amount $u = 10$ m. . . . .	54
Figure 3.24	Relation of the focusing amplitude to the dip angle. The fault length is $L = 500$ km and the slip amount $u = 10$ m. . . . .	54
Figure 3.25	Relation of the focusing amplitude to the dip angle. The fault width is $W = 100$ km, the fault depth is $d = 20$ km and the slip amount $u = 10$ m. . . . .	55
Figure 3.26	Relation of the focusing distance to the dip angle. The fault length is $L = 100$ km and the slip amount $u = 10$ m. . . . .	55
Figure 3.27	Relation of the focusing distance to the dip angle. The fault length is $L = 200$ km and the slip amount $u = 10$ m. . . . .	56
Figure 3.28	Relation of the focusing distance to the dip angle. The fault length is $L = 300$ km and the slip amount $u = 10$ m. . . . .	56
Figure 3.29	Relation of the focusing distance to the dip angle. The fault length is $L = 400$ km and the slip amount $u = 10$ m. . . . .	57
Figure 3.30	Relation of the focusing distance to the dip angle. The fault length is $L = 500$ km and the slip amount $u = 10$ m. . . . .	57
Figure 3.31	Relation of the focusing distance to the dip angle. The fault width is $W = 100$ km, the fault depth is $d = 20$ km, and the slip amount $u = 10$ m. . . . .	58
Figure 3.32	Relation of the focusing amplitude to the fault length. The fault width is $W = 50$ km and the slip amount $u = 10$ m. . . . .	59
Figure 3.33	Relation of the focusing amplitude to the fault length. The fault width is $W = 100$ km and the slip amount $u = 10$ m. . . . .	59
Figure 3.34	Relation of the focusing amplitude to the fault length. The fault width is $W = 150$ km and the slip amount $u = 10$ m. . . . .	60

Figure 3.35	Relation of the focusing distance to the fault length. The fault width is $W = 50$ km and the slip amount $u = 10$ m. . . . .	60
Figure 3.36	Relation of the focusing distance to the fault length. The fault width is $W = 100$ km and the slip amount $u = 10$ m. . . . .	61
Figure 3.37	Relation of the focusing distance to the fault length. The fault width is $W = 150$ km and the slip amount $u = 10$ m. . . . .	61
Figure 3.38	Relation of the focusing amplitude to the fault width. The fault length is $L = 200$ km and the slip amount $u = 10$ m. . . . .	62
Figure 3.39	Relation of the focusing amplitude to the fault width. The fault length is $L = 300$ km and the slip amount $u = 10$ m. . . . .	63
Figure 3.40	Relation of the focusing amplitude to the fault width. The fault length is $L = 400$ km and the slip amount $u = 10$ m. . . . .	63
Figure 3.41	Relation of the focusing amplitude to the fault width. The fault length is $L = 500$ km and the slip amount $u = 10$ m. . . . .	64
Figure 3.42	Relation of the focusing distance to the fault width. The fault length is $L = 200$ km and the slip amount $u = 10$ m. . . . .	64
Figure 3.43	Relation of the focusing distance to the fault width. The fault length is $L = 300$ km and the slip amount $u = 10$ m. . . . .	65
Figure 3.44	Relation of the focusing distance to the fault width. The fault length is $L = 400$ km and the slip amount $u = 10$ m. . . . .	65
Figure 3.45	Relation of the focusing distance to the fault width. The fault length is $L = 500$ km and the slip amount $u = 10$ m. . . . .	66
Figure 3.46	Relation of the focusing amplitude to the tsunami aspect ratio. The solid, dashed, and dotted lines indicate results for $\delta = 10^\circ$ , $20^\circ$ , and $30^\circ$ , respectively. The slip amount $u = 10$ m. . . . .	67

Figure 3.47 Relation of the focusing distance to the tsunami aspect ratio. The solid, dashed, and dotted lines indicate results for  $\delta = 10, 20$ , and  $30^\circ$ , respectively. The slip amount  $u = 10$  m. . . . . 67



## CHAPTER 1

### INTRODUCTION

Tsunamis are one of the most potent sources of natural catastrophes. As a Japanese word, tsunami means *harbor (tsu) wave (nami)*; eyewitnesses' early observations of these unusual waves had probably been near the coastal areas, e.g., harbors and ports, hence the name. The historical records of tsunami waves in Japan have existed since the 9th Century AD. Tsunamis, a series of long waves also known as shallow water-waves, are surface gravity waves propagating across the ocean with a wavelength ( $l$ ) much larger than the ocean's depth ( $h$ ), i.e.,  $l \gg h$ . Their evolution process can be divided into three main phases: generation, propagation, and runup or inundation. A tsunami as a massive water wave is generated by large-scale short-duration impulsive energy transfer to the entire sea column, mainly triggered by underwater earthquakes, submarine or subaerial landslides, and less commonly by volcanic eruptions and asteroid impacts. Gusiakov (2009) categorized the source origins of historical tsunamis, where tectonic origin, i.e., earthquake-generated tsunamis, were up to 75%, landslide 10%, volcanic eruptions 4%, and meteorological sources 3% of the tsunamis origins. "Up to 8% of all the reported historical runups still have unidentified sources," Gusiakov (2009) stated.

Characteristics of tsunami waves with small steepness can make them barely detectable by naked eyes in the open ocean. However, as they approach the shorelines with shallower water depth, wave shoaling is initiated, forcing a significant increase in tsunami amplitude and decrease in wavelength, making the waves steeper and slowing down the waves in accordance with shallow water-wave speed,  $c = \sqrt{gh}$ , where  $g$  is the gravitational acceleration.

Tsunamis can be high-impact, long-duration catastrophes, often with multiple dev-

astating waves penetrating target shorelines (Kânoğlu et al. 2015). Once a tsunami is generated, waves can travel at a speed of 800 km/h, crossing the entire ocean in a day or less. They may lead to coastal inundation in both near- and far-field, e.g. the energy propagation maps of the 26 December 2004 Sumatra tsunami (Titov et al. 2005) and the 11 March 2011 Japan tsunami (Tang et al. 2012).

After the 26 December 2004 Indian Ocean (Boxing Day) tsunami resulted from an  $M_w$  9.3 earthquake (Stein & Okal 2005), nations with potential tsunami threats started to develop tsunami forecasting capabilities, and the word tsunami made its entrance in most languages. The Boxing day tsunami was the deadliest tsunami in recorded history which caused more than 200,000 casualties across the Indian Ocean shorelines. The number of victims was above 160,000 in Indonesia, 35,000 in Sri Lanka, 16,000 in India and 8,300 in Thailand (Tsuji et al. 2006). The catastrophic tragedy has been screened in the drama movie *The Impossible* in 2012. The movie shows the true story of a Spanish tourist Dr. María Belón and her family in Thailand caught in the devastating aftermath of the 2004 Indian Ocean tsunami. The Boxing Day tsunami impacted at least 16 countries, including tourists from many other countries (Synolakis & Kong, 2006). Four hundred twenty-eight Swedish people out of about ten million population were among the casualties. Post-tsunami field surveys were conducted by different international teams of scientists to document the damage metrics, e.g., flow depth, inundation, and runup (Borrero et al. 2006; Jaffe et al. 2006; Tsuji et al. 2006). Borrero et al. (2006)'s measurements in northern Sumatra in the region around Banda Aceh reveal the runup variations between a minimum of 2.5 and a maximum of 31 m.

The magnitude  $M_w$  9.1, 11 March 2011 (the Great East Japan Earthquake) was one of the most powerful earthquakes recorded in the past 100 years. The quake shock lasts for six minutes. A half-hour later, a massive tsunami penetrated over 650 km of the Japanese coastline, overtopping sea walls and other coastal defense structures, flooding through more than 500 km<sup>2</sup> of land causing entire towns and villages to be washed away. Even though Japan was thought to be the most tsunami-ready country globally, they were not as prepared as the world estimated for such a giant catastrophe causing 15,883 fatalities and 2,654 missing in northeastern Japan (Bestor 2013). The 2011 Japan tsunami dramatically revealed that all the efforts after the Boxing Day



event did not lead to "a world that can coexist with a tsunami hazard," as stated in Synolakis & Bernard (2006). According to the field measurements, the maximum runup heights larger than 10 and 20 m were measured along 425 and 290 km of the Japanese coastline (Mori et al. 2011). The runup height reached 16.4 and 20.8 m at 30 and 40 km from the nuclear power plant, and the maximum runup height of 39.7 m was measured at Aneyoshi, Miyako (Mori et al. 2011). The Fukushima, Iwate, and Miyagi prefectures were the worst-hit areas. The Fukushima Dai-ichi nuclear power plant (NPP) accident was the third most severe accident in an NPP ever. Synolakis & Kânoğlu (2015) elucidated how the engineering and regulatory failures resulted in the Fukushima disaster.

Tsunamis are not only threats to the countries in whose territories they originate. They can cause devastation locally and across national boundaries. This was again shown dramatically by the 2011 Japan event, i.e., nuclear accident, harbor oscillations which could persist for hours (Lynett et al. 2012), and debris flows (Lebreton & Borrero 2013).

Emanated dramatic observation from the past tsunami disasters has always proved the importance of the time factor, especially in the nearshore tsunami warning and forecasting. The arrival time of the tsunami at the nearest coastline has always been very short. Hence, it is crucial to provide a reliable warning within minutes of the event. At present, most of the near- and far-field tsunami forecast models employ tsunami numerical models (Zaytsev et al. 2019; Titov et al. 2016; Miranda et al. 2014; Tinti & Tonini 2013; Liu et al. 1998; Imamura & Imteaz 1995). Besides, the probabilistic tsunami hazard assessment (PTHA) is used to estimate tsunami hazard potential on a nationwide or global scale (Behrens et al. 2022; Grezio et al. 2017; González et al. 2009). The preparation of numerical models requires time and resources to provide models input data, e.g., high-resolution geospatial data. In addition to the high-resolution bathymetric and topographic data, if a high-performance computing (HPC) cluster is not accessible in real-time computing, numerical modeling in forecasting nearshore tsunamis might not be effective. However, numerical simulation and PTHA can be beneficial in providing tsunami hazard maps (Davies & Griffin 2019; Schlurmann et al. 2010; González et al. 2009; Walsh et al. 2004) and estimating tsunami hazard potential for at-risk communities (Aydın et al. 2020;

Yalçiner et al. 2019; Sepúlveda et al. 2019; Lynett et al. 2017; Harbitz et al. 2016; Sharghivand 2014), which can be used in pre-hazard action planning. Alongside the numerical models and PTHA, the amplification factor (AF) method, i.e., relating the offshore wave height to the maximum inundation height, is used to faster estimates the tsunami height (Glimsdal et al. 2019; Løvholt et al. 2016; Baba et al. 2014; Løvholt et al. 2012).

In terms of studies relating earthquake source parameters to tsunami maximum runup, Okal & Synolakis (2004) used a data set of 72 models of nearshore seismic dislocations and landslide sources and performed tsunami numerical simulations. They varied fault parameters one by one and presented their individual influence on tsunami runup height. However, their main goal was to establish source discriminant to identify landslide and earthquake-generated events.

The other study proposed by Sepúlveda & Liu (2016) offers two relationships between the tsunami runup height and seismic parameters for two types of problems. The study implemented Carrier & Greenspan (1958)'s solution to provide analytical relationships for shoreline motion and evaluated shoreline quantities for boundary-value-problem (BVP) through Madsen & Schäffer (2010) and for initial-value-problem (IVP) through Kânoğlu (2004). The approach was applied to the 2004 Sumatra and 2010 Chile tsunamis.

In a most recent study, Wronna et al. (2021) defined a new parameter called tsunami runup predictor (TRP) and proposed relationships between the TRP and maximum runup values for leading elevation and leading depression *N*-waves. They developed the initial tsunami waveforms (ITWs) using the half-space elastic theory (Mansinha & Smylie 1971) for different scenarios by adjusting the fault plane parameters: dip angle, fault width, fault depth, and slip amount and also by varying the source distance to the shore and the beach slope. Then, they used numerical (Miranda & Luis 2019) and analytical (Aydın & Kânoğlu 2017) methods to calculate tsunami runup on constant beach slopes. Wronna et al. (2021) concluded the study by comparing the TRP runup estimates to the field measurements of several past tsunami events and obtained good agreements.

A high number of tsunami events were registered from 1990 to 2000; accordingly,

the decade was named as tsunami decade (Synolakis & Bernard 2006). At least six significant tsunamis were reported between 1992 and 1994, e.g., 1 September 1992 Nicaragua; 12 December 1992 Flores Island, Indonesia; 12 July 1993 Hokkaido-Nansei-Oki, Japan; 2 June 1994 East Java, Indonesia; 2 October 1994 Kuril Islands, Russia; and 11 November 1994 Mindoro Island, Philippines. During the field surveys of the events conducted by International Tsunami Survey Teams (ITSTs), nearly all eyewitnesses reported shoreline recession before waves advanced up the coasts. These events resulted in a paradigm shift from a solitary wave to an  $N$ -wave as a more realistic initial waveform of tsunamis. Consequently, Tadeballi & Synolakis (1994) proposed a class of elevation-depression waves, called  $N$ -waves, to define the initial waveform of tsunamis. After Tadeballi & Synolakis (1994)'s introduction to  $N$ -wave as a realistic initial waveform of incoming tsunamis, it took several events for the community to accept it (Madsen & Schäffer 2010). Nonetheless, Tadeballi & Synolakis (1996) incorporated a steepness parameter as a horizontal length scale and proved  $N$ -wave stability as a geophysically realistic model for long wave propagation.

In seeking to expose a more expeditious real-time forecasting, this study comes up with a new approach to extract the initial tsunami profile and maximum runup for a simplified beach geometry in terms of earthquake source parameters. Here, first, using regression analysis, the generalized  $N$ -wave profile (Tadeballi & Synolakis 1996) is related to the tsunami initial profile calculated through Okada's linear elastic dislocation model (Okada 1985) and  $N$ -wave parameters are identified in terms of the earthquake source parameters for a large fault plane database. Regression analysis is an effective statistical curve fitting technique used to predict the relationship between one or more independent variables and one dependent variable. Today, the technique is widely used in data science and machine learning to predict the best-fit results in advanced research, e.g., natural hazards, economics, medicine, etc.

Tadeballi & Synolakis (1996) presented maximum runup for the canonical problem<sup>1</sup> for an  $N$ -wave type initial condition; here, tsunami maximum runup is related to the earthquake source parameters through their maximum runup formulation. The preliminary results were presented in Sharghivand & Kânoğlu (2017 2016).

---

<sup>1</sup> Wave propagation over a constant depth first and then sloping beach.

Two critical factors can influence the directivity of tsunami energy radiation and initiate geometrical focusing of tsunami waves: the bathymetric features of the ocean bottom and the source configuration.

Berry (2007) used the diffraction theory and showed the underwater features, e.g., trenches' and seamounts' role in the focus of tsunami energy. He demonstrated that shallower regions in the ocean, such as seamounts, can behave as lenses and concentrate tsunami energy, potentially multiplying that 10-fold over a transverse range of tens of kilometers, causing significant local amplifications.

Ben-Menahem (1961) analyzed the radiation of seismic surface waves from finite sources and represented that the finite length of the source plays an important role in wave propagation patterns. He showed that the azimuthal scattering of waves amplitudes depends highly on the dimensions of the source. Ben-Menahem & Rosenman (1972) further calculated the radiation pattern from a submarine source using linear theory and expressed that tsunami energy propagates mainly in a direction normal to the fault rupture. Later on, Okal (2003) determined differences in directivity patterns between earthquake- and landslide-generated tsunamis.

The *N*-wave initial waveform shows specific features which might enhance maximum runup at a target coastline, referred to as tsunami focusing<sup>2</sup>.

Dotsenko et al. (1986) employed the two-dimensional linear wave theory and showed that wave energy amplification might depend on whether the initial condition has a dipolar shape. Later, the existence of a focusing point<sup>3</sup> for a finite crest length *N*-wave-type initial condition was proposed by Marchuk & Titov (1989). Their numerical studies demonstrated that the focusing point stays somewhere on a straight line coming through the centers of both depression and elevation part of the initial wave. Kânoğlu et al. (2013) considered two-dimensional propagation of an *N*-wave type initial condition with finite crest length over a flat bottom and showed that focusing effect of an *N*-wave in the direction of leading depression can enhance the runup. They studied tsunami focusing using linear non-dispersive (Aydın 2011) and linear dispersive (Kervella et al. 2007) theories analytically and nonlinear non-dispersive

---

<sup>2</sup> An unexpected wave amplification in the direction of depression side of an *N*-wave.

<sup>3</sup> A point in the leading depression side of an *N*-wave where abnormal wave amplitude is registered.

(Titov et al. 2011) and weakly nonlinear weakly dispersive (Zhou et al. 2011) theories numerically. Their study exposes the existence of the focusing point in tsunami evolution using all four approaches. Kânoğlu et al. (2013) referred to the focusing as a possible explanation for unusual high runup observations of the 17 July 1998 Papua New Guinea; the 17 July 2006 Java, Indonesia; and the 11 March 2011 Japan tsunamis. Further, Kanoglu (2016)’s preliminary results suggested that later waves could be higher on the leading depression side for an  $N$ -wave, i.e., sequencing defined by Okal & Synolakis (2016) is more pronounced on the leading depression side for dispersive wave propagation. Thereon, Aydın (2018) explored how the variation in the initial wave’s geometric parameters, e.g., wave steepness and crest length, can adjust the focusing amplitude and location of the focusing point by comparing the maximum wave envelopes for different initial profiles. He used the linear shallow water theory and showed that the maximum wave amplitude increases substantially with the initial wave crest length for mild initial waves, i.e., waves with small steepness; however, the location of the focusing point stays almost invariant. While, the focusing point dislocates significantly for steep initial waves, i.e., waves with large steepness, although it causes a slight increase in the wave maximum.

Here, the study’s second objective is to put a new perspective on tsunami focusing by relating it directly to the earthquake source parameters and exploring their impacts on tsunami focusing. Hence, the study examines how the focusing amplitude<sup>4</sup> and location of the focusing point can vary due to different source configurations.

In summary, first, the one- and two-dimensional generalized  $N$ -wave profiles and maximum runup equation are defined in terms of earthquake source parameters, i.e.,  $N$ -wave through Earthquake Parameters (NEP) and Runup through Earthquake Parameters (REP), respectively. Then, using the linear shallow water-wave theory, a propagation database is developed for a set of two-dimensional finite crest length NEP profiles to investigate the influences of the earthquake source parameters on tsunami focusing. Hence, the impacts of fault plane parameters in the variation of location and amplitude of focusing point are studied.

---

<sup>4</sup> The maximum wave amplitude at the location of the focusing point.



## CHAPTER 2

### TSUNAMI INITIAL PROFILE AND MAXIMUM RUNUP THROUGH EARTHQUAKE SOURCE PARAMETERS

Tsunamis generated by submarine earthquakes have a finite crest length, and their initial waveform is calculable from estimates of the seismic parameters through Okada (1985)'s seafloor deformation. In practice, seafloor deformation is transferred to the sea surface, assuming that the deformation takes place instantaneously. Okada's linear dislocation model enables to calculate sea bottom deformation using a set of seismic parameters, i.e., seismic moment ( $M_0$ ), fault length ( $L$ ), fault width ( $W$ ), fault depth ( $d$ ), fault slip amount ( $u$ ), dip angle ( $\delta$ ), rake angle ( $\lambda$ ), and strike angle ( $\phi$ ) (see Figure 2.1).

Tsunamis caused by the nearshore earthquakes have often resulted in the shorelines receding before advancing up on the beaches, i.e., tens of eyewitnesses' descriptions and mareogram records of recent tsunamis confirmed that subduction zone earthquakes typically generate leading depression wave propagating toward the adjacent shoreline while leading elevation wave propagates toward the open ocean. Tadepalli & Synolakis (1994, 1996) suggested classes of waves, called *N*-waves, to describe the evolution and runup of nearshore tsunamis. They defined two particular classes of *N*-waves: leading depression *N*-wave (LDN) and leading elevation *N*-wave (LEN) and showed that LDN runs up higher than its mirror image, LEN. They suggested LDN as a more appropriate initial waveform for nearshore tsunamis.

In this chapter, using regression analyses, the generalized *N*-wave profile and the maximum runup equation (Tadepalli & Synolakis 1996) will be defined in terms of the earthquake source parameters. Accordingly, the initial tsunami profile and maximum runup will be provided with respect to the earthquake source parameters.

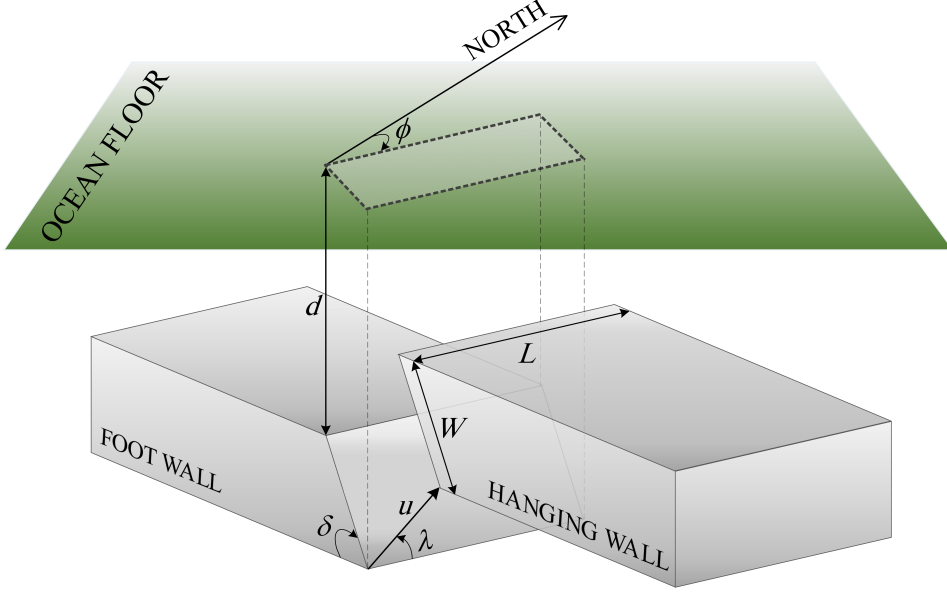


Figure 2.1: Definition sketch for the fault plane parameters:  $\phi$ ,  $\lambda$ , and  $\delta$  are the strike, the rake, and the dip angles, respectively;  $L$ ,  $W$ ,  $d$ , and  $u$  are the fault length, the fault width, the fault depth, and the fault slip amount, respectively.

## 2.1 *N*-wave through Earthquake Source Parameters

Here, the generalized *N*-wave profile is considered as in Tadepalli & Synolakis (1996) but in dimensional form as:

$$\eta(x) = \varepsilon_{1D} H (x - X_2) \operatorname{sech}^2 \gamma (x - X_1), \quad (2.1)$$

where  $\varepsilon_{1D} < 1 (\text{km}^{-1})$  is a scaling parameter to define the initial off-shore wave amplitude of  $H$  (m),  $X_1$  (km) and  $X_2$  (km) represent the distance from the origin of the coordinate system, and  $\gamma = \sqrt{3 p_0 H/4} (\text{km}^{-1})$ , with a steepness parameter  $p_0$  ( $\text{km}^{-2} \text{m}^{-1}$ ).  $X_2 - X_1$  adjusts the initial profile's depression and elevation sides. For small and negative distance  $X_2 - X_1$ , the generalized *N*-wave profile is an LDN, with a smaller amplitude leading depression wave than the elevation wave following it (see Figure 2.2).

This study sets down to identify relationships between *N*-wave parameters used in Eq. 2.1 and the earthquake source parameters. In this regard, a comprehensive set of submarine earthquake scenarios are defined and the initial ocean surface profiles are



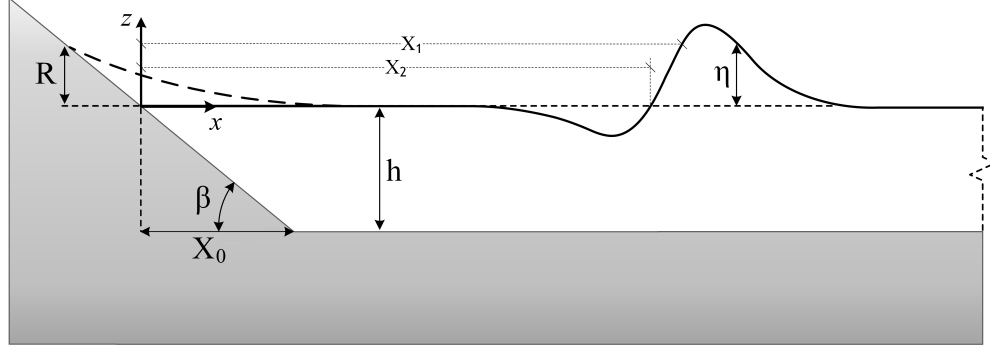


Figure 2.2: Definition sketch for the canonical problem and  $N$ -wave parameters.

estimated through Okada (1985) linear elastic dislocation formulation<sup>1</sup>. The maximum vertical displacement of the sea surface and consequently the maximum initial wave height is generated when the rake angle  $\lambda = 90^\circ$  (reverse fault) or  $\lambda = -90^\circ$  (normal fault). Thus, the rake angle is retained constant as  $\lambda = 90^\circ$  and the fault's orientation or strike angle as  $\phi = 270^\circ$  to ensure that the tsunami source is parallel to the shoreline and its bisector gives LDN (Figure 2.2). Then, the fault slip amount,  $u$ , is varied as 1, 5, 10, 15, and 20 m, the fault width,  $W$ , is considered from 20 to 150 km by 10 km increments, the fault depth,  $d$ , from 5 to 70 km by the interval of 5 km, and the dip angle  $\delta$ , from 5 to  $40^\circ$  by  $5^\circ$  increments one by one to define a set of earthquake source scenarios (Table 2.1).

Table 2.1: Range of earthquake source scenarios used in fitting database.

Fault Plane Parameter	Value
Strike angle ( $\phi$ )	$270^\circ$
Rake angle ( $\lambda$ )	$90^\circ$
Dip angle ( $\delta$ )	$5 - 40^\circ$ , $5^\circ$ increments
Slip amount ( $u$ )	1, 5, 10, 15, 20 m
Fault width ( $W$ )	20 – 150 km, 10 km increments
Fault depth ( $d$ )	5 – 70 km, 5 km increments

Using the defined scenarios, first, the nonlinear least squares regression method is used and 7840 curve fitting analyses are executed to fit the generalized  $N$ -wave profile (Eq. 2.1) to the dimensional initial surface profile obtained through Okada (1985)

<sup>1</sup> A Matlab code is used to calculate Okada's sea bottom deformation, available in MATLAB Central File Exchange (François 2010).

along the bisector, i.e., one-dimensional fitting. To overlap the  $N$ -wave profile with Okada (1985)'s coordinate system,  $X_1$  is fixed as zero in Eq. 2.1 in fitting processes. The yielded database shows that the depression wave amplitude (trough) decreases with increasing dip angle in the initial profile. The depression part almost disappears at the dip angle of  $40^\circ$ . Thus, in the following steps, the results of the  $40^\circ$  dip angle are excluded from the database.

Following the first step, the fitting results are used and again regressions are performed to determine the correlation between  $N$ -wave parameters  $\varepsilon_{1D}$ ,  $H$ ,  $X_2$ , and  $p_0$  and the earthquake source parameters. The second step will be explained in detail in the following subsections, and the fitting results will be presented.

### 2.1.1 Scaling parameter, $\varepsilon_{1D}$

The curve fitting results imply that  $\varepsilon_{1D}$  is independent of the slip amount and an optimal value for it can be obtained by a relation among the fault depth, the fault width and the dip angle, i.e.,  $\varepsilon_{1D} = \varepsilon_{1D}(d, W, \delta)$ . Considering the observations,  $\varepsilon_{1D}$  decreases logarithmically with the fault depth. Defining the relationship between  $\varepsilon_{1D}$  and fault depth as

$$\varepsilon_{1D}(d, W, \delta) = -a_1 \ln d + a_2, \quad (2.2)$$

a set of  $a_1(W, \delta)$  and  $a_2(W, \delta)$  is determined using the  $\varepsilon_{1D}$  and  $d$  couplings from the database. Examples of these couplings are given in Figure 2.3. Then, regression analyses are conducted to determine the relationships of  $a_1(W, \delta)$  and  $a_2(W, \delta)$  with  $W$  (Figure 2.4), which leads to power relations:

$$a_1(W, \delta) = a_3 W^{-a_4} \quad \text{and} \quad a_2(W, \delta) = a_5 W^{-a_6}. \quad (2.3)$$

Using the coefficients set of  $a_3(\delta)$  to  $a_6(\delta)$ , the regression analyses are further extended and the relationships of  $a_3(\delta)$  to  $a_6(\delta)$  are identified with the dip angle (Figure 2.5) as

$$a_3(\delta) = a_7 e^{a_8 \delta}, \quad a_4(\delta) = a_9 \delta^{a_{10}}, \quad a_5(\delta) = a_{11} e^{a_{12} \delta}, \quad \text{and} \quad a_6(\delta) = a_{13} \delta^{a_{14}}. \quad (2.4)$$

This will lead to the following estimate for  $\varepsilon_{1D}$  in terms of the earthquake source parameters:

$$\varepsilon_{1D}(d, W, \delta) = -a_7 e^{a_8 \delta} W^{-a_9 \delta^{a_{10}}} \ln d + a_{11} e^{a_{12} \delta} W^{-a_{13} \delta^{a_{14}}}. \quad (2.5)$$

However,  $a_7$  to  $a_{14}$  would involve error accumulation during the three steps of regression analyses. Hence, one more final nonlinear regression is carried out to identify  $a_7$  to  $a_{14}$  for which Eq. 2.5 best fits the  $\varepsilon_{1D}$  data in the fitting database resulting as

$$\varepsilon_{1D}(d, W, \delta) = -0.887 e^{0.005 \delta} W^{-0.867 \delta^{0.089}} \ln d + 2.358 e^{0.0015 \delta} W^{-0.701 \delta^{0.09}}. \quad (2.6)$$

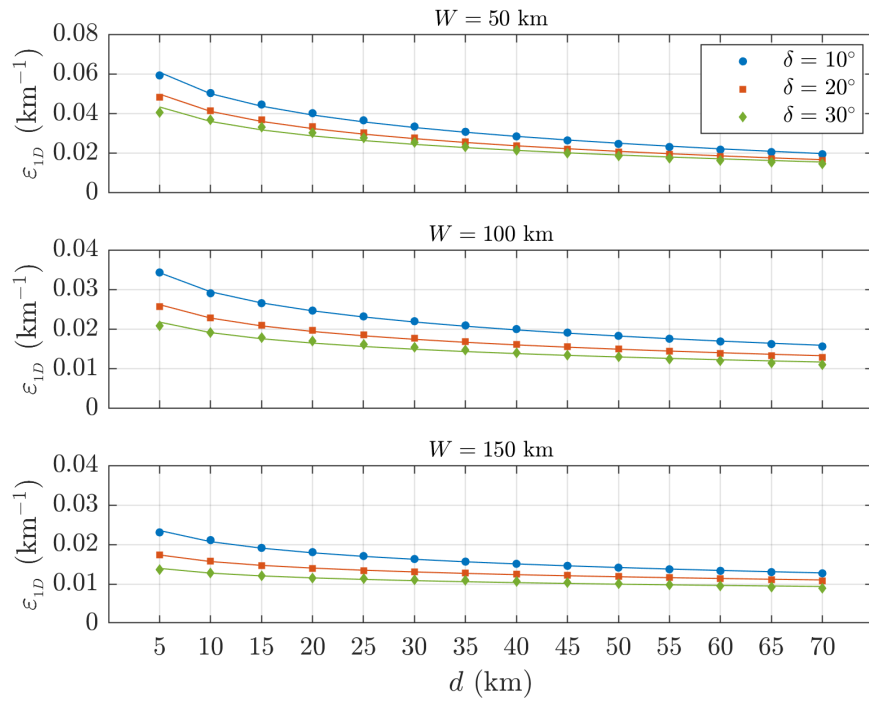


Figure 2.3: Examples of  $\varepsilon_{1D}$  and fault depth relationships for different fault widths and dip angles; and corresponding regression lines.

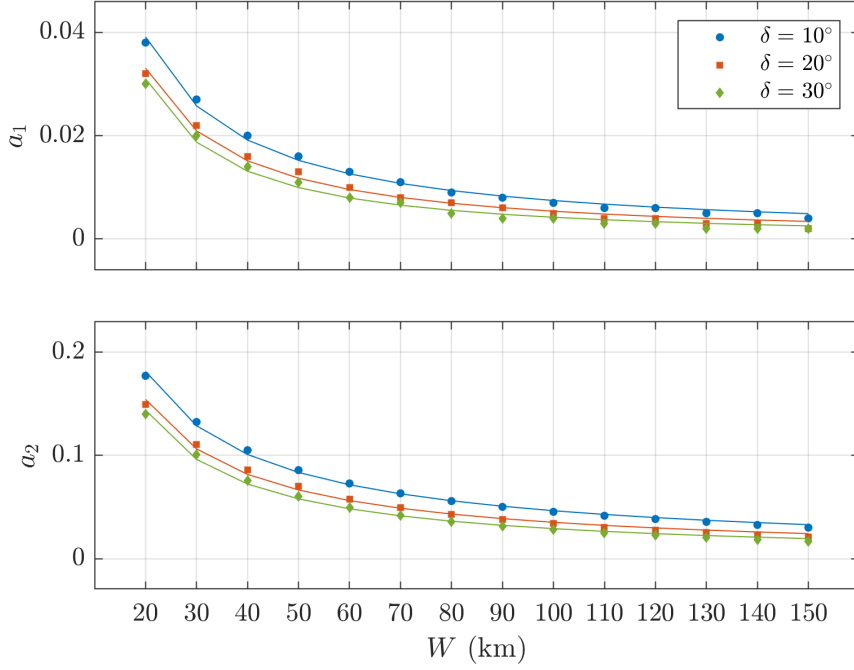


Figure 2.4: Examples of  $a_1(W, \delta)$  and  $a_2(W, \delta)$  relationships with fault width for different dip angles; and corresponding regression lines.

### 2.1.2 Off-shore wave amplitude, $H$

A relationship between the off-shore wave amplitude  $H$  and the fault plane parameters can be described as  $H = H(d, W, \delta, u)$ . Following the same methodology as described for  $\varepsilon_{1D}$ , first, it is noticed that  $H$  decreases exponentially with the fault depth (Figure 2.6) as

$$H(d, W, \delta) = b_1 e^{-b_2 d}. \quad (2.7)$$

Then, again regression analyses are performed to determine  $b_1(W, \delta)$  and  $b_2(W, \delta)$  relationships with the fault width (Figure 2.7), observing that both  $b_1(W, \delta)$  and  $b_2(W, \delta)$  have power relations with  $W$ :

$$b_1(W, \delta) = b_3 W^{b_4} \quad \text{and} \quad b_2(W, \delta) = b_5 W^{-b_6}. \quad (2.8)$$

Next, the coefficients in Eq. 2.8 are identified in term of the dip angle (Figure 2.8) as

$$b_3(\delta) = b_7 e^{b_8 \delta}, \quad b_4(\delta) = b_9 \delta^{b_{10}}, \quad b_5(\delta) = b_{11} \delta + b_{12}, \quad \text{and} \quad b_6(\delta) = b_{13} \delta + b_{14}. \quad (2.9)$$

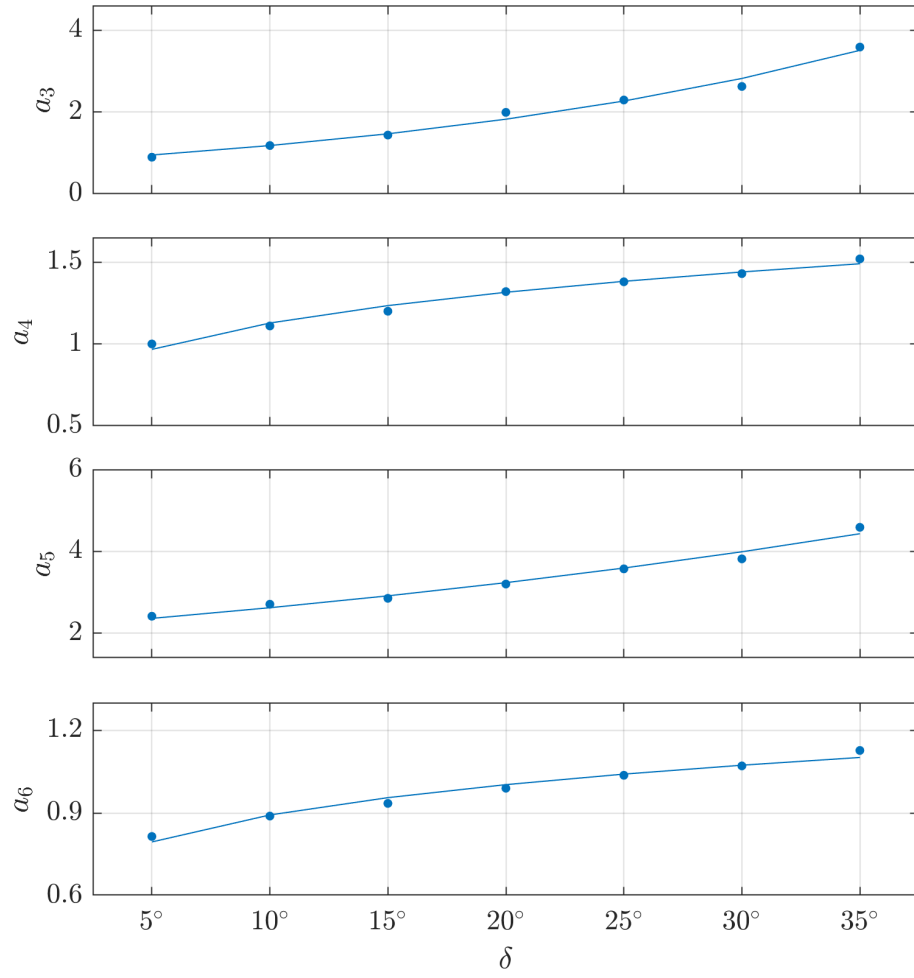


Figure 2.5: Relationships of  $a_3(\delta)$  to  $a_6(\delta)$  with dip angle; and corresponding regression lines.

Hence, the regression analyses result defines  $H$  as:

$$H(d, W, \delta) = b_7 e^{b_8 \delta} W^{b_9 \delta^{b_{10}}} e^{-d(b_{11} \delta + b_{12})} W^{-(b_{13} \delta + b_{14})}. \quad (2.10)$$

Performing a nonlinear regression one more time, the values of the coefficients  $b_7$  to  $b_{14}$  are estimated. In addition, results indicate that  $H$  is linearly proportional to the slip amount. Then, the final representation for  $H$  in terms of earthquake source parameters is:

$$H(d, W, \delta, u) = 0.328 u e^{0.005 \delta} W^{0.02 \delta^{0.44}} e^{d(0.002 \delta - 0.302)} W^{0.004 \delta - 0.794}. \quad (2.11)$$

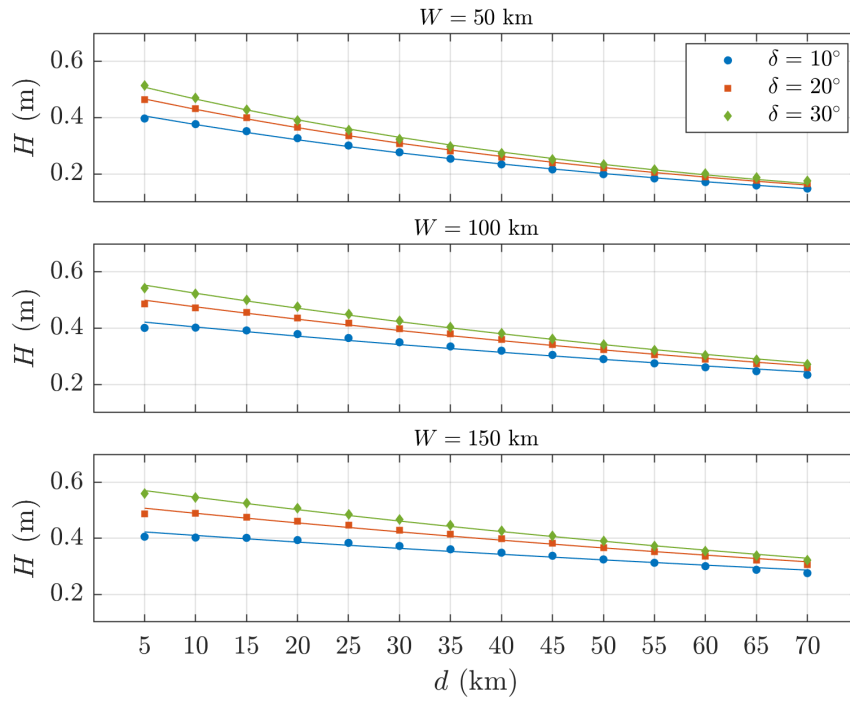


Figure 2.6: Examples of  $H$  and fault depth relationships for different fault widths and dip angles; and corresponding regression lines.

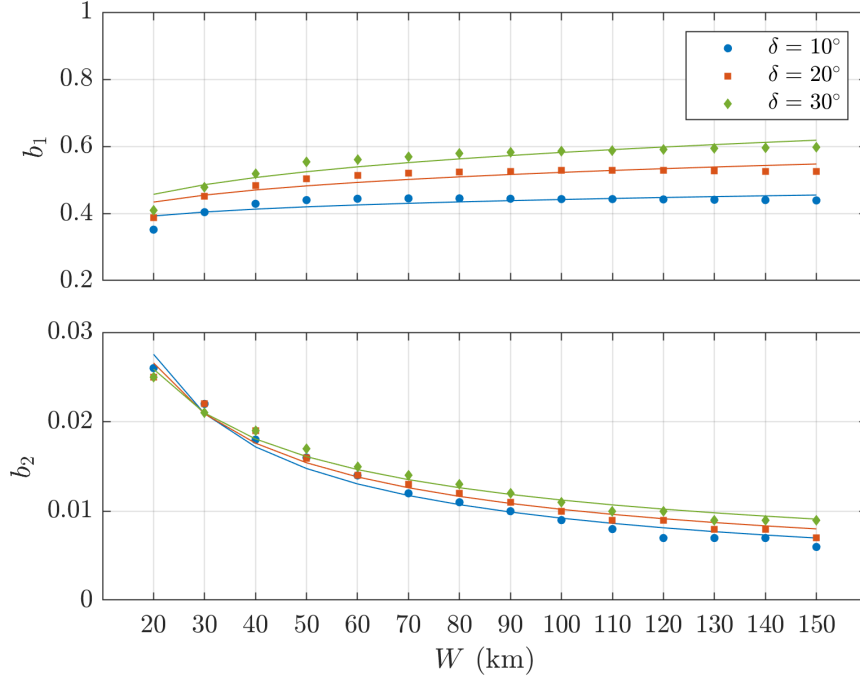


Figure 2.7: Examples of  $b_1(W, \delta)$  and  $b_2(W, \delta)$  relationships with fault width for different dip angles; and corresponding regression lines.

### 2.1.3 Distance $X_2 - X_1$

As mentioned earlier,  $X_1$  is set as zero to be consistent with Okada (1985)'s coordinate system. Curve fitting analyses show that  $X_2$  can be explained in terms of the fault depth, the fault width, and the dip angle, i.e.,  $X_2 = X_2(d, W, \delta)$ , and is not affected with the slip amount.  $X_2$  linearly decreases with increasing fault depth (Figure 2.9) as

$$X_2(d, W, \delta) = c_1 d + c_2. \quad (2.12)$$

Obtaining a set of  $c_1(W, \delta)$  and  $c_2(W, \delta)$ ; then, regression analyses are implemented to define the coefficients against the fault width (Figure 2.10) as

$$c_1(W, \delta) = c_3 W + c_4 \quad \text{and} \quad c_2(W, \delta) = c_5 W + c_6, \quad (2.13)$$

where the relationships of the coefficients  $c_3(\delta)$  to  $c_6(\delta)$  to the dip angle (Figure 2.11) are:

$$c_3(\delta) \simeq 0, \quad c_4(\delta) = c_7 \delta, \quad c_5(\delta) = c_8 \delta, \quad \text{and} \quad c_6(\delta) = c_9 \delta + c_{10}. \quad (2.14)$$

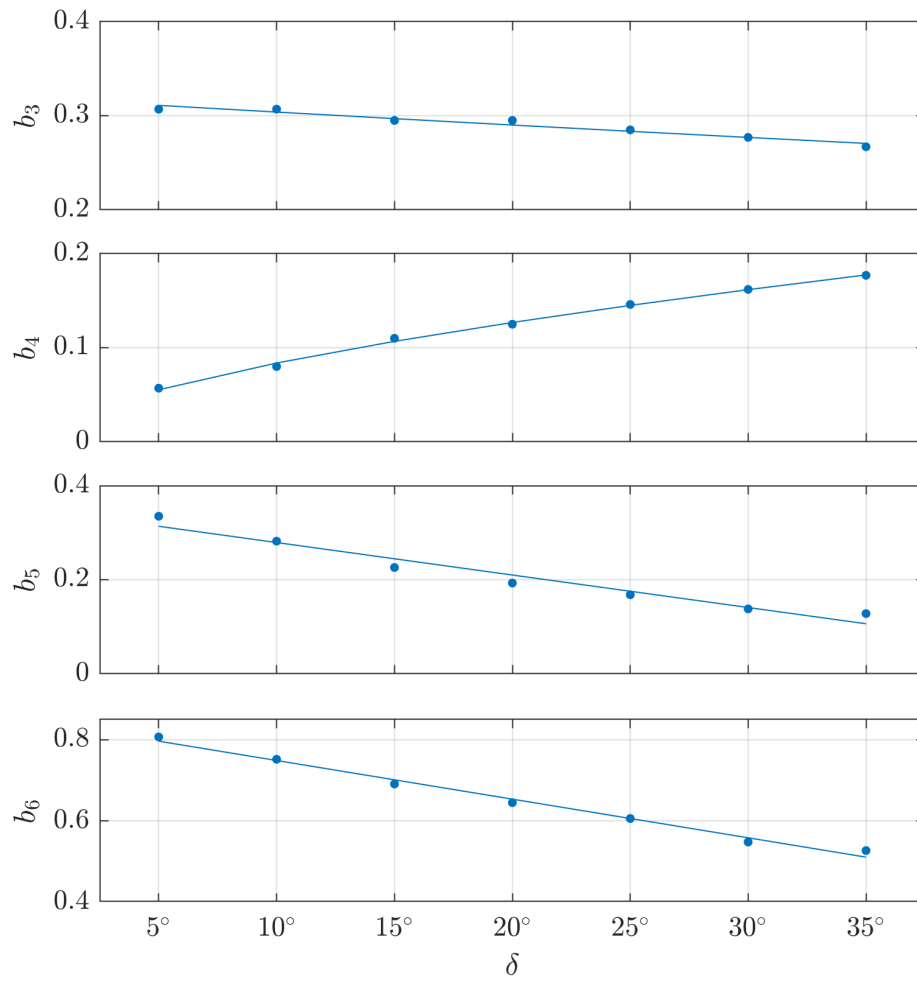


Figure 2.8: Relationships of  $b_3(\delta)$  to  $b_6(\delta)$  with dip angle; and corresponding regression lines.



The outcome defines  $X_2$  in terms of the fault depth, the fault width, and the dip angle as

$$X_2(d, W, \delta) = (c_7 d + c_8 W + c_9) \delta + c_{10}. \quad (2.15)$$

Finally, using the nonlinear regression, the value of coefficients from  $c_7$  to  $c_{10}$  are determined. To align with the generalized  $N$ -wave definition (Eq. 2.1),  $X_1$  is included in the final equation for  $X_2$ . The final equation for  $X_2$  is:

$$X_2(d, W, \delta) = (0.1171 - 0.0158 d - 0.0127 W) \delta - 1.0945 + X_1. \quad (2.16)$$

$X_1$  can be used to locate the initial wave at a certain distance from the shoreline, i.e., the initial profile can be shifted ocean-wise at the distance of  $X_1$ .

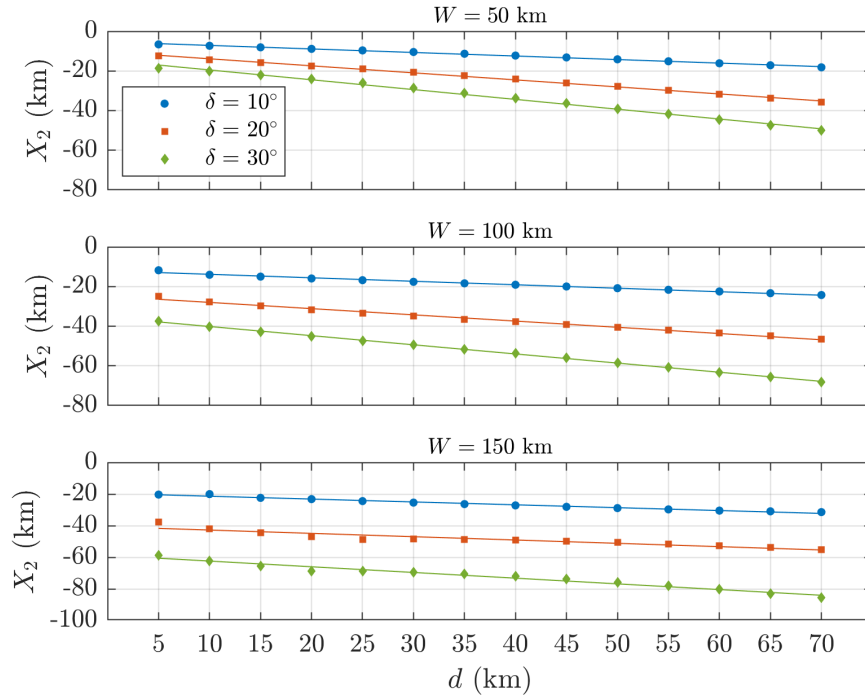


Figure 2.9: Examples of  $X_2$  and fault depth relationships for different fault widths and dip angles; and corresponding regression lines.

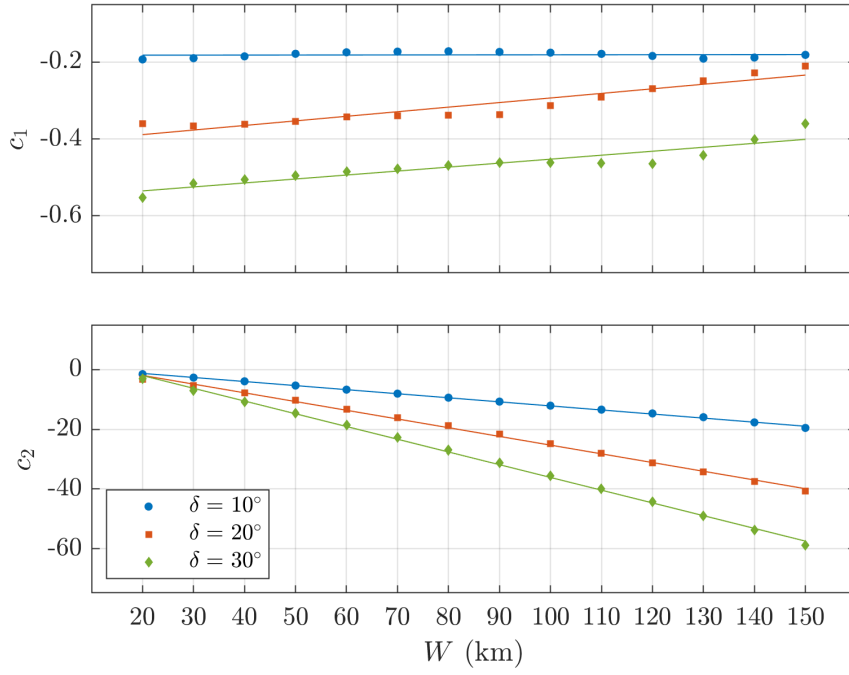


Figure 2.10: Examples of  $c_1(W, \delta)$  and  $c_2(W, \delta)$  relationships with fault width for different dip angles; and corresponding regression lines.

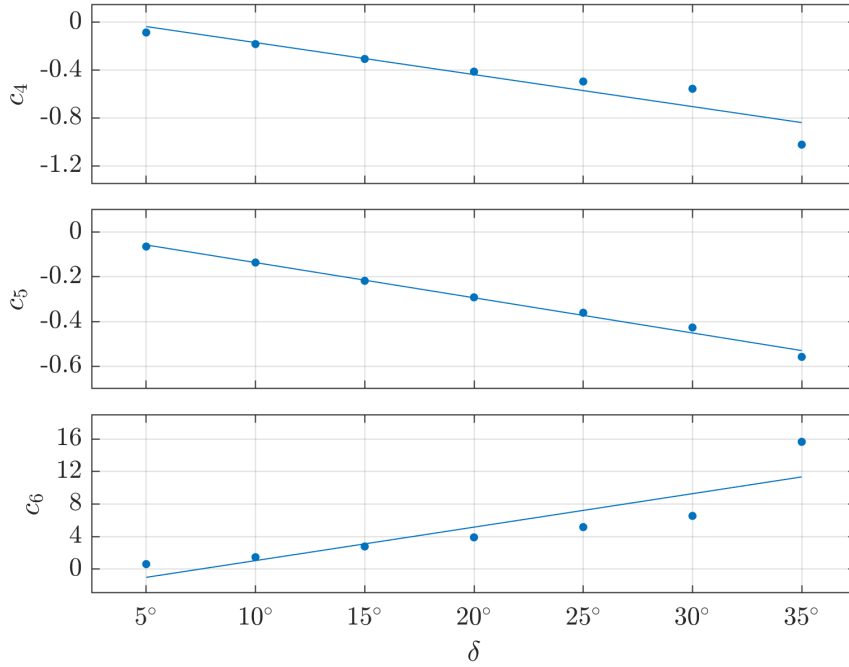


Figure 2.11: Relationships of  $c_3(\delta)$  to  $c_6(\delta)$  with dip angle and corresponding regression lines.

### 2.1.4 Steepness parameter, $p_0$

Analyses results reveal that  $p_0$  is affected by the fault depth, the fault width, the dip angle, and the slip amount i.e.,  $p_0 = p_0(d, W, \delta, u)$ . It is identified that the power fit best describes  $p_0$  in terms of the fault depth,  $d$ , (Figure 2.12) as

$$p_0(d, W, \delta) = k_1 d^{-k_2}. \quad (2.17)$$

Again, conducting regression analyses,  $k_1(W, \delta)$  and  $k_2(W, \delta)$  are obtained in terms of the fault width (Figure 2.13):

$$k_1(W, \delta) = k_3 W^{-k_4} \quad \text{and} \quad k_2(W, \delta) = -k_5 \ln W + k_6, \quad (2.18)$$

where, the relationships of  $k_3(\delta)$  to  $k_6(\delta)$  with the dip angle (Figure 2.14) are as follows:

$$k_3(\delta) = k_7 e^{k_8 \delta}, \quad k_4(\delta) = k_9 \delta + k_{10}, \quad k_5(\delta) = k_{11} e^{k_{12} \delta}, \quad \text{and} \quad k_6(\delta) = k_{13} \delta + k_{14}. \quad (2.19)$$

Hence, the following equation describes  $p_0$  in terms of the fault depth, the fault width, and the dip angle:

$$p_0(d, W, \delta, u) = k_7 e^{k_8 \delta} W^{-(k_9 \delta + k_{10})} d^{k_{11} e^{k_{12} \delta} \ln W - k_{13} \delta - k_{14}}. \quad (2.20)$$

Further, it is noticed that  $p_0$  is inversely proportional with the slip amount. Performing the nonlinear regression once more, the final formula for  $p_0$  is:

$$p_0(d, W, \delta, u) = 3.92 u^{-1} e^{0.074 \delta} W^{-0.022 \delta - 1.495} d^{0.075 e^{0.034 \delta} \ln W - 0.014 \delta - 0.776}. \quad (2.21)$$

Substituting Eqs. 2.6, 2.11, 2.16, and 2.21 in Eq. 2.1; finally, the one-dimensional form of  $N$ -wave profile is defined in terms of the earthquake source parameters referring to as the one-dimensional  $N$ -wave through earthquake parameters (NEP):

$$\eta_{NEP}(x, d, W, \delta, u) = \varepsilon_{1D} H(x - X_2) \operatorname{sech}^2 \gamma(x - X_1). \quad (2.22)$$

Eq. 2.22 can be used to estimate the initial profile of tsunamis using the earthquake source parameters. Further, the two-dimensional form of  $N$ -wave profile referred to as two-dimensional NEP (Eq. 3.11) is provided in chapter 3. Figure 2.15 indicates one example for the comparison of the two-dimensional NEP profile with the individually fitted  $N$ -wave profile and their corresponding Okada's displacement model.

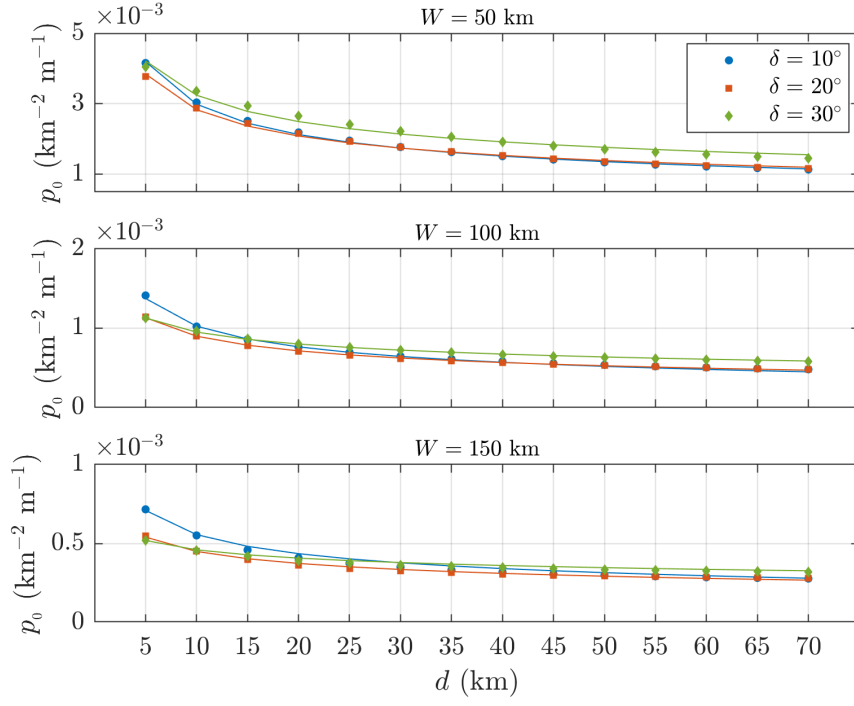


Figure 2.12: Examples of  $p_0$  and fault depth relationships for different fault widths and dip angles; and corresponding regression lines.

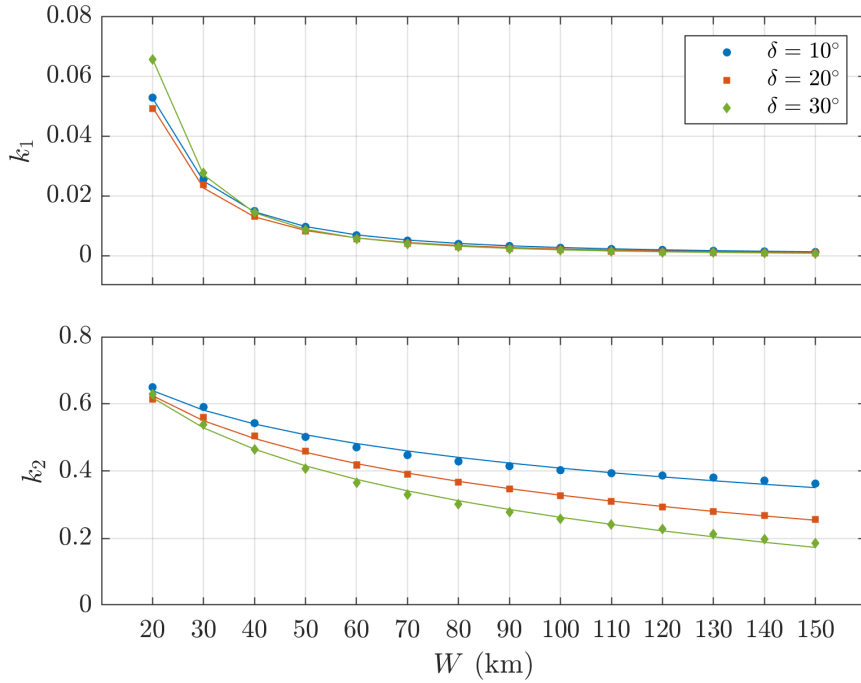


Figure 2.13: Examples of  $a_1(W, \delta)$  and  $a_2(W, \delta)$  relationships with fault width for different dip angles; and corresponding regression lines.

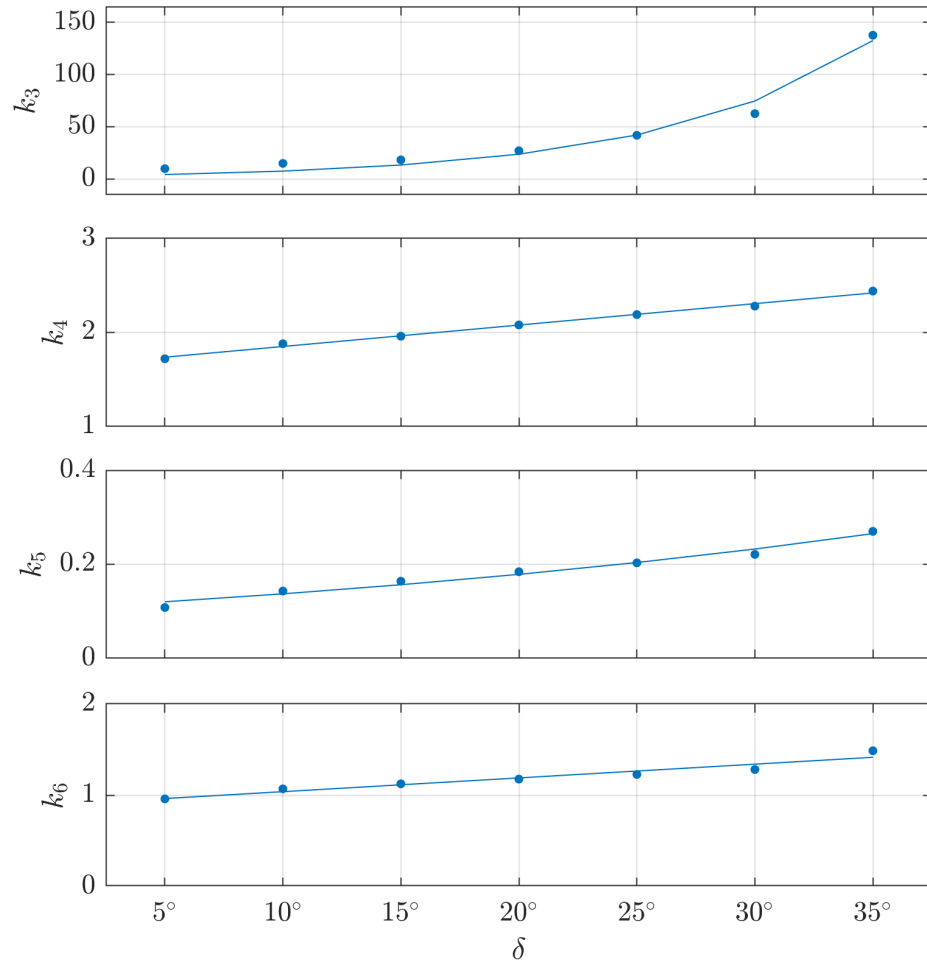


Figure 2.14: Relationships of  $k_3(\delta)$  to  $k_6(\delta)$  with dip angle; and corresponding regression lines.

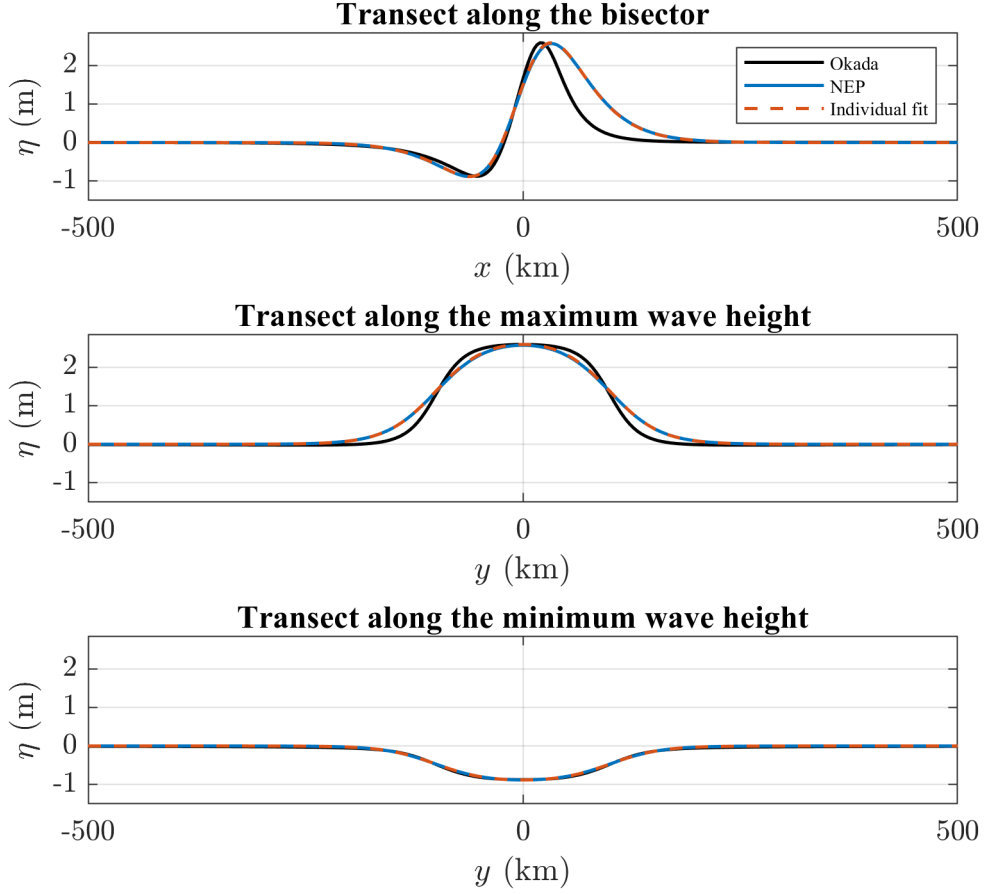


Figure 2.15: An example of two-dimensional NEP profile (blue solid line) compared with the individually fitted  $N$ -wave profile (red dashed line) and Okada (1985)'s displacement model (black solid line) using the submarine earthquake source as  $L = 200$  km,  $W = 50$  km,  $d = 40$  km,  $u = 10$  m,  $\delta = 20^\circ$ ,  $\lambda = 90^\circ$ , and  $\phi = 270^\circ$ . The Root Mean Squared Errors (RMSEs) between NEP and Okada profiles from top to bottom are calculated as 0.26 m, 0.13 m, and 0.02 m, respectively.

## 2.2 Maximum Runup through Earthquake Source Parameters

At this point, the tsunami initial profile has been defined with respect to the fault plane parameters. Next, the aim is to determine the maximum tsunami runup in terms of the earthquake source parameters. Here, undisturbed ocean depth  $h$  is used as the reference depth, either in m ( $h_m$ ) or in km ( $h_{km}$ ) dimensions, to introduce the non-dimensional variables as

$$\tilde{\eta}, \tilde{H}, \tilde{R} = (\eta, H, R)/h_m, \quad \tilde{X}_0, \tilde{X}_1, \tilde{X}_2, \tilde{L} = (X_0, X_1, X_2, L)/(h_{km}),$$

$$\tilde{p}_0 = p_0 \times (h_{km})^2 \times h_m, \text{ and } \tilde{\varepsilon}_{1D} = \varepsilon_{1D} \times (h_{km}). \quad (2.23)$$

Tadepalli & Synolakis (1994) used the solution methodology of Synolakis (1986) and solved the linear shallow-water wave equations to obtain the evolution of several type of  $N$ -waves over a canonical bathymetry. They performed asymptotic analysis and expressed tsunami runup laws for different  $N$ -wave initial waveforms. Further, Tadepalli & Synolakis (1994) computed an approximate upper bound for runup of the non-breaking LDNs.

Further, Tadepalli & Synolakis (1996) introduced steepness parameter in the definition of  $N$ -wave to represent initial tsunami profile more realistically, however, did not provide the approximate upper bound of the runup as in Tadepalli & Synolakis (1994). They calculated the runup of  $N$ -wave profile (2.1) as

$$\tilde{R}(\tilde{t}) = \frac{16}{3} \tilde{\varepsilon}_{1D} \tilde{\gamma}_s^{3/2} (2\pi \tilde{X}_0)^{1/2} \left( \frac{1}{\tilde{p}_0^{1/4}} \right) \sum_{n=1}^{\infty} (-1)^{n+1} n^{1/2}$$

$$\times \left\{ 2n\tilde{\gamma} (\tilde{X}_1 - \tilde{X}_2 - \tilde{\phi}) + \frac{1}{2} \right\} e^{-2n\tilde{\gamma}\tilde{\phi}}, \quad (2.24)$$

where  $\tilde{\gamma}_s = \sqrt{3\tilde{H}/4}$ ,  $\tilde{X}_0 = \cot \beta$  (distance to toe of the sloping beach in canonical topography and  $\beta$  is the beach slope),  $\tilde{\phi} = \tilde{X}_1 + \tilde{X}_0 - \tilde{c}\tilde{t}$ , and with normalization  $\tilde{c} = 1$ .

This study uses the same approach as Tadepalli & Synolakis (1994) and Synolakis (1987) and calculates an approximate upper bound for Eq. 2.24 as

$$\tilde{R}_{REP}(d, W, \delta, u) = 2.831 \tilde{\varepsilon}_{1D} \sqrt{\tilde{X}_0} \tilde{H}^{5/4} \tilde{p}_0^{1/4} \left[ \left| \tilde{X}_1 - \tilde{X}_2 - \frac{0.366}{\tilde{\gamma}} \right| + \frac{0.618}{\tilde{\gamma}} \right]. \quad (2.25)$$

Eq. 2.25 is valid when  $\tilde{H} < \tilde{H}_{breaking}$ .

Substituting the non-dimensional form of Eqs. 2.6, 2.11, 2.16, and 2.21 into Eq. 2.25, the approximate maximum runup for one-dimensional NEP profile (Eq. 2.22) is provided. The resulting equation, Eq. 2.25, is referred to hereafter as runup through earthquake parameters (REP). Figure 2.16 compares maximum runup values calculated through REP with those computed using the  $\varepsilon_{1D}$ ,  $H$ ,  $X_2$ , and  $p_0$  parameters obtained through the fitting database for 240 different earthquake source scenarios, observing a good agreement.

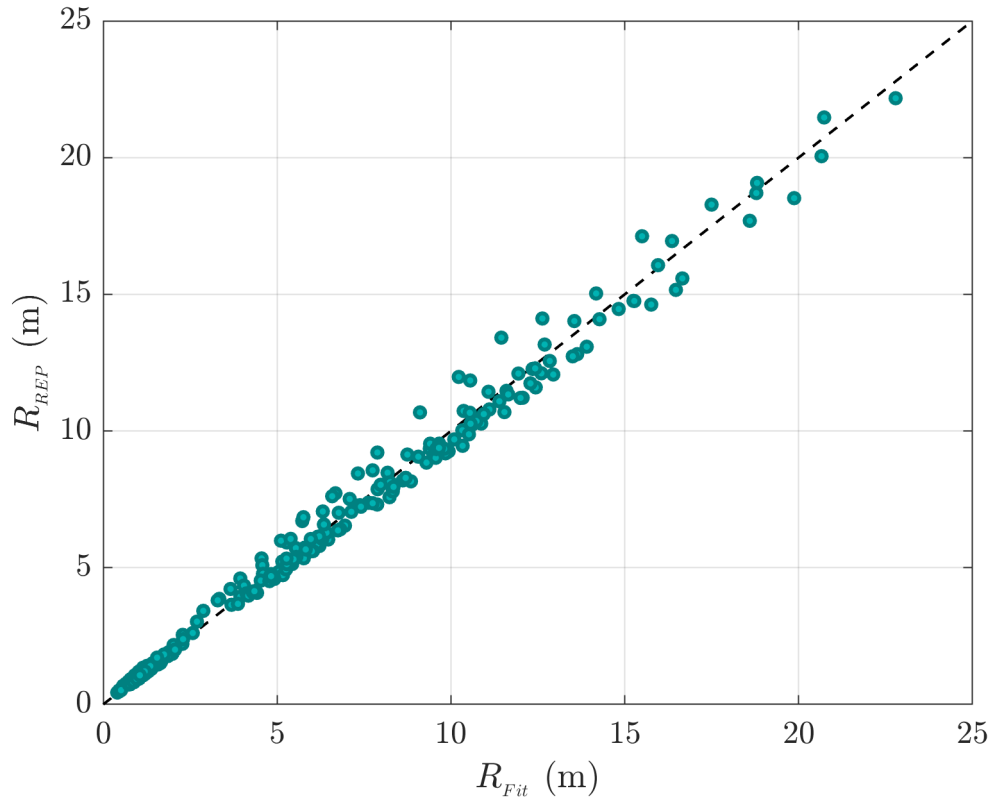


Figure 2.16: Comparison of runup estimates calculated using REP (Eq. 2.25) with those calculated using the parameters in fitting database. The earthquake source scenarios are defined by varying parameters as  $W = 20, 50, 100$ , and  $150$  km,  $d = 10, 20, 30$  and  $40$  km,  $u = 1, 5$ , and  $10$  m,  $\delta = 10$  to  $30^\circ$  with  $5^\circ$  increments, and the beach slope of  $1/20$ .



### 2.3 Field Validation

In this section, NEP (Eq. 2.22) and REP (Eq. 2.25) are tested by comparing with the field runup measurements for several events. One-dimensional NEP is used to obtain the initial waveforms of Nicaragua 1992; Indonesia, Java 1994; Mexico, Colima 1995; Sumatra 2004; Chile, Maule 2010; Japan, Tohoku 2011; and the Aegean Sea, Türkiye 2020 tsunamis (Table 2.2, including corresponding references). Then, tsunami runup values for the considered events are calculated using REP and compared with the mean and extreme field runup measurements. The mean and extreme field runup measurements have been acquired through the National Geophysical Data Center / World Data Service: NGDC/WDS (2022). Further, the field runup measurements for the Aegean Sea, Türkiye event have been obtained from Doğan et al. (2021). The beach slope ( $\tan \beta$ ) and the ocean depth ( $h$ ) for Sumatra 2004 and Chile 2010 events have been considered the same as Sepúlveda & Liu (2016). The ocean depth and the beach slope are approximated using the General Bathymetric Chart of the Oceans (GEBCO, 2020) bathymetry for the 2011 Tohoku and the 2020 Türkiye tsunamis. In addition, for other events, the referred parameters have been used the same as Wronna et al. (2021).

Initial wave profiles are computed using one-dimensional NEP and compared with Okada (1985)'s dislocation model results using earthquake source parameters, given in Table 2.2. All initial wave profiles estimated from NEP fit well with Okada's model (Figure 2.17). Further, runup estimations based on REP are compatible with post-events field runup measurements (Figure 2.18 and Table 2.2). Following, observations are summarised.

A runup height of 9.45 m is calculated for the 1992 Nicaraguan tsunami, which is within the mean and extreme field runup measurements (6.80 – 9.90 m). For Java 1994, the runup calculated by REP is about 8 m (1.5 m less than the mean runup value), yet between the minimum 5.4 m and maximum 13.9 m runup values of field observations, which have been reported only in four locations (NGDC/WDS 2022, Maramai & Tinti 1997). For Mexico, Colima 1995 event, REP is in line with the post-event field surveys measurements with the runup height of 6.64 m. While Borrero et al. (2006)'s post-tsunami field survey measurements in northern Sumatra in the

region around Banda Aceh reveals the runup variation between 2.5 and 31 m for the 2004 Sumatra tsunami, NGDC/WDS 2022 reports 13.44 m and 40.20 m mean and extreme field runup measurements. This study uses the same rupture parameters as Sepúlveda & Liu (2016) for the event, who calculated a runup height of 7.79 m. REP estimates a runup height of 9.67 m, which is between the minimum and maximum field runup measurements; however, it underestimates the mean and extreme field runup values. In the 2010 Chile Maule field survey, two maximum runup heights of 29 m along a steep coastal bluff at Constitución and 20 m in a coastal bluff within 70 m of the shoreline to the south of the Tirúa river have been reported (Fritz et al. 2011). The measurements indicate that except for the bluff landforms in the other coastal regions, the tsunami maximum runup values were 5 – 15 m, e.g., in the areas between Constitución and Punta Morguilla (5 – 15 m), in the regions between Punta Morguilla and Mehuín mostly under 5 m, and in the Greater Valparaíso area below 5 m. REP runup height of 12.22 m is in accordance with the post-event field observations and Sepúlveda & Liu (2016)'s runup result of 11.67 m for the event. The magnitude  $M_w$  9.1, 11 March 2011 East Japan earthquake generated one of the most destructive tsunamis in recorded history. The quake lasted for six minutes and a half-hour later, a massive tsunami penetrated the Pacific coast of Japan. The runup height reached 16.4 and 20.8 m at the distance of 30 and 40 km from the nuclear power plant, and the maximum runup height of 39.7 m was measured at Aneyoshi, Miyako (Mori et al. 2011). REP computes a runup height of 26.53 m, which is in the range of mean and extreme field runup measurements (11.30 – 39.70 m). This study utilizes the earthquake source model provided by National Earthquake Information Center (NEIC) for the Aegean Sea, Türkiye 2020 event. REP calculates the runup height of 1.83 m, which is in agreement with the mean and extreme field runup observations (1.49 – 3.82 m) along the Turkish coast reported by Doğan et al. (2021).

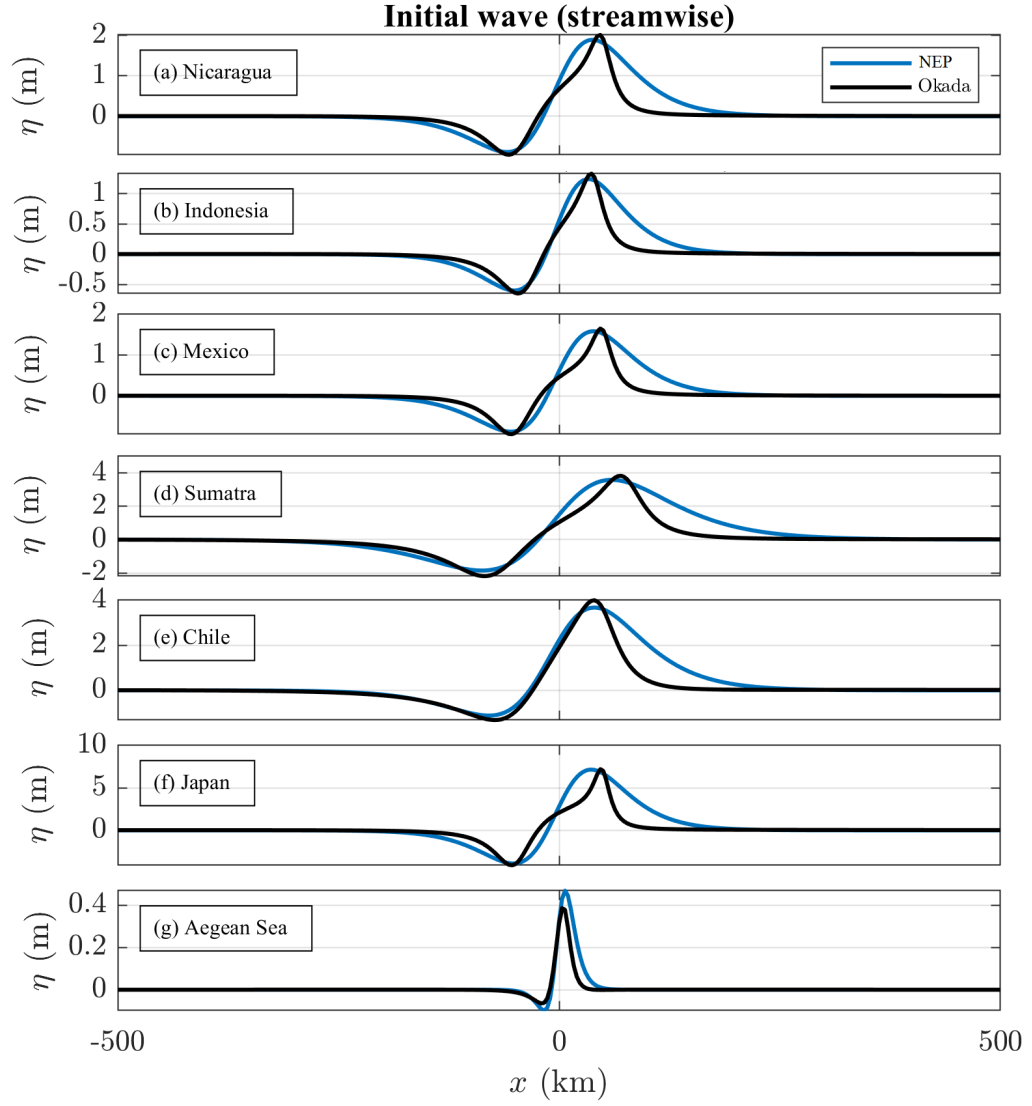


Figure 2.17: Leading depression initial waveform through NEP and Okada (1985) for (a) Nicaragua 1992; (b) Indonesia, Java 1994; (c) Mexico, Colima 1995; (d) Sumatra 2004; (e) Chile, Maule 2010; (f) Japan, Tohoku 2011; and (g) Aegean Sea, Türkiye 2020. The fault plane parameters for the events and references are given in Table 2.2.

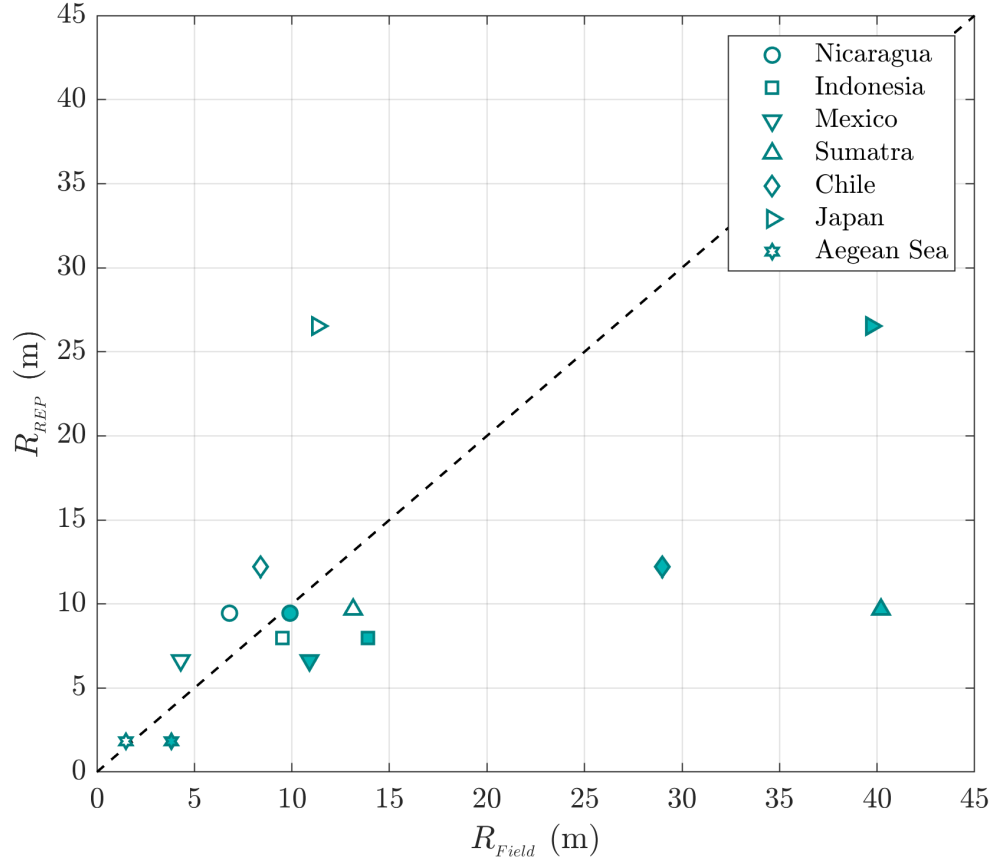


Figure 2.18: Comparison of runup values calculated using REP (Eq. 2.25) with mean (not-filled symbols) and extreme (filled symbols) field runup measurements. The fault plane parameters for the events and references are given in Table 2.2.

Table 2.2: The source parameters and beach slopes used for the events. Here,  $M_w$ ,  $u$ ,  $W$ ,  $d$ , and  $\delta$  indicate the moment magnitude, the slip amount, the fault width, the fault depth, and the dip angle, respectively;  $\tan \beta$  represents the nearshore beach slope and  $h$  is the ocean depth.  $R_{REP}$  is calculated using Eq. 2.25 and  $R_{Mean}$  and  $R_{Ext}$  show the mean and extreme field runup measurements for the events.

Event	References	$M_w$	$u$ (m)	$W$ (km)	$d$ (km)	$\delta$ ( $^\circ$ )	$\tan \beta$	$h$ (m)	$R_{REP}$ (m)	Field measurements	
										$R_{Mean}$ (m)	$R_{Ext}$ (m)
Nicaragua 1992	Wronna et al. (2021)										
	Okal & Synolakis (2004)										
	Piatanesi et al. (1996)										
	Dziewonski et al. (1995)	7.7	5.00	100	16	12	1/29	4814	9.45	6.80	9.90
Indonesia, Java 1994	Wronna et al. (2021)										
	Okal & Synolakis (2004)										
	Abercrombie et al. (2001)										
	Dziewonski et al. (1995)	7.8	3.40	80	16	12	1/57	3294	7.98	9.50	13.90
Mexico, Colima 1995	Wronna et al. (2021)										
	Okal & Synolakis (2004)										
	Mendoza & Hartzell (1999)										
	Dziewonski et al. (1997)	8.0	4.30	100	15	9	1/18	3844	6.64	4.30	10.90
Sumatra, Aceh 2004	Sepúlveda & Liu (2016)										
	Sipkin et al. (2000)	9.3	10.22	150	30	10	1/34	1500	9.67	13.14	40.20
Chile, Maule 2010	Sepúlveda & Liu (2016)										
	Sipkin et al. (2000)	8.8	10.05	100	30	20	1/32	3100	12.22	8.40	29.00
Japan, Tohoku 2011	NEIC										
	Duputel et al. (2012)	9.1	19.00	100	11.5	9	1/34	1500	26.53	11.30	39.70
Aegean Sea, Türkiye 2020	NEIC										
		7.0	1.50	15	11.5	29	1/50	480	1.83	1.49	3.82



## CHAPTER 3

### IMPACTS OF EARTHQUAKE SOURCE PARAMETERS ON TSUNAMI FOCUSING

Earthquake-generated tsunamis caused by the impulsive movement of the seafloor evolve substantially through spatial and temporal spreading from their source region, e.g., the maps of energy propagation –maximum wave height computed at each grid point– of the 26 December 2004 Sumatra tsunami (Titov et al. 2005) and the 11 March 2011 Japan tsunami (Tang et al. 2012). In their numerical simulations for the 2004 Sumatra tsunami, Titov et al. (2005) monitored two main factors influencing tsunami wave directionality: the bathymetric waveguides (Koshimura et al. 1999) and the focusing configuration of the source region (Marchuk & Titov 1989). This chapter will study the latter. Focusing refers to abnormal wave amplification in the direction of depression side of an  $N$ -wave (Figure 3.1). This chapter will examine how the focusing amplitude and location of the focusing point –focusing distance– vary for different source configurations resulting from various earthquake source scenarios, and finally, it will explore the influence of earthquake source parameters on tsunami focusing.

Marchuk & Titov (1989) carried out numerical simulation for finite crest length  $N$ -wave-type initial displacement (Figure 3.1a) and demonstrated the existence of a focusing point. They explained the tsunami focusing process for a rectangular initial deformation consisting of plus-minus surface displacements. Their numerical experiments showed that the focusing point stays somewhere on a straight line coming through the centers of both depression and elevation part of the tsunami initial surface displacement. They noticed that at a point along the bisector line –reaching through centers of both elevation ( $E$ ) and depression ( $D$ ) sides of initial wave– the

focusing point ( $F$ ) exists where waves crests from the elevation part and the short boundaries ( $ab$  and  $ef$ ) of the depression part arrive simultaneously (Figures 3.1*b, c* and 3.2). Marchuk & Titov (1989) used the isochrone technique to show the potentially dangerous area in the neighborhood of the focusing point. They illustrated that if the center of the elevation part and the short boundaries of the depression part of the rectangular tsunami source are located in the same isochrone –identical travel times– the wave height will be amplified, hence, the focusing point.

Later, the focusing phenomenon was presented in Kânoğlu et al. (2013). They explored tsunami focusing generated by finite-crested  $N$ -wave-type initial displacement using linear non-dispersive (Aydın 2011) and linear dispersive (Kervella et al. 2007) theories analytically and nonlinear non-dispersive (Titov et al. 2011) and weakly nonlinear weakly dispersive (Zhou et al. 2011) theories numerically. Their study reveals that the focusing points exist in tsunami evolution using all four approaches of the governing equations of hydrodynamics with almost unnoticeable differences among them. They referred to the focusing as a possible explanation for unusually high runup observations, e.g., the 17 July 1998 Papua New Guinea; the 17 July 2006 Java, Indonesia; and the 11 March 2011 Japan tsunamis.

Afterward, Aydın (2018) studied how the focusing amplitude and location of the focusing point can change by varying the initial wave's specific geometric parameters, e.g., wave steepness and crest length. He used the linear shallow water-wave theory and calculated the maximum wave envelopes for different finite-crested  $N$ -wave initial profiles by changing the relevant parameters. Then, he compared the maximum wave envelopes for different initial profiles and concluded the study: for mild initial waves, maximum wave amplitude increases substantially with the initial wave crest's transverse length; however, the location of the focusing point remains almost constant. Meanwhile, the focusing point dislocates significantly for steep initial waves, although it drives a slight increase in the wave maximum.

In what follows, the analytical solution provided in Aydın (2011) will be utilized, and the tsunami focusing resulting from the initial wave configuration will be related to the earthquake source parameters for the finite crest length initial  $N$ -wave profile. In this regard, the linear shallow water-wave theory will be used and the connection



between focusing amplitude and fault plane parameters, and the relationship between focusing distance and earthquake source parameters will be examined (see Figure 3.3 for definition of the focusing parameters).

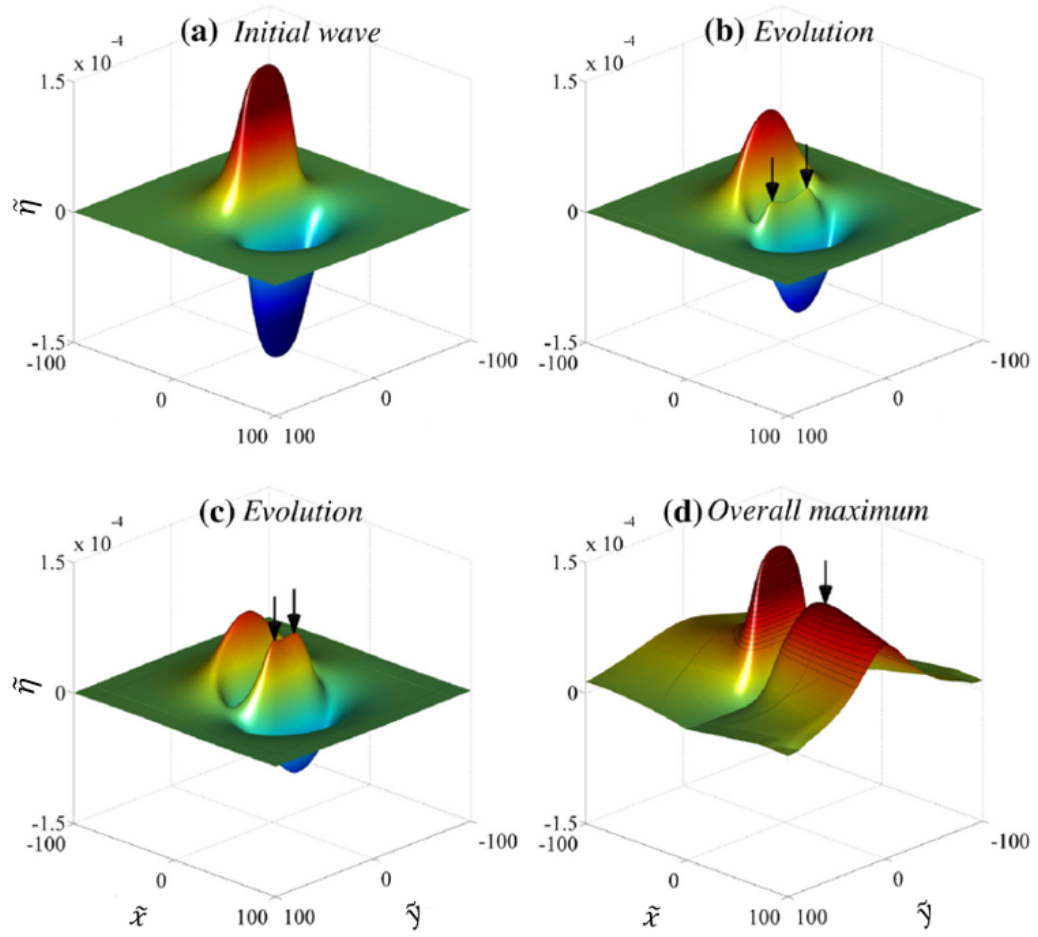


Figure 3.1: Evolution and focusing of a finite-crested  $N$ -wave profile; (a) initial wave, (b,c) evolution, and (d) focusing. After Kânoğlu et al. (2013).

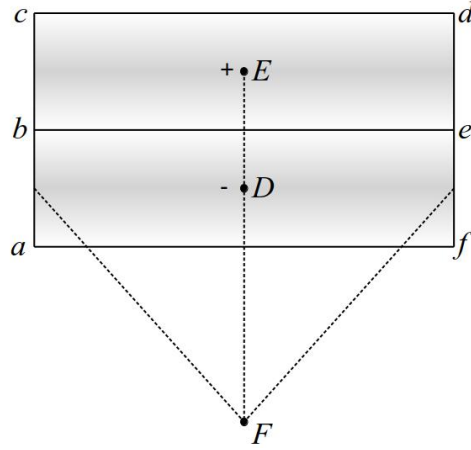


Figure 3.2: Location of the focusing point  $F$  for an  $N$ -wave-type initial surface displacement. After Marchuk & Titov (1989).

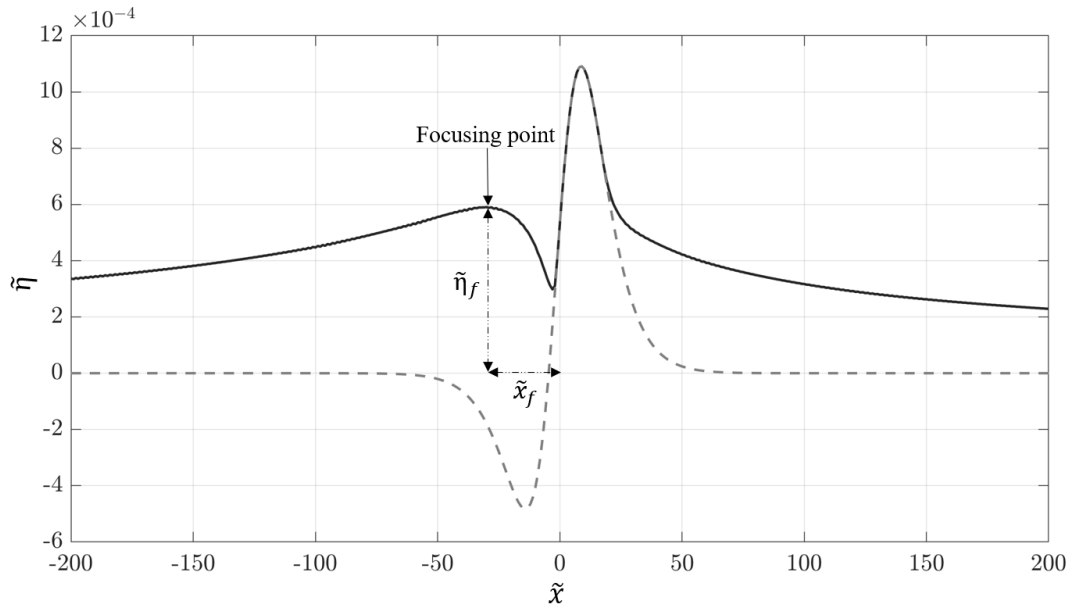


Figure 3.3: Definition of the focusing parameters:  $\tilde{\eta}_f$ : dimensionless focusing amplitude and  $|\tilde{x}_f|$ : dimensionless focusing distance. Dashed and solid lines indicate an example of the initial tsunami wave and maximum wave envelope along the bisector, respectively. The earthquake source parameters are:  $\phi = 270^\circ$ ,  $\lambda = 90^\circ$ ,  $\delta = 15^\circ$ ,  $u = 10$  m,  $L = 200$  km,  $W = 50$  km, and  $d = 20$  km.

### 3.1 Review of Analytical Solution

The propagation phase of tsunamis can be modeled using the shallow water-wave (SW) equations either numerically or analytically. SW equations are derived from Euler equations by neglecting vertical acceleration. Two-dimensional nonlinear shallow water-wave (NSW) equations can be written as three first-order partial differential equations:

$$u_t + uu_x + vv_y + g\eta_x = 0, \quad (3.1a)$$

$$v_t + uv_x + vv_y + g\eta_y = 0, \quad (3.1b)$$

$$[(h + \eta)u]_x + [(h + \eta)v]_y + \eta_t = 0, \quad (3.1c)$$

where  $u = u(x, y, t)$  and  $v = v(x, y, t)$  are the horizontal depth-averaged velocities in  $x$ - and  $y$ -directions, respectively.  $\eta = \eta(x, y, t)$  is the free surface elevation,  $h = h(x, y)$  is the undisturbed water depth,  $g$  is the gravitational acceleration,  $x$  and  $y$  represent the spatial coordinates, and  $t$  is time. The subscripts denote the derivatives regarding the related variables.

Eliminating nonlinear terms, a single second-order partial differential equation, i.e., the linear shallow water-wave (LSW) equation can be derived. Considering a constant ocean depth of  $h$ , the LSW equation can be written as

$$\eta_{tt} - gh(\eta_{xx} + \eta_{yy}) = 0. \quad (3.2)$$

This is a linear non-dispersive wave model. Non-dimensional variables can be defined as

$$(\tilde{x}, \tilde{y}) = \frac{(x, y)}{l_0} = \frac{(x, y)}{h}, \quad \tilde{\eta} = \frac{\eta}{h_0} = \frac{\eta}{h}, \quad \text{and} \quad \tilde{t} = \frac{t}{t_0} = t\sqrt{\frac{g}{h}}, \quad (3.3)$$

where  $l_0$ ,  $h_0$ , and  $t_0 = l_0/\sqrt{gh_0}$  represent the characteristic length, depth, and time scales, respectively, with  $l_0 = h_0 = h$  being ocean depth.

The non-dimensional form of Eq. 3.2 becomes

$$\tilde{\eta}_{\tilde{t}\tilde{t}} - \tilde{\eta}_{\tilde{x}\tilde{x}} - \tilde{\eta}_{\tilde{y}\tilde{y}} = 0. \quad (3.4)$$

Aydin (2011) extended the initial  $N$ -wave profile (Tadepalli & Synolakis 1996) into a finite crest length and provided an analytical solution, solving the LSW equation, for

propagation of a finite crest length initial wave over a constant ocean depth basin. He defined an initial surface profile with zero initial velocity as the initial condition for Eq. (3.4):

$$\tilde{\eta}(\tilde{x}, \tilde{y}, \tilde{t} = 0) = \tilde{\eta}_0(\tilde{x}, \tilde{y}), \quad (3.5a)$$

$$\tilde{\eta}_t(\tilde{x}, \tilde{y}, \tilde{t} = 0) = 0. \quad (3.5b)$$

For the solution of this initial value problem, Aydın (2011) utilized the Fourier transform pair over the space variables  $(\tilde{x}, \tilde{y})$

$$\tilde{\eta}(\tilde{\rho}, \tilde{\sigma}, \tilde{t}) = \int_{-\infty}^{\infty} \int_{-\infty}^{\infty} \tilde{\eta}(\tilde{x}, \tilde{y}, \tilde{t}) e^{-i(\tilde{\rho}\tilde{x} + \tilde{\sigma}\tilde{y})} d\tilde{x} d\tilde{y}, \quad (3.6a)$$

$$\tilde{\eta}(\tilde{x}, \tilde{y}, \tilde{t}) = \frac{1}{(2\pi)^2} \int_{-\infty}^{\infty} \int_{-\infty}^{\infty} \tilde{\eta}(\tilde{\rho}, \tilde{\sigma}, \tilde{t}) e^{i(\tilde{\rho}\tilde{x} + \tilde{\sigma}\tilde{y})} d\tilde{\rho} d\tilde{\sigma}, \quad (3.6b)$$

and transformed the governing LSW Eq. 3.4 into an ordinary differential equation, through Eq. 3.6a as

$$\tilde{\eta}_{\tilde{t}\tilde{t}} + (\tilde{\rho}^2 + \tilde{\sigma}^2) \tilde{\eta} = 0, \quad (3.7)$$

where  $\tilde{\rho}$  and  $\tilde{\sigma}$  are the wavenumbers in  $\tilde{x}$ - and  $\tilde{y}$ - directions, respectively, and the Fourier transforms of the initial conditions (Eq. 3.5) are presented as

$$\tilde{\eta}(\tilde{\rho}, \tilde{\sigma}, \tilde{t} = 0) = \tilde{\eta}_0(\tilde{\rho}, \tilde{\sigma}), \quad (3.8a)$$

$$\tilde{\eta}_t(\tilde{\rho}, \tilde{\sigma}, \tilde{t} = 0) = 0. \quad (3.8b)$$

The solution of Eq. 3.7 in the Fourier space is then

$$\tilde{\eta}(\tilde{\rho}, \tilde{\sigma}, \tilde{t}) = \tilde{\eta}_0(\tilde{\rho}, \tilde{\sigma}) \cos \tilde{\omega} \tilde{t}, \quad (3.9)$$

where  $\tilde{\omega} = \sqrt{\tilde{\rho}^2 + \tilde{\sigma}^2}$ .

Aydın (2011) derived the analytical solution in the physical space by back-transformation of (3.9) through (3.6b) as

$$\tilde{\eta}(\tilde{x}, \tilde{y}, \tilde{t}) = \frac{1}{(2\pi)^2} \int_{-\infty}^{\infty} \int_{-\infty}^{\infty} \tilde{\eta}_0(\tilde{\rho}, \tilde{\sigma}) e^{i(\tilde{\rho}\tilde{x} + \tilde{\sigma}\tilde{y})} \cos \tilde{\omega} \tilde{t} d\tilde{\rho} d\tilde{\sigma}, \quad (3.10)$$

where  $\tilde{\eta}_0$  is Fourier transform of tsunami initial condition.

### 3.2 Two-dimensional $N$ -wave through Earthquake Source Parameters

In Chapter 2, the one-dimensional  $N$ -wave profile in terms of the earthquake source parameters was proposed, i.e., one-dimensional NEP (Eq. 2.22). In this section, the aim is to provide the two-dimensional  $N$ -wave profile with respect to the earthquake source parameters.

Kânoğlu et al. (2013) extended generalized  $N$ -wave profile (Eq. 2.1) into the second dimension and defined the two-dimensional finite crest length  $N$ -wave profile as

$$\tilde{\eta}_{NEP}(\tilde{x}, \tilde{y}) = \frac{1}{2} \tilde{\varepsilon}_{2D} \tilde{H}(\tilde{x} - \tilde{X}_2) \operatorname{sech}^2 \tilde{\gamma}(\tilde{x} - \tilde{X}_1) \times [\tanh \tilde{\gamma}(\tilde{y} + \tilde{L}/2) - \tanh \tilde{\gamma}(\tilde{y} - \tilde{L}/2)]. \quad (3.11)$$

where  $\tilde{L}$  refers to the dimensionless initial wave crest length, which is equal to the earthquake fault length. It is determined that varying the fault length directly affects the tsunami initial wave's crest length, and its effect on the initial wave height is negligible.  $\tilde{\varepsilon}_{2D}$  can be defined as

$$\tilde{\varepsilon}_{2D} = 2 \tilde{\varepsilon}_{1D} / [\tanh(\tilde{\gamma}\tilde{L}/2) - \tanh(-\tilde{\gamma}\tilde{L}/2)], \quad (3.12)$$

where  $\varepsilon_{1D}$  is given with Eq. 2.6. Substituting the non-dimensional form of Eq. 3.12, Eq. 2.11, Eq. 2.16, and Eq. 2.21 into the two-dimensional  $N$ -wave profile (Eq. 3.11) will provide the two-dimensional NEP in terms of the earthquake source parameters.

Fourier transform of the two-dimensional NEP profile (Eq. 3.11) is

$$\tilde{\eta}_{NEP}(\tilde{\rho}, \tilde{\sigma}) = i \frac{4\tilde{\varepsilon}_{2D}\tilde{H}}{\pi} \tilde{\alpha}^3 (e^{-i\tilde{\sigma}\tilde{L}} - 1) e^{-i(-\tilde{\sigma}\tilde{L}/2 + \tilde{\rho}\tilde{X}_1)} [(\tilde{X}_1 - \tilde{X}_2)\tilde{\rho} + i(1 - \tilde{\alpha}\tilde{\rho} \coth \tilde{\alpha}\tilde{\rho})] \operatorname{csch} \tilde{\alpha}\tilde{\sigma} \operatorname{csch} \tilde{\alpha}\tilde{\rho}, \quad (3.13)$$

where  $\tilde{\alpha} = \pi/(2\tilde{\gamma})$ .

In what follows, Eqs. 3.10 and 3.13 will be utilized to provide a tsunami propagation database.

### 3.3 Earthquake Source Scenarios

The aim is to provide a tsunami propagation database to explore the relationship between tsunami focusing and earthquake source parameters. Accordingly, 384 differ-

ent earthquake source scenarios are defined: similar to what was conducted in chapter 2; the strike angle is kept constant as  $\phi = 270^\circ$  to provide a leading depression  $N$ -wave regarding the coordinate system (see Figure 2.2). Furthermore, the rake angle is retained as  $\lambda = 90^\circ$  to generate maximum vertical displacement of the sea surface considering the physics of the fault plane. Then, the fault slip amount is ranged as 1, 5, 10, 15, and 20 m; the fault length is taken from 100 to 500 km by an interval of 100 km; the fault width is considered as 50, 100, and 150 km; and the fault depth as 10, 20, 30, and 40 km. As mentioned in chapter 2, the maximum depression wave amplitude (trough) decreases in the initial profile by increasing the dip angle. The depression part almost disappears at the dip angle of  $40^\circ$ . Consequently, the dip angle is taken from  $10^\circ$  up to  $35^\circ$  by the interval of  $5^\circ$ . The range of earthquake source scenarios is summarized in Table 3.1.

Table 3.1: Range of earthquake source scenarios used in propagation database.

Fault Plane Parameter	Value
Strike angle ( $\phi$ )	$270^\circ$
Rake angle ( $\lambda$ )	$90^\circ$
Dip angle ( $\delta$ )	$10 - 35^\circ$ , $5^\circ$ increments
Slip amount ( $u$ )	1, 5, 10, 15, 20 m
Fault length ( $L$ )	100 – 500 km, 100 km increments
Fault width ( $W$ )	50 – 150 km, 50 km increments
Fault depth ( $d$ )	10 – 40 km, 10 km increments

The following empirical equations are used to calculate the moment magnitude of the earthquake scenarios (Johnson 1998; Synolakis et al. 1997).

$$M_w = (2/3) \log M_0 - 6.03, \quad (3.14a)$$

$$M_0 = \mu u L W, \quad (3.14b)$$

where  $M_0$  is seismic moment,  $\mu$  refers to rigidity of the earth ( $\text{N/m}^2$ ),  $u$  is the slip amount (m),  $L$  is the fault length (m), and  $W$  is the fault width (m). Rigidity depends primarily on the geological properties, i.e., whether the fault is on soft sediment or hard rock. This study uses a typical rigidity of  $4.0 \times 10^{10} \text{ N/m}^2$  (Johnson 1998). The moment magnitude for the earthquake scenarios stands as  $7.5 \leq M_w \leq 9.0$ .

In this chapter, the finite-crested two-dimensional NEP profiles (Eq. 3.11) are calculated as tsunamis' initial waves using defined earthquake source scenarios in terms of the fault plane parameters. Then, using Eq. 3.10, Fourier transforms (Eq. 3.13) of the calculated profiles are propagated over a constant depth ocean of  $h = 3000$  m to study the tsunami focusing phenomenon. The propagation results are used to determine how and to what extent the earthquake source parameters can cause variation in the amplitude and location of the focusing point. The maximum wave envelope profiles are calculated by monitoring the largest wave height at each spatial location for the propagation database. Then, the connection between focusing amplitude and earthquake source parameters and the connection between focusing distance and fault plane parameters are analyzed.

### 3.4 Results and Discussions

A tsunami propagation database, including maximum wave envelopes for 384 earthquake source scenarios, is provided. Here, the maximum wave envelopes along the bisector are used, i.e.,  $x$ -direction. Then, the impact of the earthquake source parameters, e.g., the slip amount ( $u$ ), the fault depth ( $d$ ), the dip angle ( $\delta$ ), the fault length ( $L$ ), the fault width ( $W$ ), and the tsunami aspect ratio ( $L/W$ ) on the variation of amplitude and location of the focusing point are studied one by one. It is essential to note that  $x$ -axis is referenced to the zero crossing of  $N$ -wave and the negative direction is toward the shoreline (see Figure 3.3).

### 3.4.1 Focusing through the slip amount

The effect of slip amount on focusing amplitude and focusing distance is examined in this section. Figures 3.4 and 3.5 indicate the effect of slip amount on focusing amplitude. While the first plot shows information for the fault depth of  $d = 20$  km and the latter for the fault depth of  $d = 40$  km, the fault length is  $L = 300$  km, the dip angle varies from  $\delta = 10^\circ$  to  $\delta = 35^\circ$ , and the fault widths are  $W = 50, 100$ , and  $150$  km in both graphs.

There is a linear relation between focusing amplitude and the slip amount (Figures 3.4 and 3.5). As expected, the focusing amplitude tends to rise by increasing the slip amount. Notice that almost all results for different dip angles fall over each other for deeper earthquakes ( $d = 40$  km), which implies that the focusing amplitude is not much sensitive to the dip angle after a certain fault depth (Figure 3.5).

Figures 3.6 and 3.7 show the relation between focusing distance and slip amount. Again, while the first plot indicates information for  $d = 20$  km and the second for  $d = 40$  km fault depth, the dip angle varies from  $\delta = 10^\circ$  to  $\delta = 35^\circ$ , the fault width is  $W = 50, 100$ , and  $150$  km, and the fault length is  $L = 300$  km in both graphs. The results reveal that the focusing distance is not sensitive to the slip amount and remains constant for different slips.



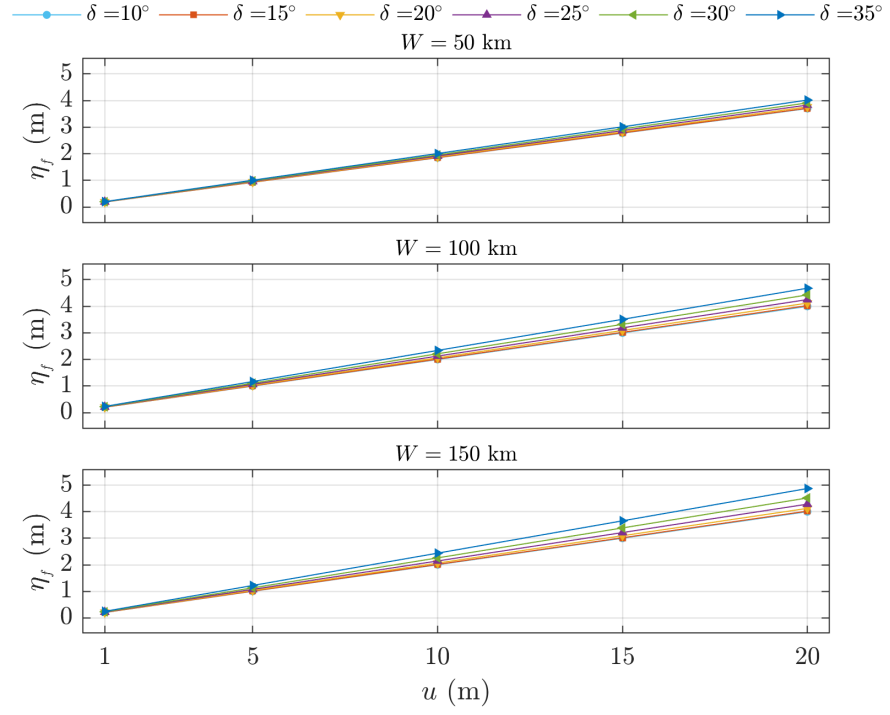


Figure 3.4: Relation of the focusing amplitude to the slip amount. The fault length is  $L = 300$  km and the fault depth is  $d = 20$  km.

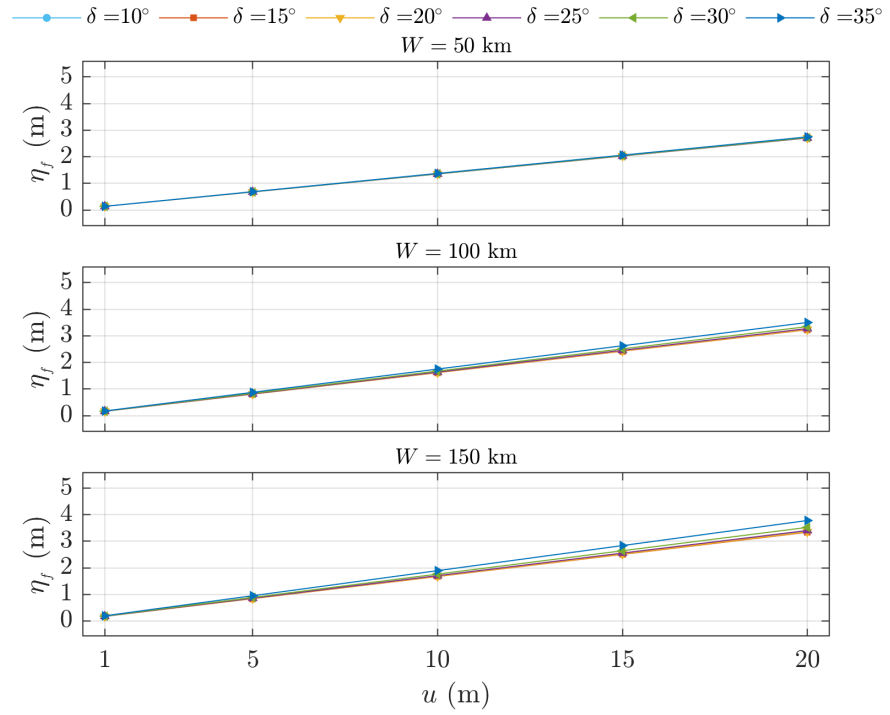


Figure 3.5: Relation of the focusing amplitude to the slip amount. The fault length is  $L = 300$  km and the fault depth is  $d = 40$  km.

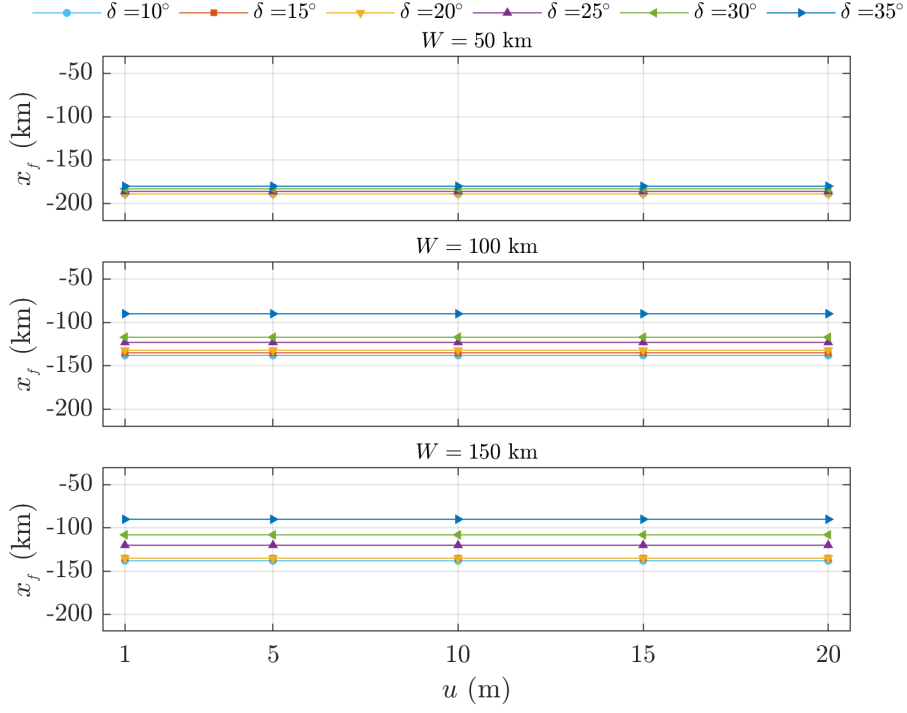


Figure 3.6: Relation of the focusing distance to the slip amount. The fault length is  $L = 300$  km and the fault depth is  $d = 20$  km.

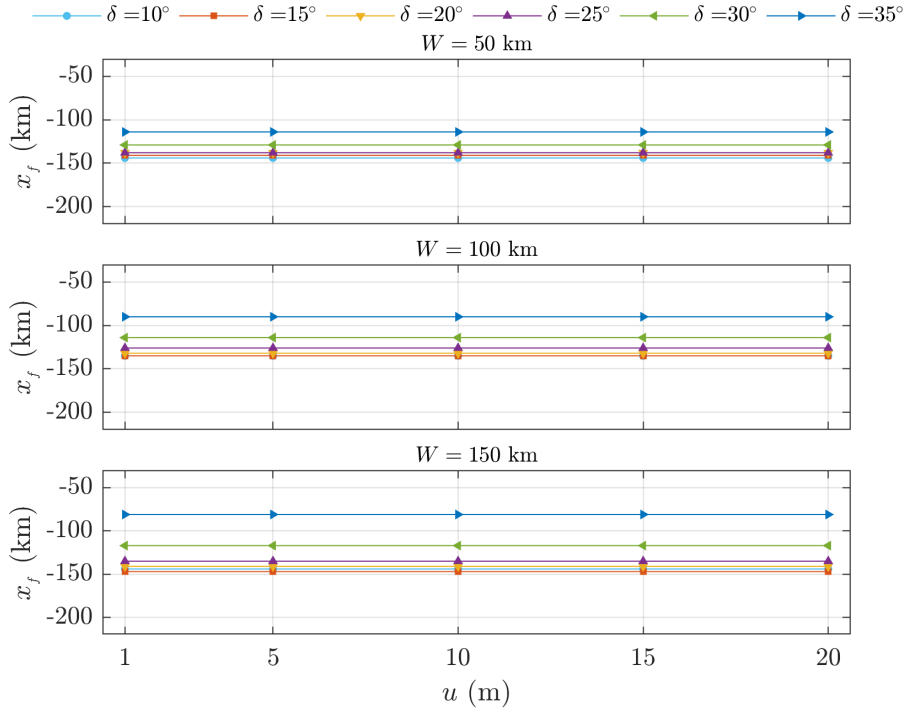


Figure 3.7: Relation of the focusing distance to the slip amount. The fault length is  $L = 300$  km and the fault depth is  $d = 40$  km.

### 3.4.2 Focusing through the fault depth

The effect of the fault depth on focusing amplitude can be observed in Figures 3.8 to 3.13. Figures 3.8, 3.9, 3.10, 3.11, and 3.12 indicate results for the fault length of  $L = 100, 200, 300, 400$ , and  $500$  km, respectively. Focusing amplitude almost linearly decreases with increasing the fault depth. Further, focusing amplitude seems to get less sensitive to the dip angle as fault depth increases. Figure 3.13 again illustrates the focusing amplitude-fault depth relationship for different fault lengths, this time by keeping the dip angle  $\delta = 15^\circ$  constant and varying the fault width as  $W = 50, 100$ , and  $150$  km.

Following Figures 3.14 to 3.19, the focusing distance is not much sensitive to the fault depth for the sources with small fault length and tsunami aspect ratios; however, by increasing the fault length and tsunami aspect ratios, focusing distance gets more sensitive to the fault depth. The results reveal that the focusing point gets farther from the tsunami source, closer to the shoreline, for larger tsunami aspect ratios. It can be stated that focusing distance ( $|x_f|$ ) tends to decrease by increasing the fault depth for sources with larger tsunami aspect ratios.

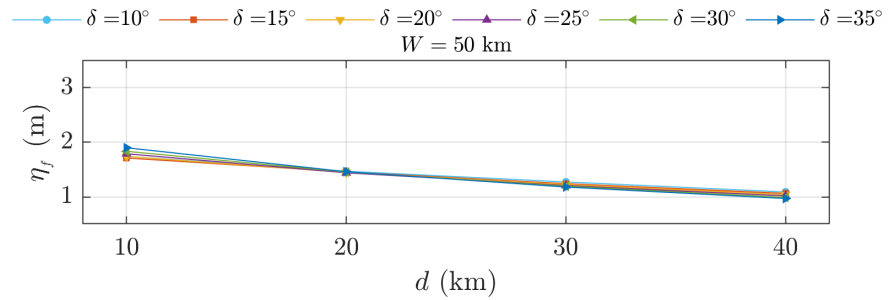


Figure 3.8: Relation of the focusing amplitude to the fault depth. The fault length is  $L = 100$  km and the slip amount  $u = 10$  m.

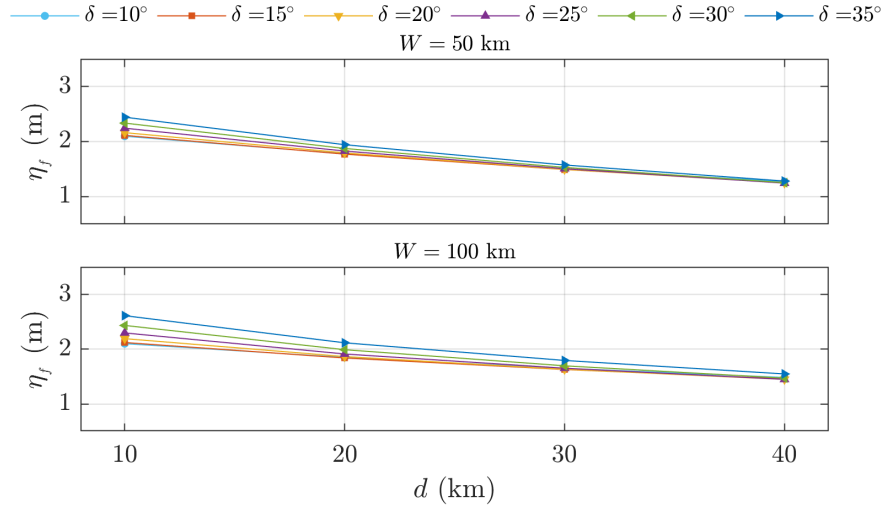


Figure 3.9: Relation of the focusing amplitude to the fault depth. The fault length is  $L = 200$  km and the slip amount  $u = 10$  m.

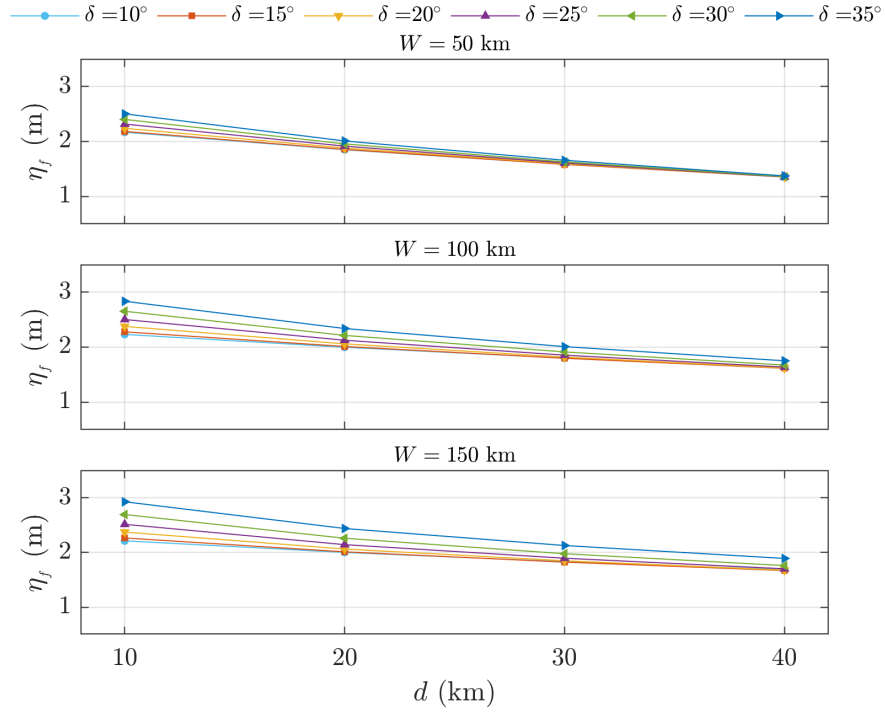


Figure 3.10: Relation of the focusing amplitude to the fault depth. The fault length is  $L = 300$  km and the slip amount  $u = 10$  m.

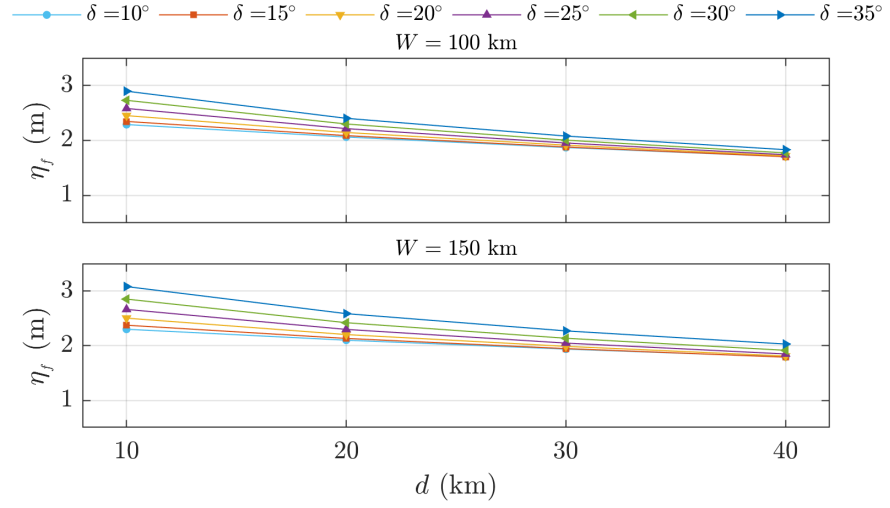


Figure 3.11: Relation of the focusing amplitude to the fault depth. The fault length is  $L = 400 \text{ km}$  and the slip amount  $u = 10 \text{ m}$ .

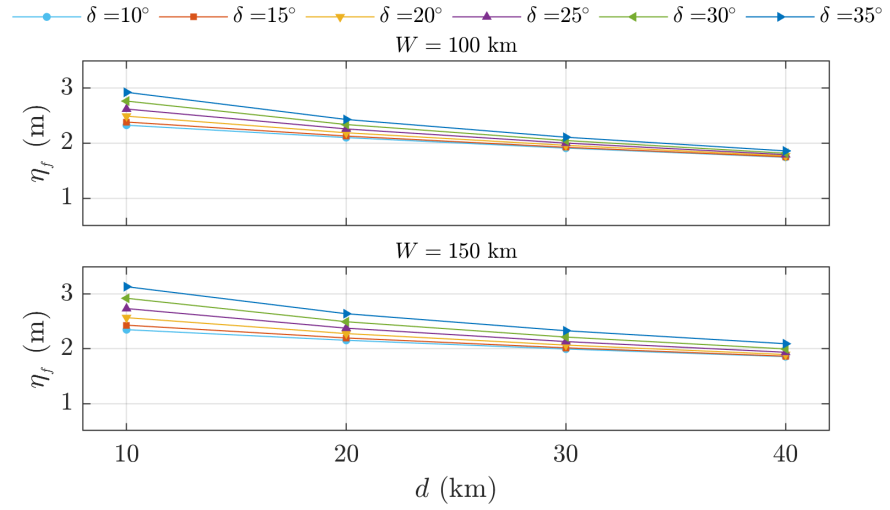


Figure 3.12: Relation of the focusing amplitude to the fault depth. The fault length is  $L = 500 \text{ km}$  and the slip amount  $u = 10 \text{ m}$ .

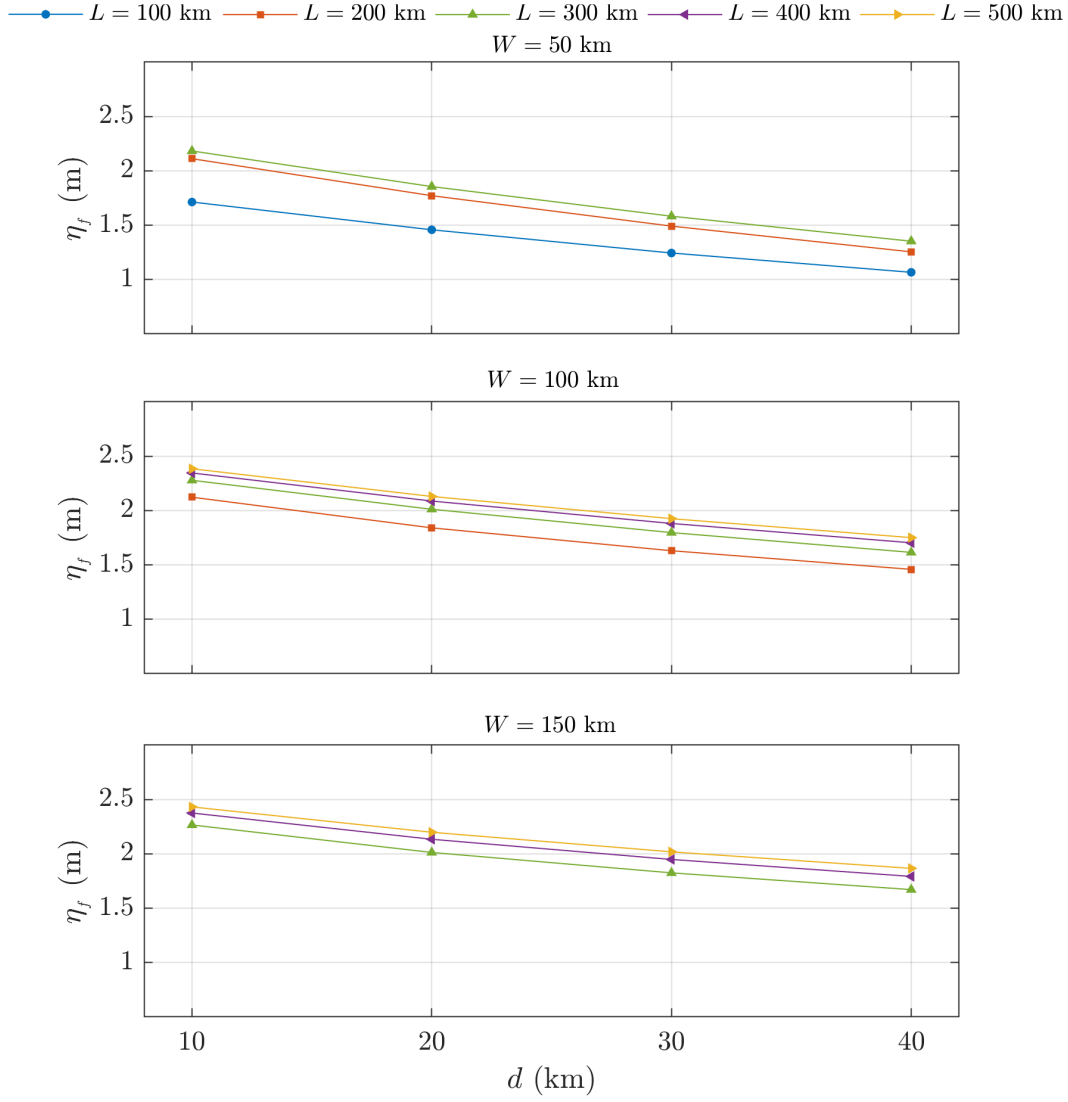


Figure 3.13: Relation of the focusing amplitude to the fault depth. The dip angle is  $\delta = 15^\circ$ , and the slip amount  $u = 10$  m.

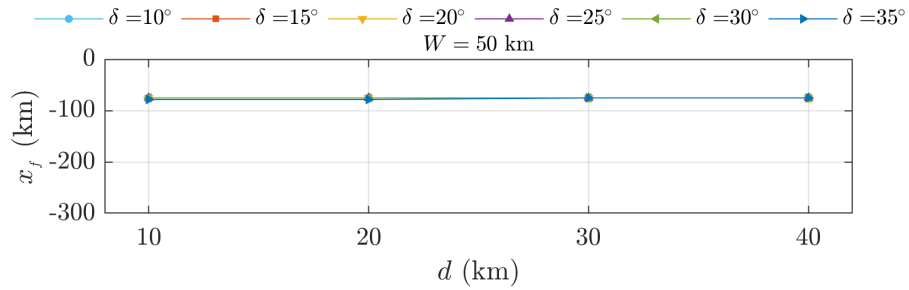


Figure 3.14: Relation of the focusing distance to the fault depth. The fault length is  $L = 100$  km and the slip amount  $u = 10$  m.

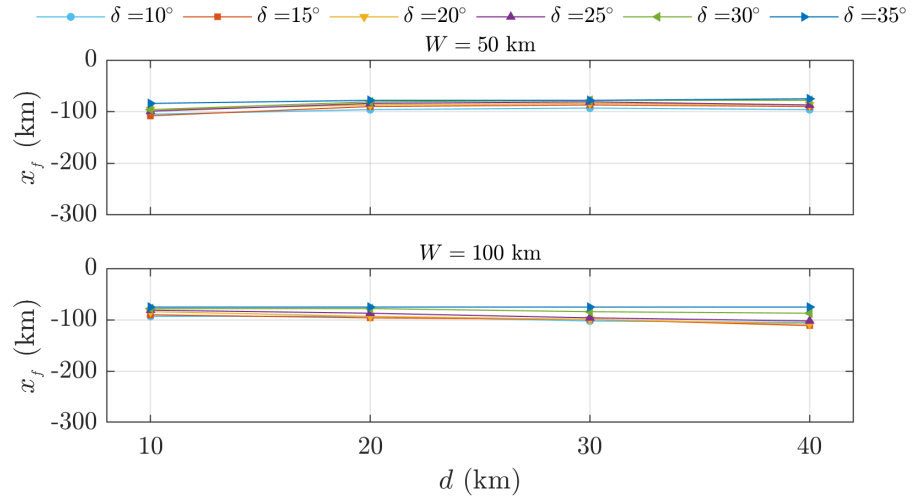


Figure 3.15: Relation of the focusing distance to the fault depth. The fault length is  $L = 200$  km and the slip amount  $u = 10$  m.

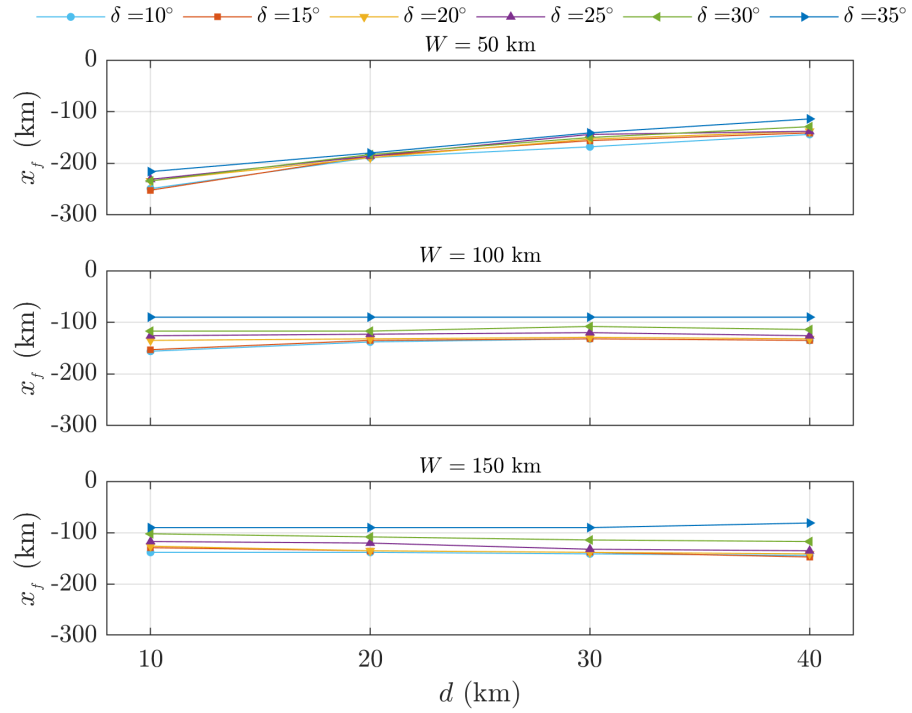


Figure 3.16: Relation of the focusing distance to the fault depth. The fault length is  $L = 300$  km and the slip amount  $u = 10$  m.

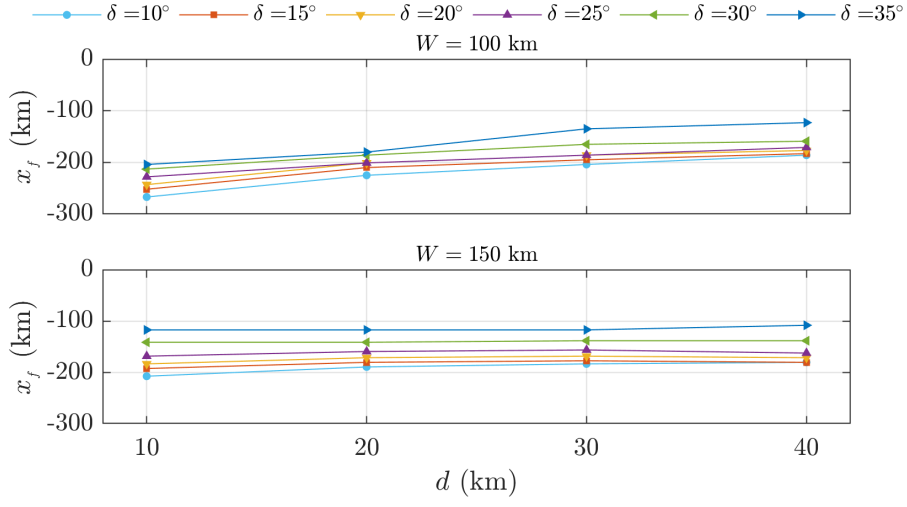


Figure 3.17: Relation of the focusing distance to the fault depth. The fault length is  $L = 400$  km and the slip amount  $u = 10$  m.

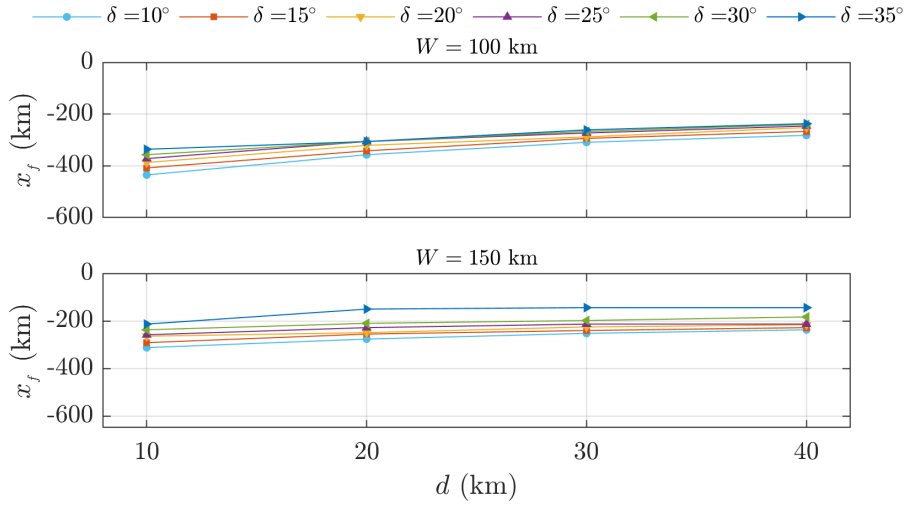


Figure 3.18: Relation of the focusing distance to the fault depth. The fault length is  $L = 500$  km and the slip amount  $u = 10$  m.



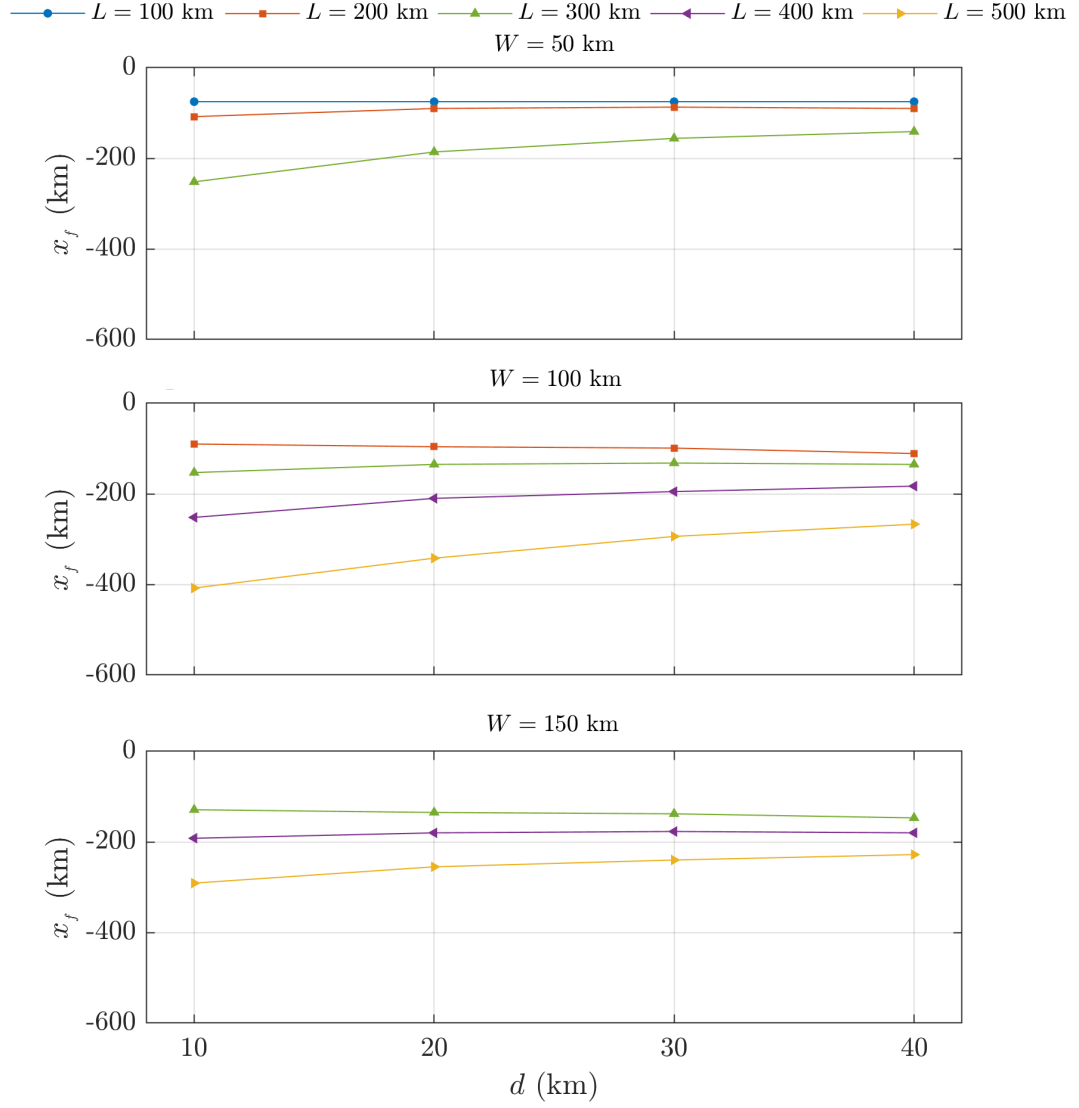


Figure 3.19: Relation of the focusing distance to the fault depth. The dip angle is  $\delta = 15^\circ$ , and the slip amount  $u = 10$  m.

### 3.4.3 Focusing through the dip angle

Figures 3.20 to 3.25 show that focusing amplitude increases slightly by rising the dip angle. The most significant increase in focusing amplitude against the dip angle is related to the shallower earthquake with larger fault width. The focusing amplitude almost remains constant for the source with smaller fault width and deeper faults, e.g.,  $W = 50$  km and  $d = 40$  km.

There is a gradual decrease in focusing distance by increasing the dip angle for the tsunami source by fault length of  $L = 200$  and  $L = 300$  km (Figures 3.27, 3.28, and 3.31). As tsunami source length increases, the focusing distance decreases against the dip angle at a more significant rate, e.g., for the source lengths of  $L = 400$  and  $L = 500$  km, drops in focusing distance are more evident (Figures 3.29, 3.30, and 3.31). Nevertheless, the focusing distance remains constant against the dip angle for a tsunami source with a fault length of  $L = 100$  km and fault width of  $W = 50$  km (Figure 3.26).

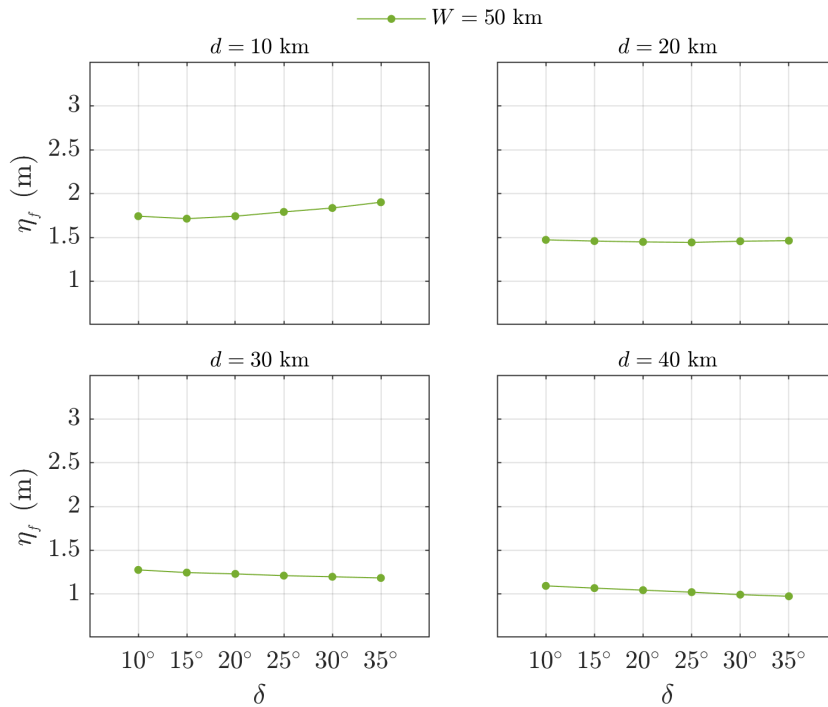


Figure 3.20: Relation of the focusing amplitude to the dip angle. The fault length is  $L = 100$  km and the slip amount  $u = 10$  m.

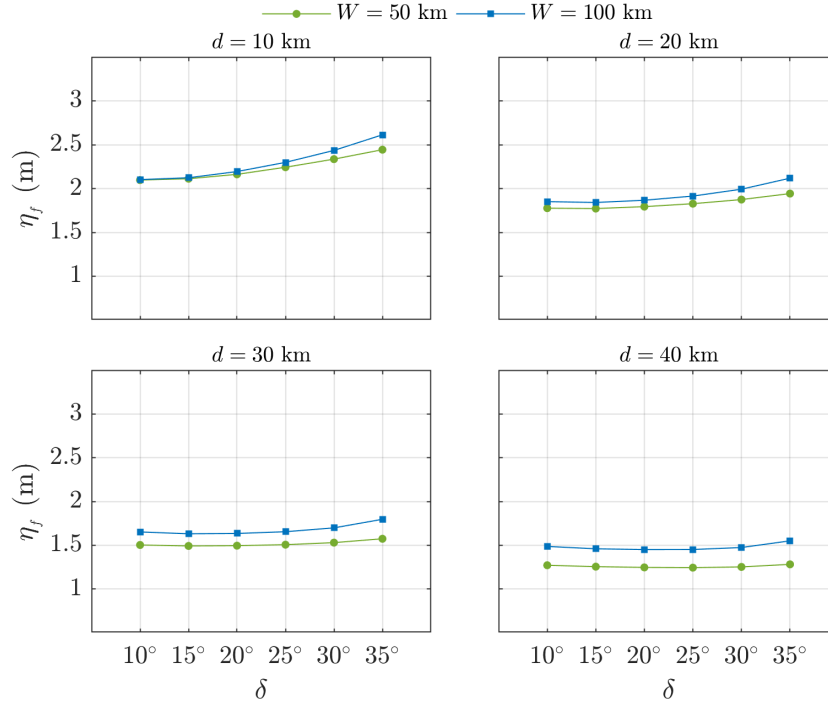


Figure 3.21: Relation of the focusing amplitude to the dip angle. The fault length is  $L = 200$  km and the slip amount  $u = 10$  m.

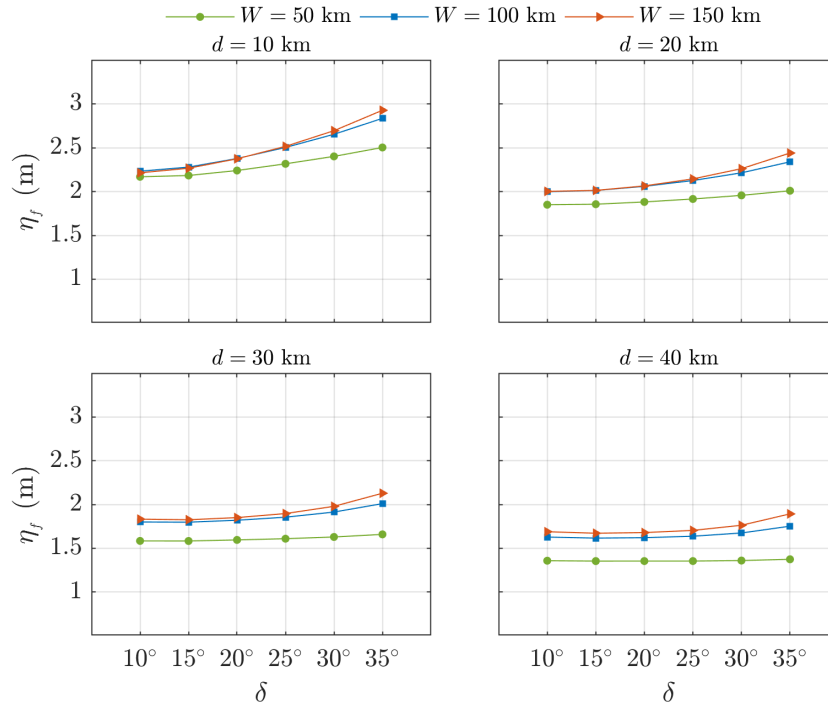


Figure 3.22: Relation of the focusing amplitude to the dip angle. The fault length is  $L = 300$  km and the slip amount  $u = 10$  m.

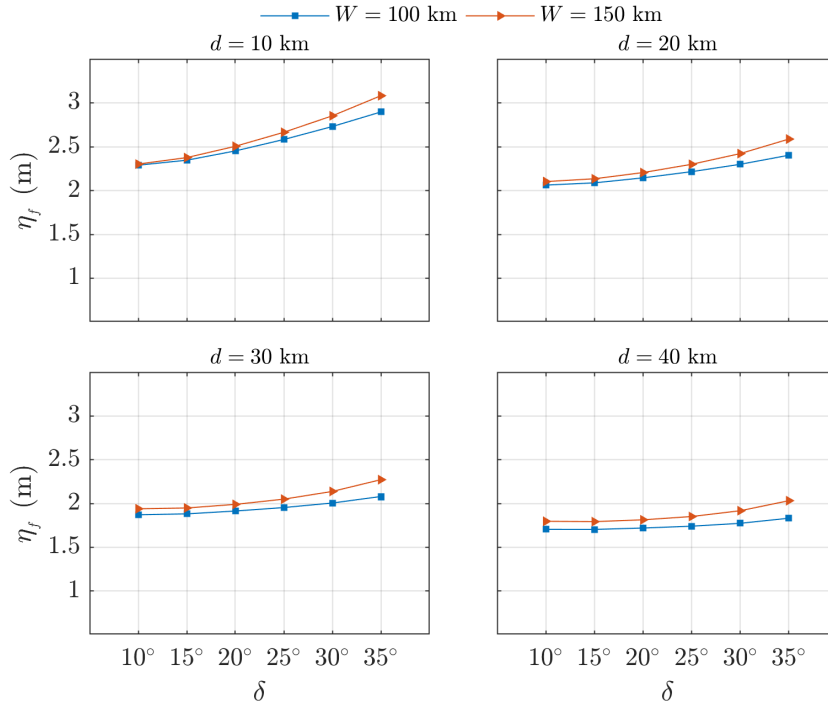


Figure 3.23: Relation of the focusing amplitude to the dip angle. The fault length is  $L = 400$  km and the slip amount  $u = 10$  m.

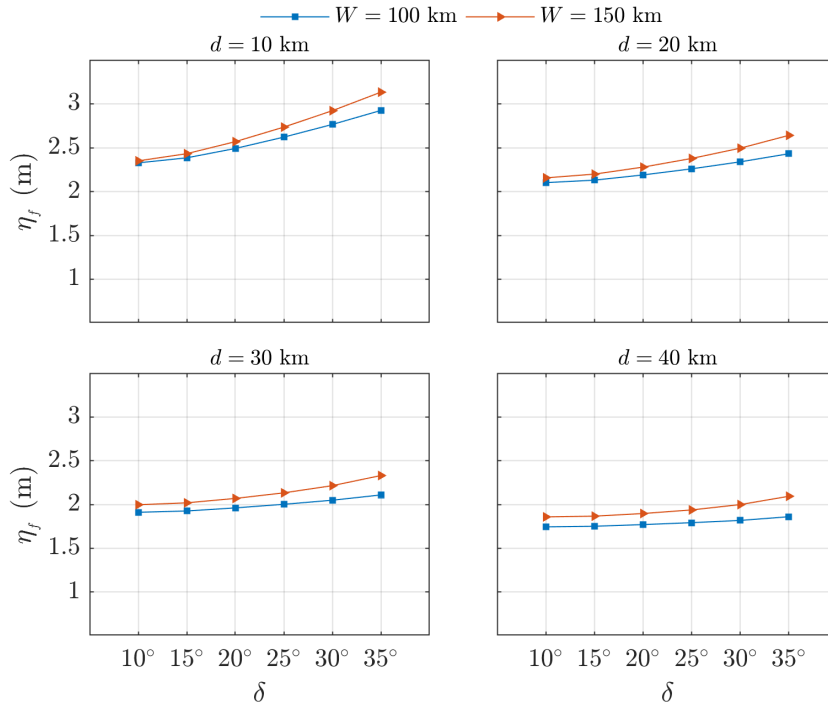


Figure 3.24: Relation of the focusing amplitude to the dip angle. The fault length is  $L = 500$  km and the slip amount  $u = 10$  m.

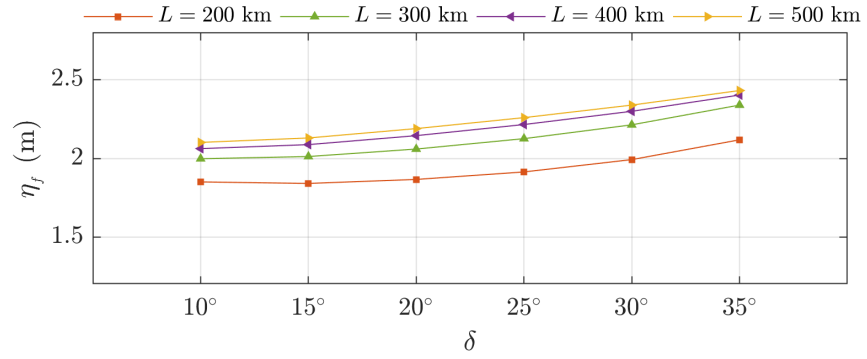


Figure 3.25: Relation of the focusing amplitude to the dip angle. The fault width is  $W = 100$  km, the fault depth is  $d = 20$  km and the slip amount  $u = 10$  m.

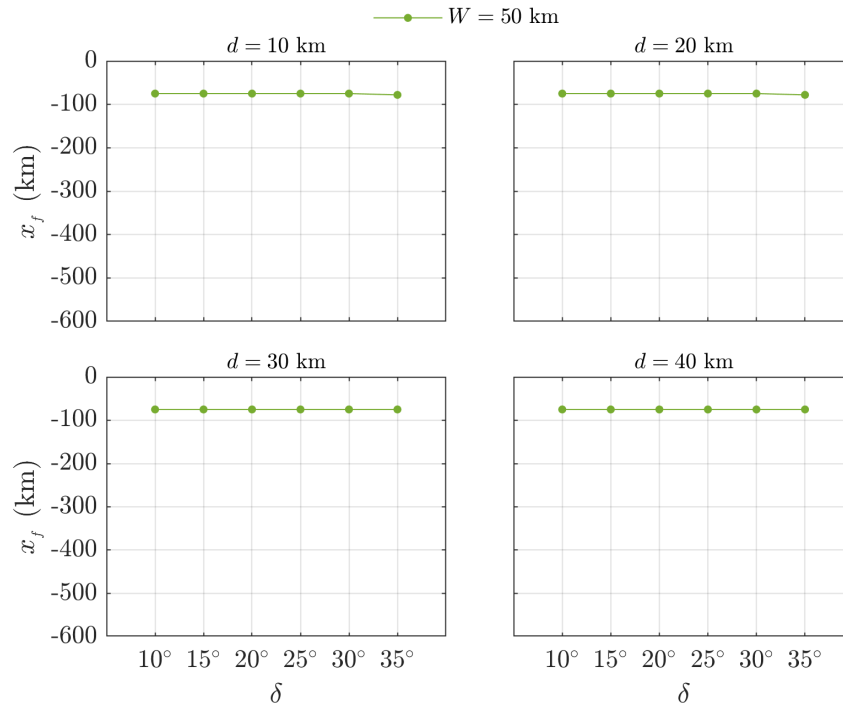


Figure 3.26: Relation of the focusing distance to the dip angle. The fault length is  $L = 100$  km and the slip amount  $u = 10$  m.

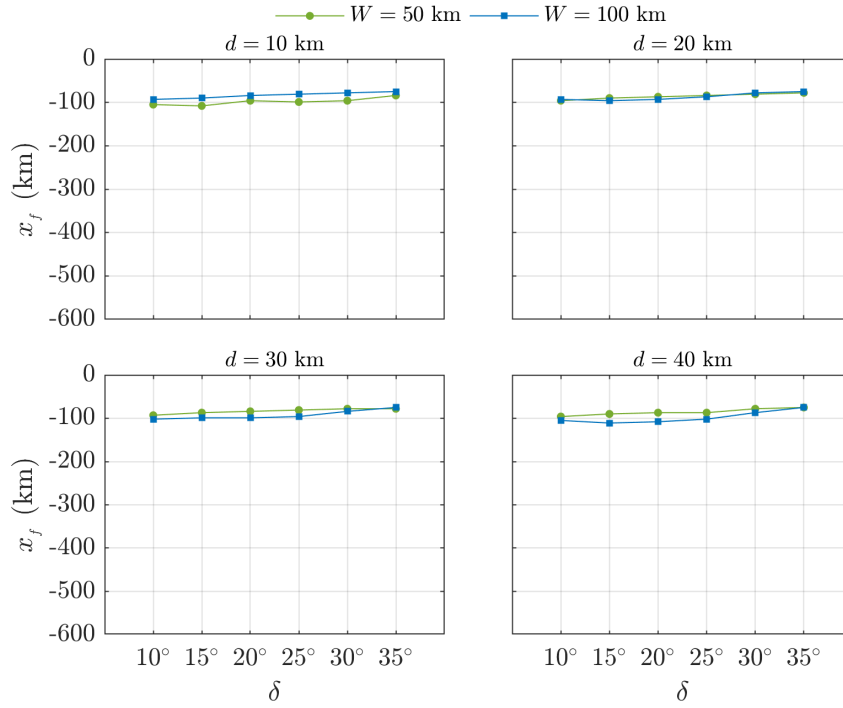


Figure 3.27: Relation of the focusing distance to the dip angle. The fault length is  $L = 200$  km and the slip amount  $u = 10$  m.

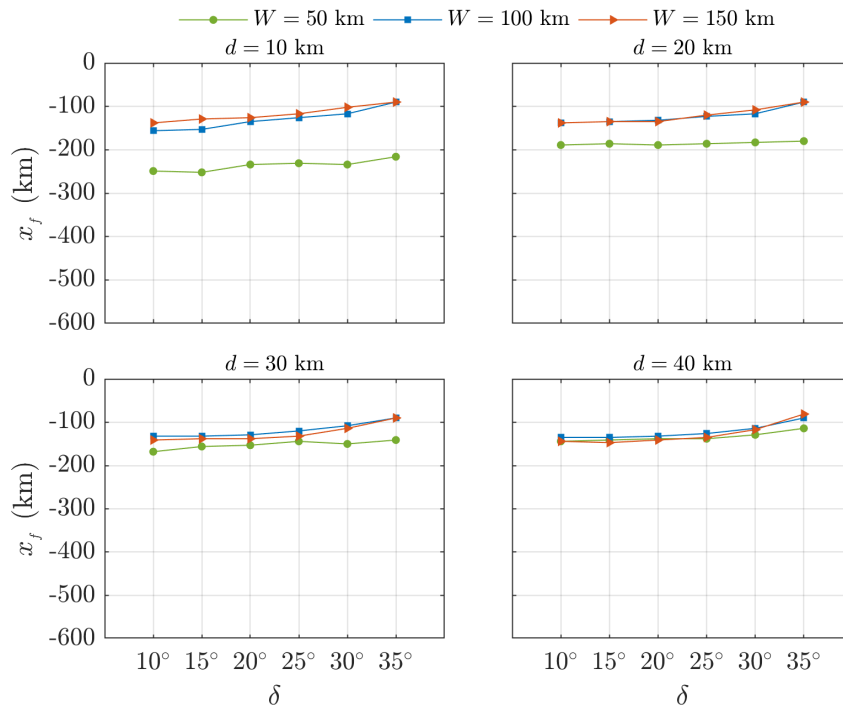


Figure 3.28: Relation of the focusing distance to the dip angle. The fault length is  $L = 300$  km and the slip amount  $u = 10$  m.

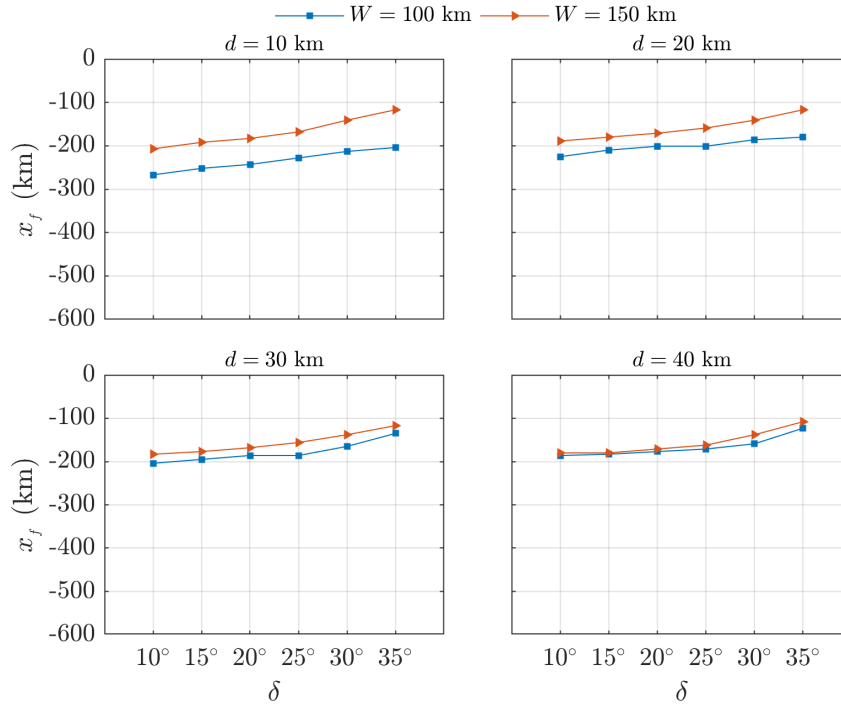


Figure 3.29: Relation of the focusing distance to the dip angle. The fault length is  $L = 400$  km and the slip amount  $u = 10$  m.

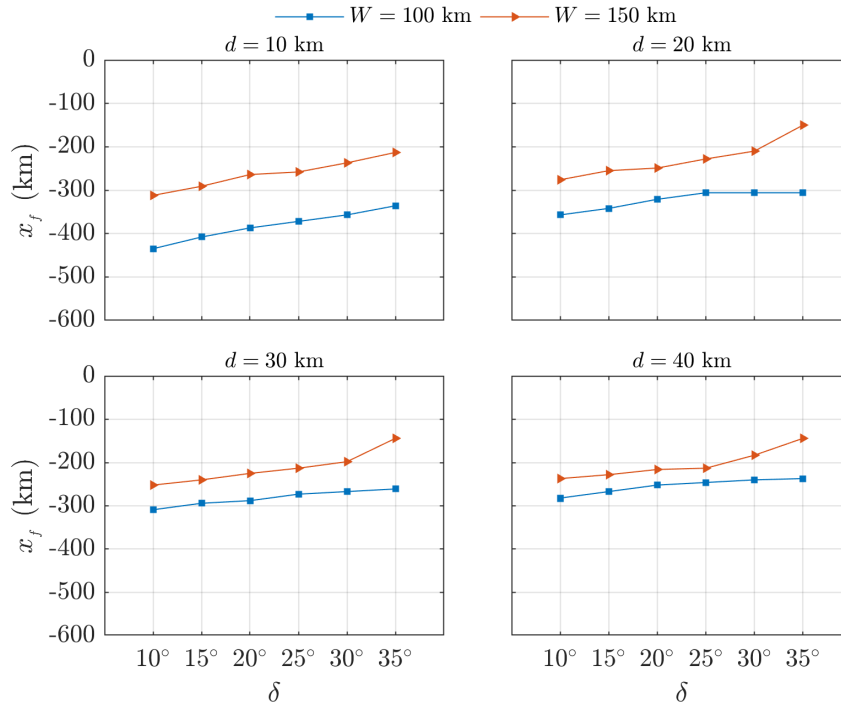


Figure 3.30: Relation of the focusing distance to the dip angle. The fault length is  $L = 500$  km and the slip amount  $u = 10$  m.

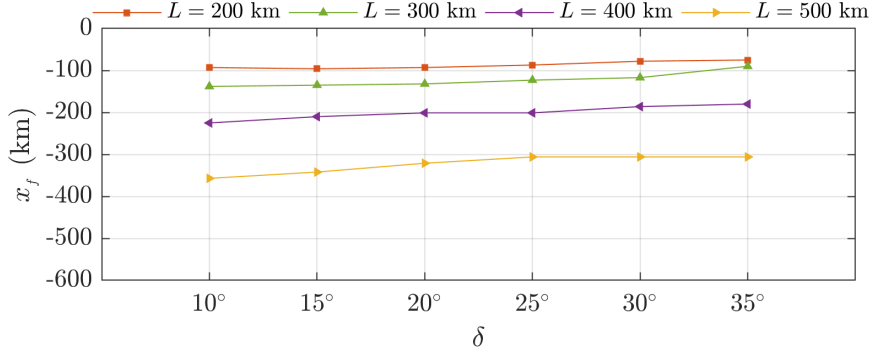


Figure 3.31: Relation of the focusing distance to the dip angle. The fault width is  $W = 100$  km, the fault depth is  $d = 20$  km, and the slip amount  $u = 10$  m.

#### 3.4.4 Focusing through the fault length

Considering Figures 3.32, 3.33, and 3.34, focusing amplitude increases slightly by increasing the fault length, except for the fault lengths from  $L = 100$  to  $L = 200$  km, in which the rate of change is much pronounced. Further, for  $L = 400$  to  $L = 500$  km, focusing amplitude remains almost constant (very slight increase) against the fault length, which implies that after a certain value of  $L$ , focusing amplitude is not much sensitive to the fault length. These results are consistent with Aydın (2018) and Kânoğlu et al. (2013).

Tsunami focusing is an impact of the finite crest length initial profile. Analyzing Figures 3.35, 3.36, and 3.37, it can be inferred that focusing distance increases by expanding the fault length, i.e., the crest length of the tsunami. Hence, the focusing point gets farther from the tsunami source and reaches closer to the shoreline, implying a sharp increase in focusing distance for elongated tsunami sources. Again, the results align with Aydın (2018) and Kânoğlu et al. (2013).



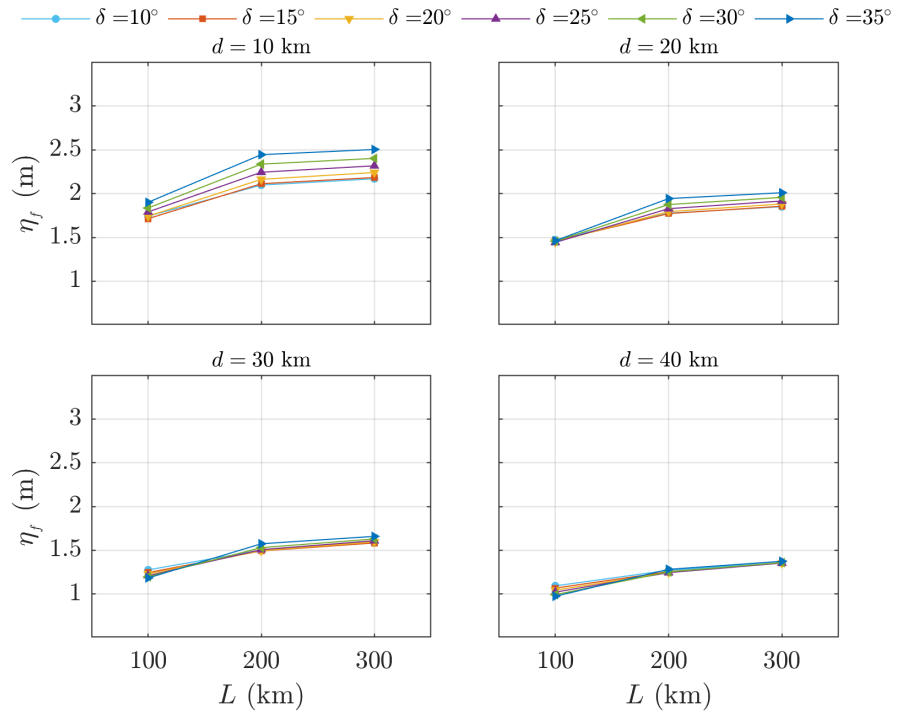


Figure 3.32: Relation of the focusing amplitude to the fault length. The fault width is  $W = 50$  km and the slip amount  $u = 10$  m.

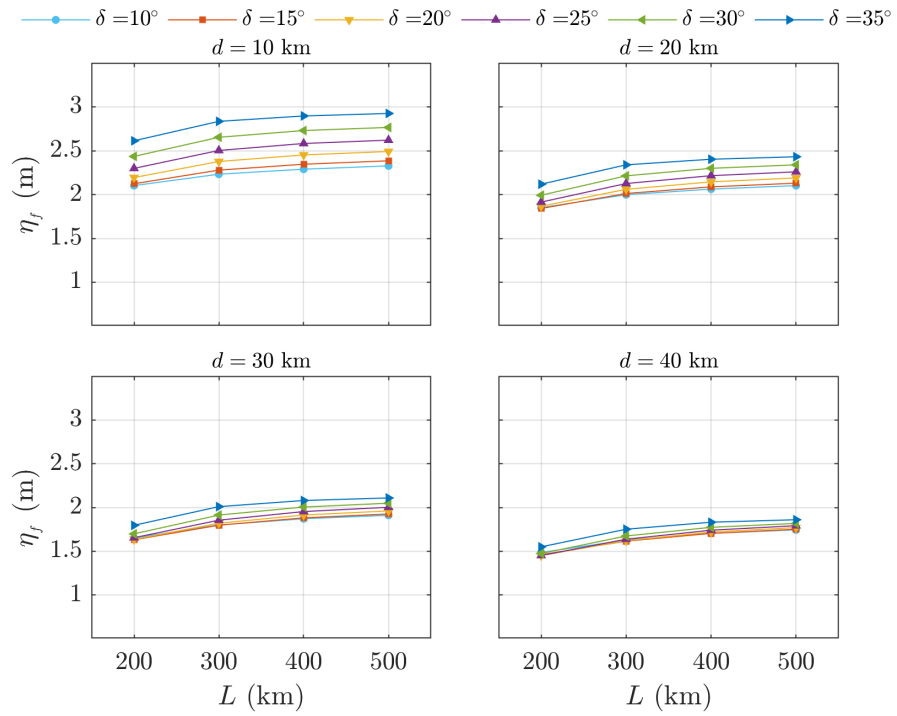


Figure 3.33: Relation of the focusing amplitude to the fault length. The fault width is  $W = 100$  km and the slip amount  $u = 10$  m.

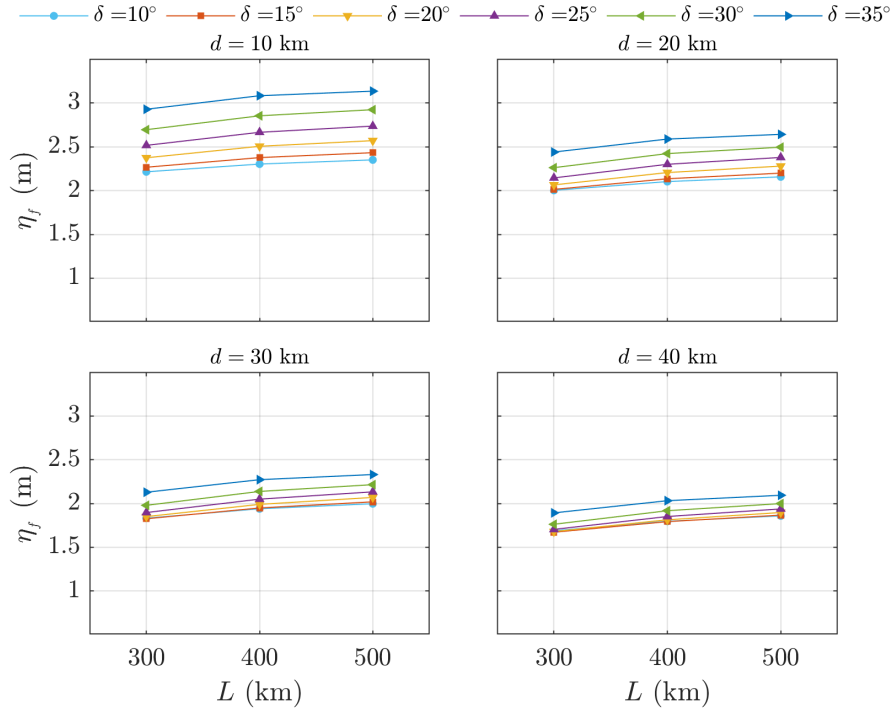


Figure 3.34: Relation of the focusing amplitude to the fault length. The fault width is  $W = 150$  km and the slip amount  $u = 10$  m.

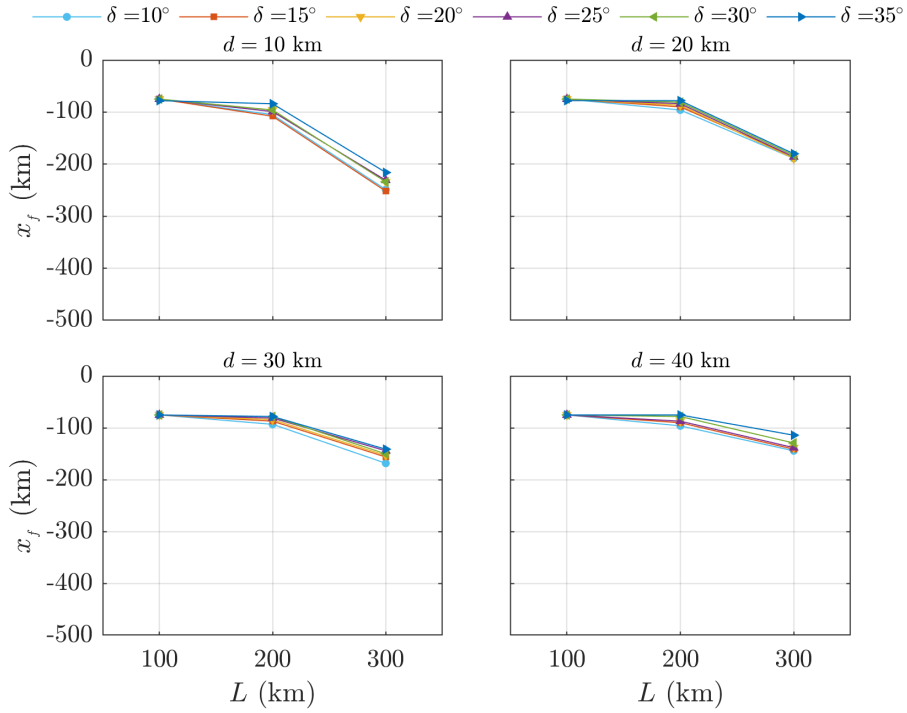


Figure 3.35: Relation of the focusing distance to the fault length. The fault width is  $W = 50$  km and the slip amount  $u = 10$  m.

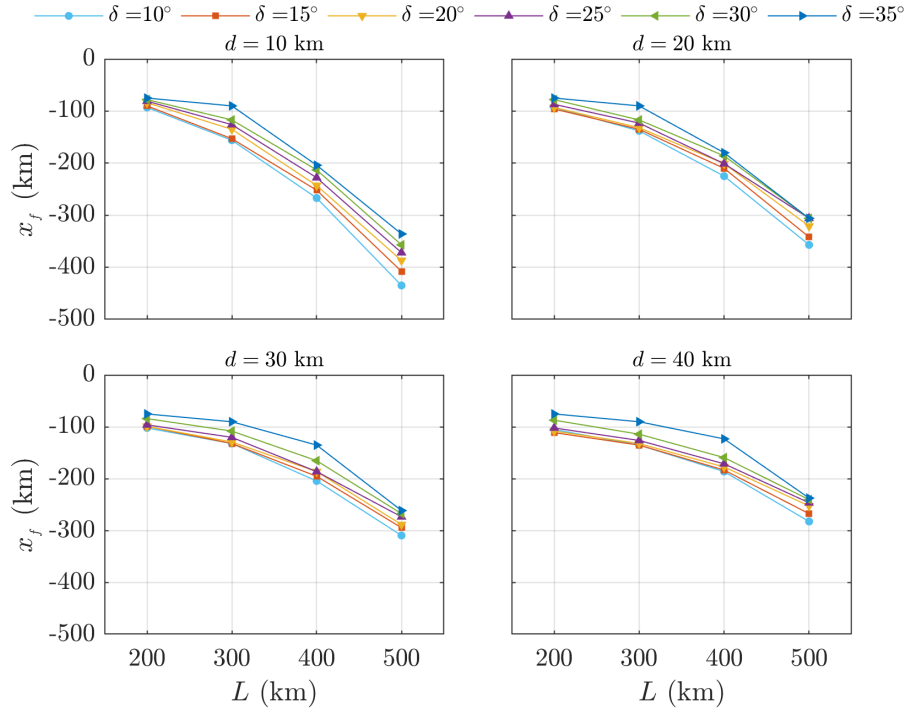


Figure 3.36: Relation of the focusing distance to the fault length. The fault width is  $W = 100$  km and the slip amount  $u = 10$  m.

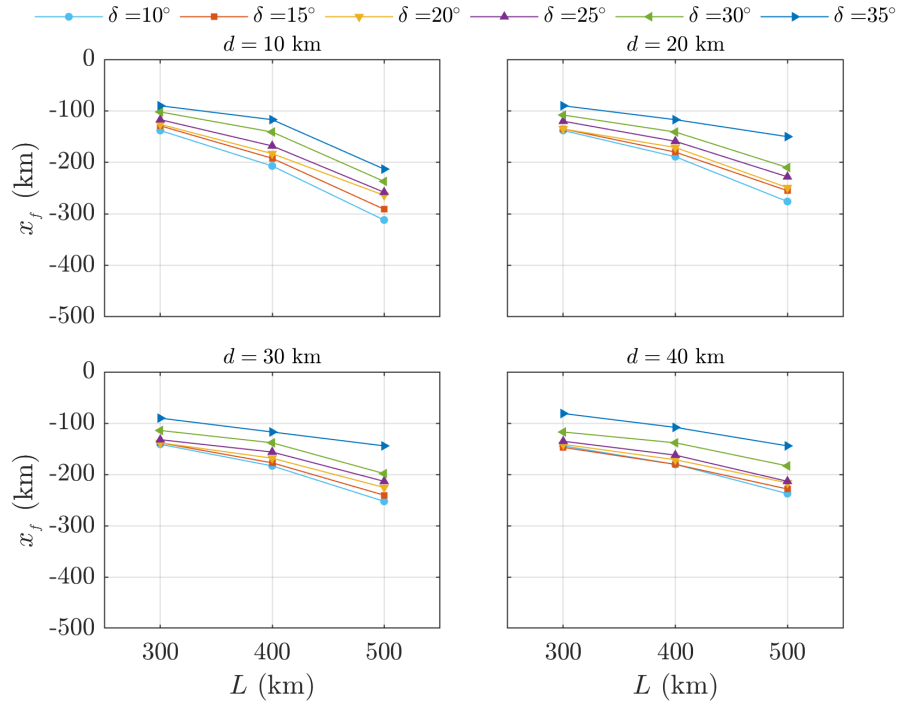


Figure 3.37: Relation of the focusing distance to the fault length. The fault width is  $W = 150$  km and the slip amount  $u = 10$  m.

### 3.4.5 Focusing through the fault width

The focusing amplitude rises by increasing the fault width, especially for the larger dip angles (Figures 3.38 to 3.41). Further, figures 3.42 to 3.45 indicate that the focusing distance tends to decrease by increasing the fault width.

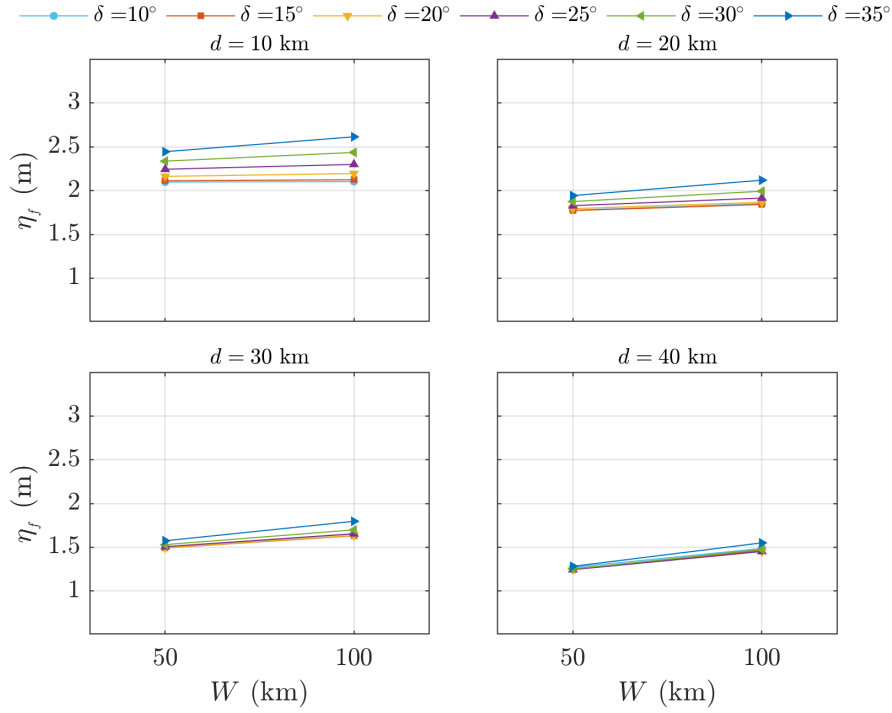


Figure 3.38: Relation of the focusing amplitude to the fault width. The fault length is  $L = 200$  km and the slip amount  $u = 10$  m.

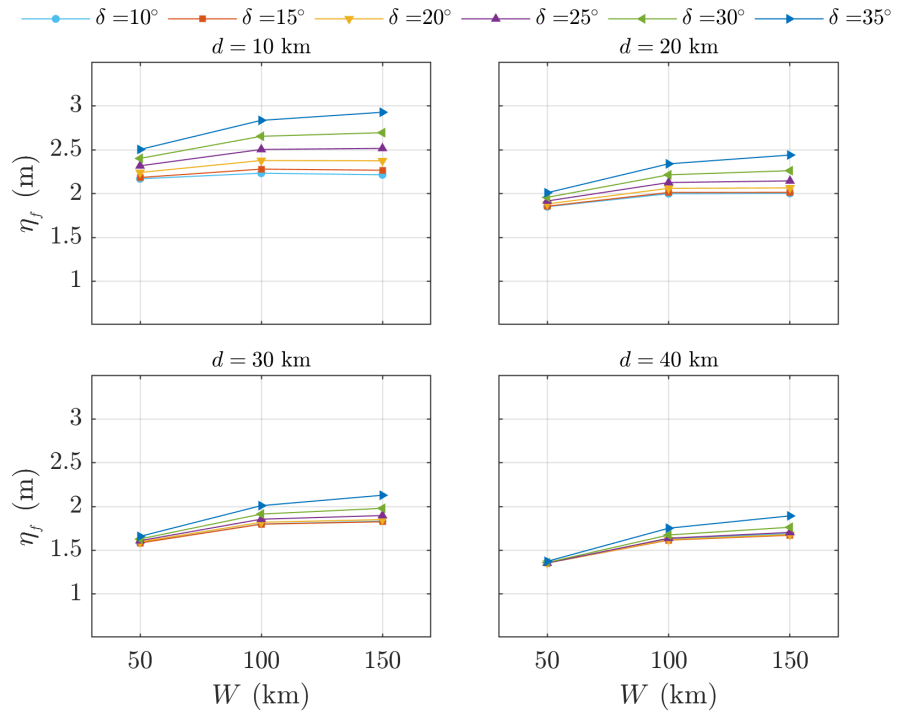


Figure 3.39: Relation of the focusing amplitude to the fault width. The fault length is  $L = 300$  km and the slip amount  $u = 10$  m.

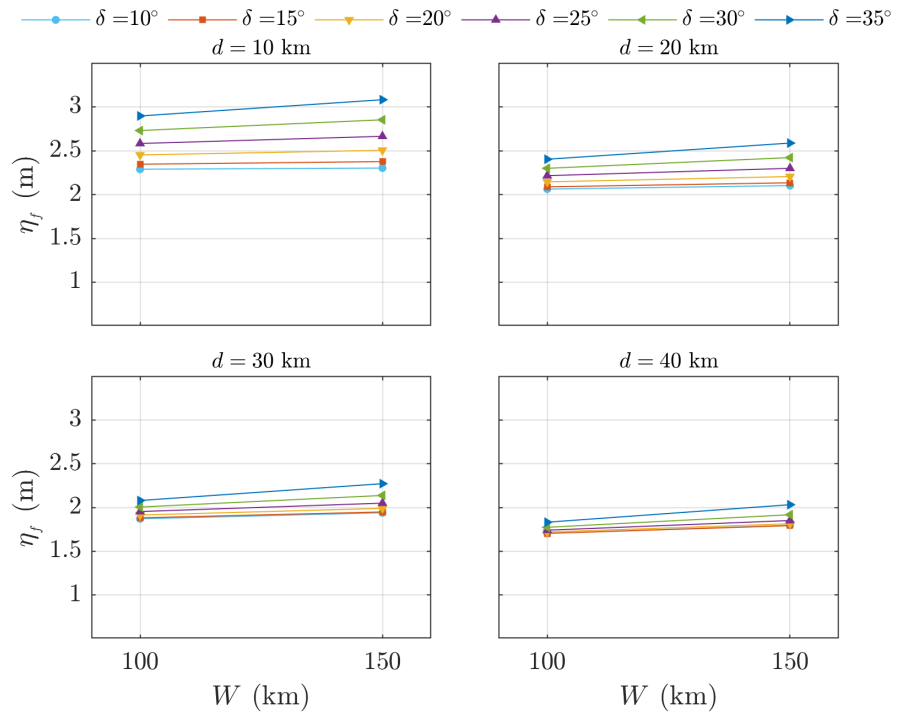


Figure 3.40: Relation of the focusing amplitude to the fault width. The fault length is  $L = 400$  km and the slip amount  $u = 10$  m.

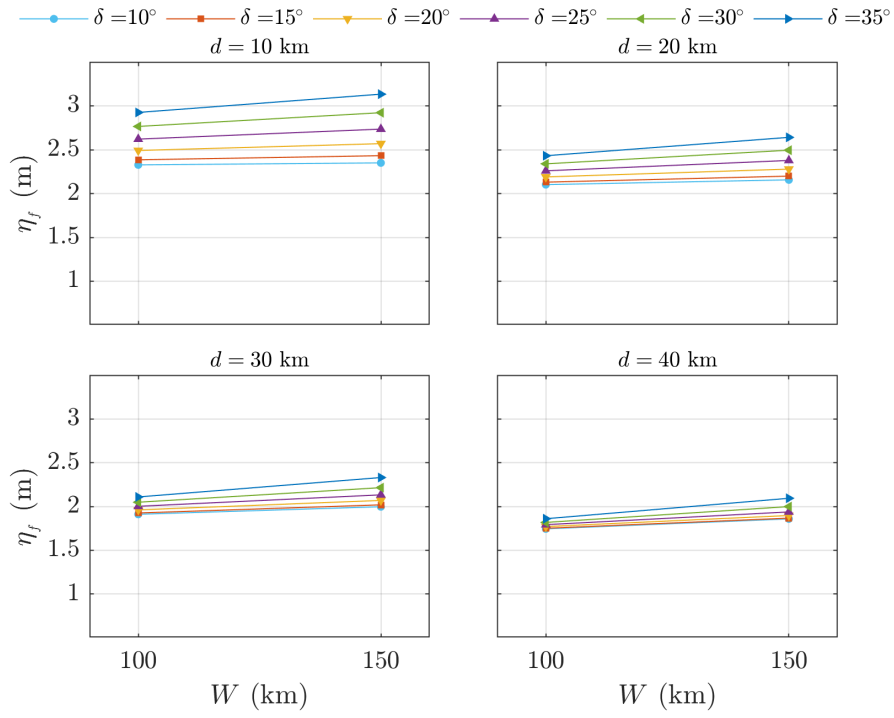


Figure 3.41: Relation of the focusing amplitude to the fault width. The fault length is  $L = 500$  km and the slip amount  $u = 10$  m.

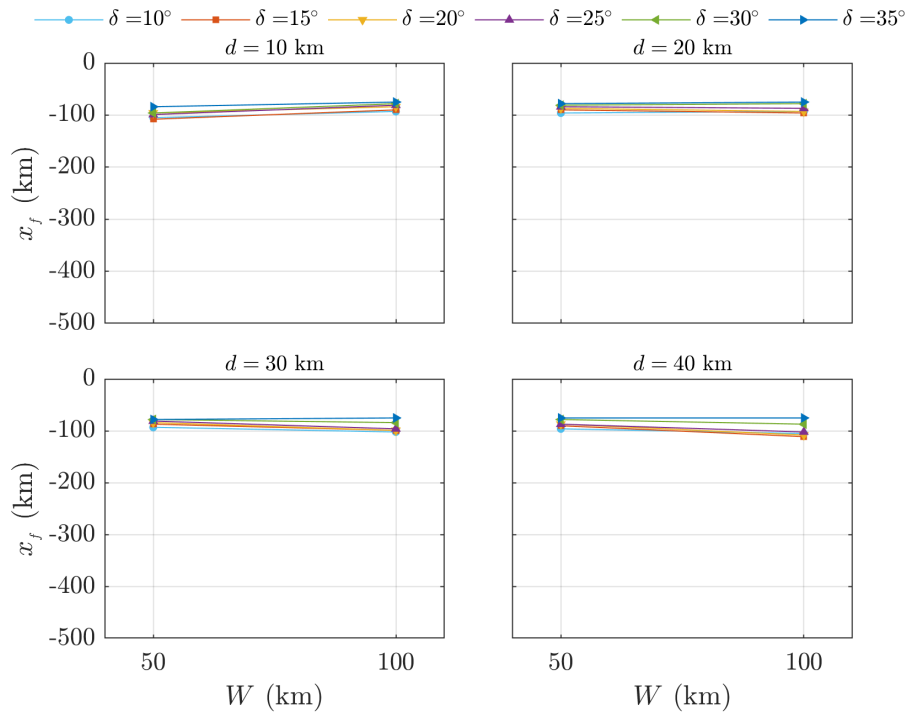


Figure 3.42: Relation of the focusing distance to the fault width. The fault length is  $L = 200$  km and the slip amount  $u = 10$  m.

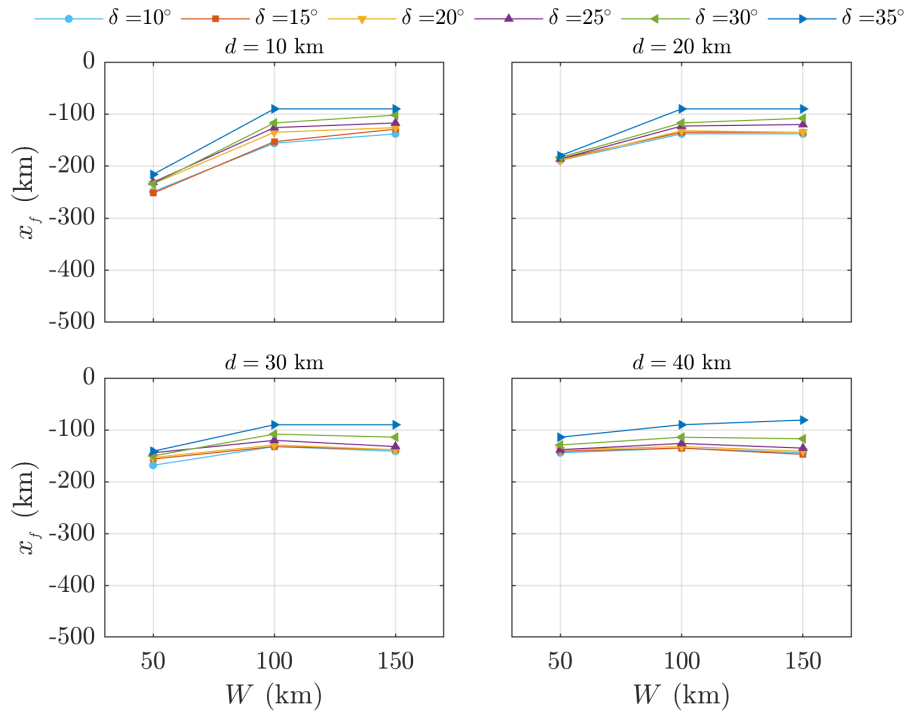


Figure 3.43: Relation of the focusing distance to the fault width. The fault length is  $L = 300$  km and the slip amount  $u = 10$  m.

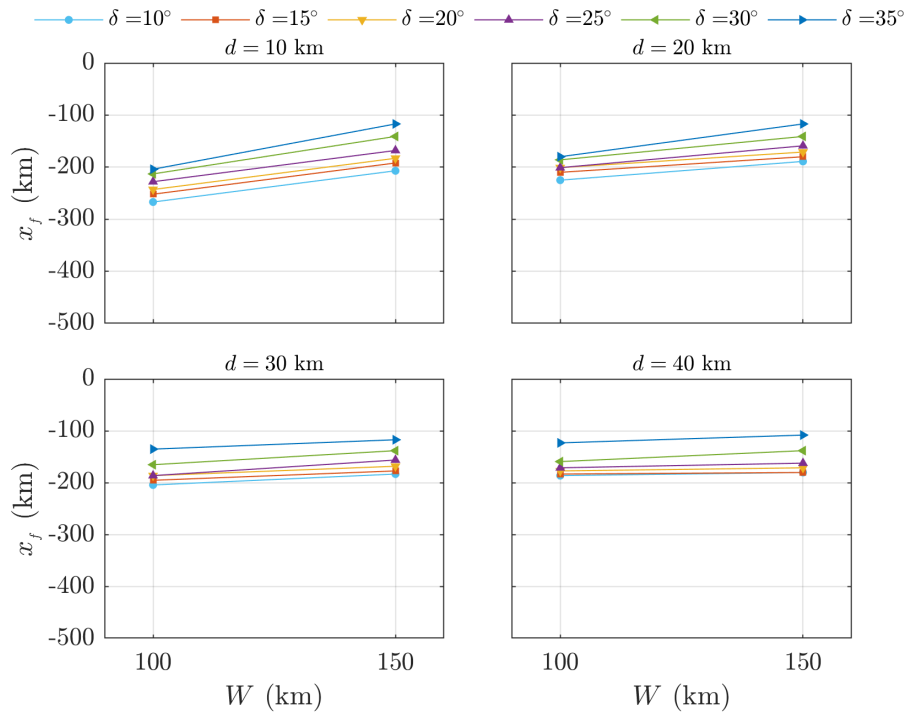


Figure 3.44: Relation of the focusing distance to the fault width. The fault length is  $L = 400$  km and the slip amount  $u = 10$  m.

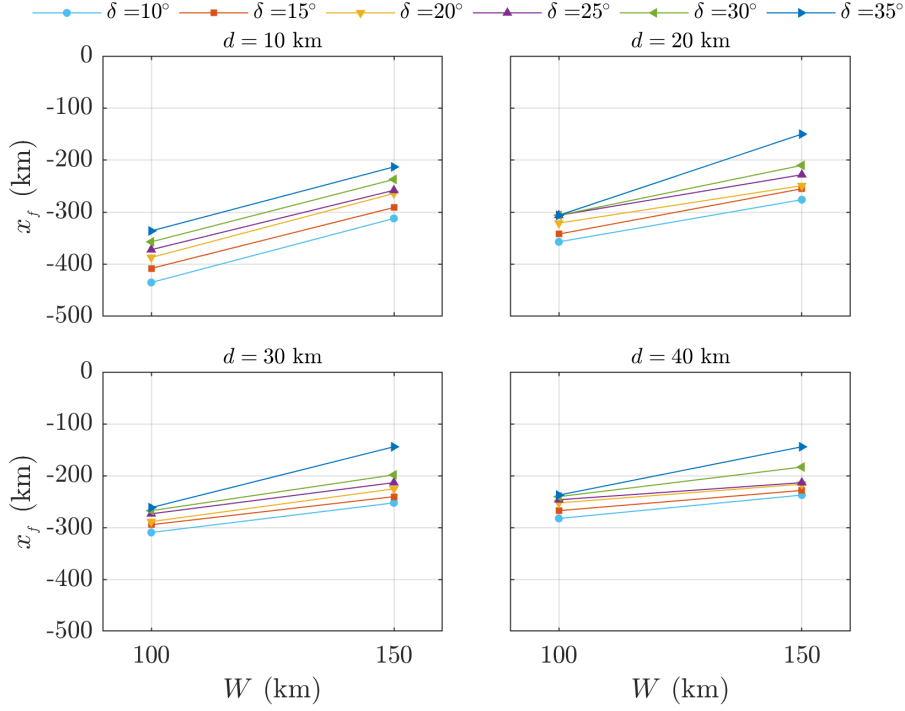


Figure 3.45: Relation of the focusing distance to the fault width. The fault length is  $L = 500$  km and the slip amount  $u = 10$  m.

### 3.4.6 Focusing through the tsunami aspect ratio

The relationship of focusing amplitude to the tsunami aspect ratio ( $L/W$ ) for different source combinations of the fault width, fault depth, and dip angle is shown in Figure 3.46, where focusing amplitude rises by increasing the tsunami aspect ratio.

The focusing distance ( $|x_f|$ ) increases by increasing the tsunami aspect ratio (Figure 3.47). Consequently, the focusing point gets farther from the source region; especially for much-elongated sources, the focusing distance increases significantly, translating to the focusing point reaching closer to the coastline and potentially generating destructive tsunami waves in the coastal surroundings.



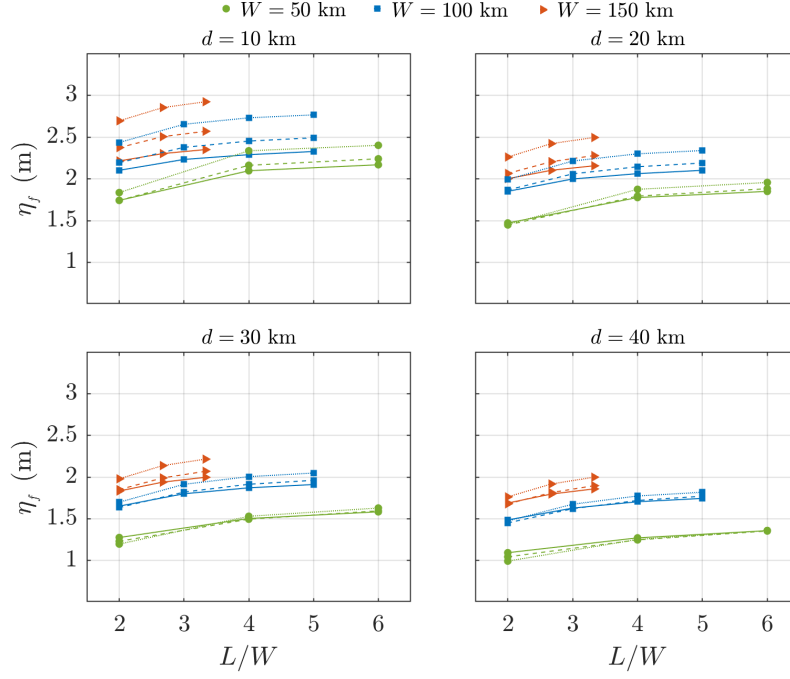


Figure 3.46: Relation of the focusing amplitude to the tsunami aspect ratio. The solid, dashed, and dotted lines indicate results for  $\delta = 10, 20$ , and  $30^\circ$ , respectively. The slip amount  $u = 10$  m.

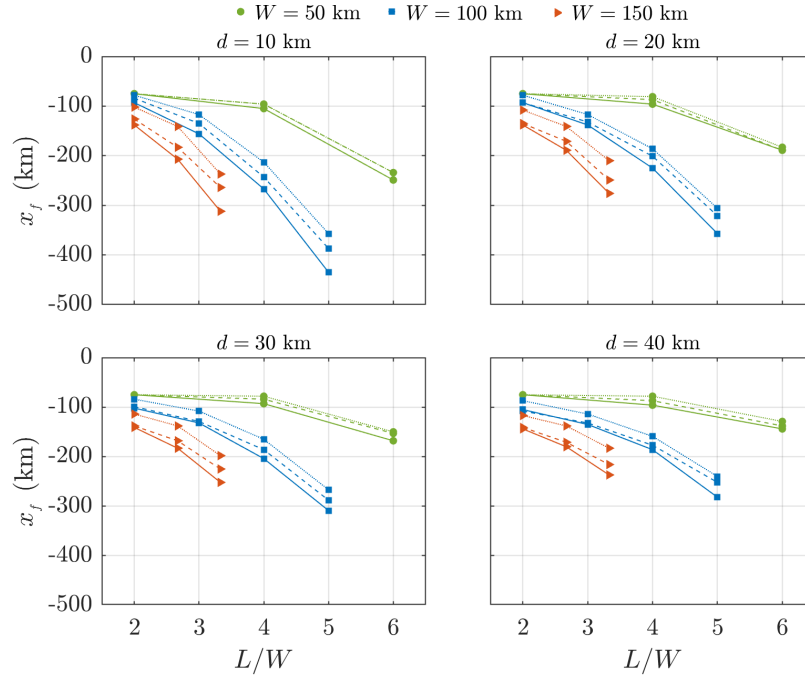


Figure 3.47: Relation of the focusing distance to the tsunami aspect ratio. The solid, dashed, and dotted lines indicate results for  $\delta = 10, 20$ , and  $30^\circ$ , respectively. The slip amount  $u = 10$  m.

To summarize the results, it can be stated that focusing amplitude linearly rises by increasing the slip amount. In contrast, focusing distance is not sensitive to the slip amount and remains constant for different slips. Focusing amplitude almost linearly decreases for deeper faults. However, the focusing distance is not much sensitive to the fault depth except in the case of the tsunami source with large aspect ratios. Focusing amplitude can experience a slight rise by increasing the dip angle. Nevertheless, focusing distance undergoes a decrease by increasing the dip angle. Focusing amplitude grows slightly by expanding the fault length to a certain amount, then remains almost constant. On the other hand, by increasing the fault length, the focusing point moves away from the tsunami source, corresponding to an increase in focusing distance. About the relationship of the fault width to the focusing, it can be noted that focusing amplitude increases by extending the fault width; further, for elongated earthquake sources, the focusing distance tends to decrease by extending the fault width. Last, focusing amplitude rises by increasing the tsunami aspect ratio; moreover, focusing distance increases by extending the tsunami aspect ratio, especially for much-elongated sources focusing distance increases significantly. In addition, it can be stated that focusing amplitude is mostly affected by the slip amount and the fault depth; further, focusing distance depends mainly on the fault length (tsunami crest length) and the aspect ratio.

Finally, it would be remarked that the wave model used in this chapter neglects the effects of bathymetric change, which nevertheless can be computed since Berry (2007). In addition, nonlinearity and dispersion are neglected in this study; however, Kânoğlu et al. (2013) compared the role of four approximations of the governing equations of hydrodynamics, e.g., linear non-dispersive, linear dispersive, nonlinear non-dispersive, and weakly nonlinear weakly dispersive theories on tsunami focusing; and showed that the focusing points exist in tsunami evolution using all four approaches with almost indiscernible differences.

## CHAPTER 4

### CONCLUSIONS

In this study, first, the initial tsunami wave and the maximum runup are provided in terms of the earthquake source parameters; then, the effects of the earthquake source parameters on the unique behavior, i.e., focusing, of leading depression tsunami propagation are investigated.

Chapter 1 gives an introduction to the study and reviews related literature. In chapter 2, the generalized *N*-wave profile and maximum runup equations (Tadepalli & Synolakis 1996) are parameterized in terms of the earthquake source parameters; then, two asymptotic equations (one-dimensional NEP and REP), appropriate for calculating the nearshore tsunami initial profile and maximum runup, are proposed. The results are justified by comparing with the field measurements of 1992 Nicaragua, 1994 Indonesia, 1995 Mexico, 2004 Sumatra, 2010 Chile, 2011 Japan, and the 2020 Aegean Sea tsunamis. Consequently, this study confirms *N*-wave as a suitable model for geophysically realistic tsunamis. The study's approach can provide an urgent and quick estimation of the tsunami maximum runup height whenever the fault plane parameters of the tsunami source are available and can be used in tsunami early warning and forecasting. Nonetheless, NEP and REP provide results for canonical bathymetry and the complexity of the beach bathymetry is not considered. In addition, even though the earthquake fault plane parameters are reasonably varied in the fitting processes to cover the most probable earthquake scenarios, formulas should not be used where the earthquake fault plane parameters are outside the range of the fitting database. Otherwise, NEP can not properly fit Okada's profile; consequently, the maximum runup calculated by REP may not be acceptable. The approach can provide a helpful tsunami forecast, especially where the high-resolution terrain data are unavailable,

and a quick early warning must be performed. Even though data are available, numerical modeling might be time-consuming and not fast enough in nearshore tsunami early warning if high-performance computer systems are not accessible.

Chapter 3 studies the tsunami focusing phenomenon. In this chapter, first, two-dimensional  $N$ -wave profile is provided in terms of the earthquake source parameters (two-dimensional NEP). Then, an analytical solution of linear shallow water-wave equations over a constant depth ocean (Aydın 2011) is used, and the impacts of the fault plane parameters on the focusing of finite crest length  $N$ -wave profile (two-dimensional NEP) are illustrated. The earthquake source parameters' effects on the variation of amplitude and location of the focusing point can be summarized as follows: focusing amplitude rises linearly by increasing the slip amount. In contrast, focusing distance remains constant against the slip amount. Focusing amplitude almost linearly decreases for deeper faults. However, the focusing distance is not much sensitive to the fault depth except for the tsunami source with large aspect ratios. Focusing amplitude rises slightly by increasing the dip angle. Nevertheless, focusing distance experiences a decrease by increasing the dip angle. Focusing amplitude increases slightly by extending the fault length to a certain amount, then remains almost constant. On the other hand, by increasing the fault length, the focusing point moves away from the tsunami source region, corresponding to an increase in focusing distance. Focusing amplitude increases by expanding the fault width; further, for elongated earthquake sources, the focusing distance tends to decrease by expanding the fault width. Last, focusing amplitude rises by increasing the tsunami aspect ratio; moreover, focusing distance increases by extending the tsunami aspect ratio, especially for much-elongated sources focusing distance increases significantly. Here, the results may explain some discrepancies encountered in the field runup observations.

Finally, it would be remarked that the results presented in this thesis can help not only estimate nearshore tsunami initial profile and maximum runup quickly and efficiently but also better understand the effects of the fault plane parameters on tsunami characteristics and coastal amplification.

## REFERENCES

- Abercrombie, R. E., Antolik, M., Felzer, K., & Ekström, G. (2001). The 1994 Java tsunami earthquake: slip over a subducting seamount. *Journal of Geophysical Research: Solid Earth*, 106, 6595–6607. doi:<https://doi.org/10.1029/2000JB900403>.
- Aydın, B. (2011). *Analytical solutions of shallow-water wave equations*. Ph.D. thesis Middle East Technical University Ankara, Türkiye.
- Aydın, B. (2018). Identifying the role of initial wave parameters on tsunami focusing. *Acta Geophysica*, 66, 283–291.
- Aydın, B., & Kânoğlu, U. (2017). New analytical solution for nonlinear shallow water-wave equations. *Pure and Applied Geophysics*, 174, 3209–3218. doi:10.1007/s00024-017-1508-z.
- Aydın, B., Sharghivand, N., & Özge Bayazıtöğlu (2020). Potential tsunami hazard along the southern Turkish coast. *Coastal Engineering*, 158, 103696. doi:<https://doi.org/10.1016/j.coastaleng.2020.103696>.
- Baba, T., Takahashi, N., & Kaneda, Y. (2014). Near-field tsunami amplification factors in the Kii Peninsula, Japan for Dense Oceanfloor Network for Earthquakes and Tsunamis (DONET). *Marine Geophysical Research*, 35, 319–325. doi:10.1007/s11001-013-9189-1.
- Behrens, J., Løvholt, F., Jalayer, F., Lorito, S., Salgado-Gálvez, M. A., & Sørensen, M. (2022). *Assessing research gaps in probabilistic tsunami hazard and risk analysis*. Technical Report Copernicus Meetings.
- Ben-Menahem, A. (1961). Radiation of seismic surface-waves from finite moving sources. *Bulletin of the Seismological Society of America*, 51, 401–435.
- Ben-Menahem, A., & Rosenman, M. (1972). Amplitude patterns of tsunami waves

- from submarine earthquakes. *Journal of Geophysical Research (1896-1977)*, 77, 3097–3128. doi:<https://doi.org/10.1029/JB077i017p03097>.
- Berry, M. (2007). Focused tsunami waves. *Proceedings of the Royal Society A: Mathematical, Physical and Engineering Sciences*, 463, 3055–3071. doi:10.1098/rspa.2007.0051.
- Bestor, T. C. (2013). Disasters, natural and unnatural: reflections on March 11, 2011, and its aftermath. *The Journal of Asian Studies*, 72, 763–782.
- Borrero, J. C., Synolakis, C. E., & Fritz, H. (2006). Northern Sumatra field survey after the December 2004 great Sumatra earthquake and Indian Ocean tsunami. *Earthquake Spectra*, 22, 93–104. doi:10.1193/1.2206793.
- Carrier, G., & Greenspan, H. (1958). Water waves of finite amplitude on a sloping beach. *Journal of Fluid Mechanics*, 4, 97–109. doi:10.1017/S0022112058000331. Cited By 474.
- Davies, G., & Griffin, J. (2019). Sensitivity of probabilistic tsunami hazard assessment to far-field earthquake slip complexity and rigidity depth-dependence: case study of Australia. *Pure and Applied Geophysics*, 177, 1521–1548. doi:10.1007/s00024-019-02299-w.
- Dotsenko, S., Sergeevskii, B. Y., & Cherkesov, L. (1986). Spatial tsunami waves caused by a sign-changing displacement of the ocean surface. *Issledovanie Tsunami*, 1, 7–14. In Russian.
- Doğan, G. G., Yalçiner, A. C., Yüksel, Y., Ulutaş, E., Polat, O., Güler, I., Şahin, C., Tarih, A., & Kânoğlu, U. (2021). The 30 October 2020 Aegean Sea tsunami: Post-event field survey along Turkish coast. *Pure and Applied Geophysics*, 178, 785–812. doi:10.1007/s00024-021-02693-3.
- Duputel, Z., Rivera, L., Kanamori, H., & Hayes, G. (2012). W phase source inversion for moderate to large earthquakes (1990–2010). *Geophysical Journal International*, 189, 1125–1147. doi:10.1111/j.1365-246X.2012.05419.x.
- Dziewonski, A., Ekström, G., & Salganik, M. (1995). Centroid-moment tensor solutions for April–June 1994. *Physics of the Earth and Planetary Interiors*, 88, 69–78. doi:[https://doi.org/10.1016/0031-9201\(94\)03006-5](https://doi.org/10.1016/0031-9201(94)03006-5).

- Dziewonski, A., Ekström, G., & Salganik, M. (1997). Centroid-moment tensor solutions for October–December 1995. *Physics of the Earth and Planetary Interiors*, 101, 1–12. doi:[https://doi.org/10.1016/S0031-9201\(96\)03199-8](https://doi.org/10.1016/S0031-9201(96)03199-8).
- François, B. (2010). Okada: Surface deformation due to a finite rectangular source. Matlab code, MATLAB Central File Exchange.
- Fritz, H. M., Petroff, C. M., Catalán, P. A., Cienfuegos, R., Winckler, P., Kalligeris, N., Weiss, R., Barrientos, S. E., Meneses, G., Valderas-Bermejo, C., Ebeling, C., Papadopoulos, A., Contreras, M., Almar, R., Dominguez, J. C., & Synolakis, C. E. (2011). Field survey of the 27 February 2010 Chile tsunami. *Pure and Applied Geophysics*, 168, 1989–2010. doi:10.1007/s00024-011-0283-5.
- GEBCO (2020). GEBCO bathymetric compilation group 2020, the GEBCO 2020 grid - a continuous terrain model of the global oceans and land. <https://download.gebco.net/>. doi:10.5285/a29c5465-b138-234d-e053-6c86abc040b9 accessed April 2022.
- Glimsdal, S., Løvholt, F., Harbitz, C. B., Romano, F., Lorito, S., Orefice, S., Brizuela, B., Selva, J., Hoechner, A., Volpe, M. et al. (2019). A new approximate method for quantifying tsunami maximum inundation height probability. *Pure and Applied Geophysics*, 176, 3227–3246.
- González, F., Geist, E. L., Jaffe, B., Kânoğlu, U., Mofjeld, H., Synolakis, C., Titov, V. V., Arcas, D., Bellomo, D., Carlton, D. et al. (2009). Probabilistic tsunami hazard assessment at Seaside, Oregon, for near-and far-field seismic sources. *Journal of Geophysical Research: Oceans*, 114.
- González, F. I., Geist, E. L., Jaffe, B., Kânoğlu, U., Mofjeld, H., Synolakis, C. E., Titov, V. V., Arcas, D., Bellomo, D., Carlton, D., Horning, T., Johnson, J., Newman, J., Parsons, T., Peters, R., Peterson, C., Priest, G., Venturato, A., Weber, J., Wong, F., & Yalçiner, A. (2009). Probabilistic tsunami hazard assessment at Seaside, Oregon, for near- and far-field seismic sources. *Journal of Geophysical Research: Oceans*, 114. doi:10.1029/2008JC005132.
- Grezio, A., Babeyko, A., Baptista, M. A., Behrens, J., Costa, A., Davies, G., Geist,

- E. L., Glimsdal, S., González, F. I., Griffin, J., Harbitz, C. B., LeVeque, R. J., Lorito, S., Løvholt, F., Omira, R., Mueller, C., Paris, R., Parsons, T., Polet, J., Power, W., Selva, J., Sørensen, M. B., & Thio, H. K. (2017). Probabilistic tsunami hazard analysis: multiple sources and global applications. *Reviews of Geophysics*, 55, 1158–1198. doi:10.1002/2017RG000579.
- Gusiakov, V. (2009). Tsunami history: recorded. *The sea*, 15, 23–53.
- Harbitz, C. B., Nakamura, Y., Arikawa, T., Baykal, C., Doğan, G. G., Frauenfelder, R., Glimsdal, S., Guler, H. G., Issler, D., Kaiser, G., Kânoğlu, U., Kisacik, D., Kortenhaus, A., Løvholt, F., Maruyama, Y., Sassa, S., Sharghivand, N., Strusinska-Correia, A., Tarakcioglu, G. O., & Yalçiner, A. C. (2016). Risk assessment and design of prevention structures for enhanced tsunami disaster resilience (RAPSODI)/Euro-Japan collaboration. *Coastal Engineering Journal*, 58, 1640012–1–1640012–37. doi:10.1142/S057856341640012X.
- Imamura, F., & Imteaz, M. A. (1995). Long waves in two layers: governing equations and numerical model.
- Jaffe, B. E., Borrero, J. C., Prasetya, G. S., Peters, R., McAdoo, B., Gelfenbaum, G., Morton, R., Ruggiero, P., Higman, B., Dengler, L., Hidayat, R., Kingsley, E., Kongko, W., Lukijanto, Moore, A., Titov, V., & Yulianto, E. (2006). Northwest Sumatra and offshore islands field survey after the December 2004 Indian Ocean tsunami. *Earthquake Spectra*, 22, 105–135. doi:10.1193/1.2207724.
- Johnson, J. M. (1998). Heterogeneous coupling along alaska-aleutians as inferred from tsunami, seismic, and geodetic inversions. In *Advances in Geophysics* (pp. 1–116). Elsevier volume 39.
- Kanoglu, U. (2016). Tsunami Focusing and Leading Amplitude. In *AGU Fall Meeting Abstracts* (pp. NH41A–1742). volume 2016.
- Kânoğlu, U. (2004). Nonlinear evolution and runup-rundown of long waves over a sloping beach. *Journal of Fluid Mechanics*, 513, 363–372. doi:10.1017/S002211200400970X.
- Kânoğlu, U., Titov, V. V., Aydın, B., Moore, C., Stefanakis, T. S., Zhou, H., Spillane, M., & Synolakis, C. E. (2013). Focusing of long waves with finite crest over



- constant depth. *Proceedings of the Royal Society A-Mathematical Physical and Engineering Sciences*, 469. doi:10.1098/rspa.2013.0015.
- Kervella, Y., Dutykh, D., & Dias, F. (2007). Comparison between three-dimensional linear and nonlinear tsunami generation models. *Theoretical and computational fluid dynamics*, 21, 245–269.
- Koshimura, S., Imamura, F., & Shuto, N. (1999). Propagation of obliquely incident tsunamis on a slope part i: Amplification of tsunamis on a continental slope. *Coastal Engineering Journal*, 41, 151–164.
- Kânoğlu, U., Titov, V., Bernard, E., & Synolakis, C. (2015). Tsunamis: bridging science, engineering and society. *Philosophical Transactions of the Royal Society A: Mathematical, Physical and Engineering Sciences*, 373, 20140369. doi:10.1098/rsta.2014.0369.
- Lebreton, L. C. M., & Borrero, J. C. (2013). Modeling the transport and accumulation floating debris generated by the 11 March 2011 Tohoku tsunami. *Marine Pollution Bulletin*, 66, 53–58. doi:10.1016/j.marpolbul.2012.11.013.
- Liu, P. L.-F., Woo, S.-B., & Cho, Y.-S. (1998). Computer programs for tsunami propagation and inundation. *Cornell University*, 25.
- Løvholt, F., Griffin, J., & Salgado-Gálvez, M. (2016). Tsunami hazard and risk assessment on the global scale. In R. A. Meyers (Ed.), *Encyclopedia of Complexity and Systems Science* (pp. 1–34). Berlin, Heidelberg: Springer Berlin Heidelberg. doi:10.1007/978-3-642-27737-5\_642-1.
- Lynett, P. J., Borrero, J. C., Weiss, R., Son, S., Greer, D., & Renteria, W. (2012). Observations and modeling of tsunami-induced currents in ports and harbors. *Earth and Planetary Science Letters*, 327, 68–74. doi:10.1016/j.epsl.2012.02.002.
- Lynett, P. J., Gately, K., Wilson, R., Montoya, L., Arcas, D., Aytore, B., Bai, Y., Bricker, J. D., Castro, M. J., Cheung, K. F., David, C. G., Doğan, G. G., Escalante, C., González-Vida, J. M., Grilli, S. T., Heitmann, T. W., Horrillo, J., Kânoğlu, U., Kian, R., Kirby, J. T., Li, W., Macías, J., Nicolsky, D. J., Ortega, S., Pampell-Manis, A., Park, Y. S., Roeber, V., Sharghivand, N., Shelby,

- M., Shi, F., Tehranirad, B., Tolkova, E., Thio, H. K., Velioğlu, D., Yalçiner, A. C., Yamazaki, Y., Zaytsev, A., & Zhang, Y. (2017). Inter-model analysis of tsunami-induced coastal currents. *Ocean Modelling*, 114, 14 – 32. doi:<https://doi.org/10.1016/j.ocemod.2017.04.003>.
- Løvholt, F., Glimsdal, S., Harbitz, C. B., Zamora, N., Nadim, F., Peduzzi, P., Dao, H., & Smebye, H. (2012). Tsunami hazard and exposure on the global scale. *Earth-Science Reviews*, 110, 58 – 73. doi:<https://doi.org/10.1016/j.earscirev.2011.10.002>.
- Madsen, P. A., & Schäffer, H. A. (2010). Analytical solutions for tsunami runup on a plane beach: single waves, N-waves and transient waves. *Journal of Fluid Mechanics*, 645, 27–57. doi:10.1017/S0022112009992485.
- Mansinha, L., & Smylie, D. (1971). The displacement fields of inclined faults. *Bulletin of the Seismological Society of America*, 61, 1433–1440.
- Maramai, A., & Tinti, S. (1997). The 3 June 1994 Java tsunami: A post-event survey of the coastal effects. *Natural Hazards*, (pp. 31–49). doi:10.1023/A:1007957224367.
- Marchuk, A., & Titov, V. (1989). Source configuration and the process of tsunami waves forming. (pp. 11–17). In: Gusiakov VK (ed) Tsunamis: their science and hazard mitigation, Proceedings of international tsunami symposium. Novosibirsk, USSR.
- Mendoza, C., & Hartzell, S. (1999). Fault-slip distribution of the 1995 Colima-Jalisco, Mexico, earthquake. *Bulletin of the Seismological Society of America*, 89, 1338–1344.
- Miranda, J., & Luis, J. (2019). NSWING (non-linear shallow water model with nested grids), instituto dom luiz.
- Miranda, J., Luis, J., Reis, C., Omira, R., & Baptista, M. A. (2014). Validation of NSWING, a multi-core finite difference code for tsunami propagation and run-up. In *American Geophysical Union (AGU) fall meeting, San Francisco. Paper S21A-4390*.

- Mori, N., Takahashi, T., Yasuda, T., & Yanagisawa, H. (2011). Survey of 2011 Tohoku earthquake tsunami inundation and run-up. *Geophysical Research Letters*, 38. doi:10.1029/2011GL049210.
- NGDC/WDS (2022). Global historical tsunami database. National Geophysical Data Center NOAA. doi:10.7289/V5PN93H7 accessed Feb 2022.
- Okada, Y. (1985). Surface deformation due to shear and tensile faults in a half-space. *Bulletin of the Seismological Society of America*, 75, 1135–1154.
- Okal, E., & Synolakis, C. (2004). Source discriminants for near-field tsunamis. *Geophysical Journal International*, 158, 899–912. doi:10.1111/j.1365-246x.2004.02347.x.
- Okal, E. A. (2003). Normal mode energetics for far-field tsunamis generated by dislocations and landslides. *Pure and Applied Geophysics*, 160, 2189–2221.
- Okal, E. A., & Synolakis, C. E. (2016). Sequencing of tsunami waves: why the first wave is not always the largest. *Geophysical Journal International*, 204, 719–735.
- Piatanesi, A., Tinti, S., & Gavagni, I. (1996). The slip distribution of the 1992 Nicaragua earthquake from tsunami run-up data. *Geophysical Research Letters*, 23, 37–40.
- Schlurmann, T., Kongko, W., Goseberg, N., Natawidjaja, D., & Sieh, K. (2010). Near-field tsunami hazard map Padang, West Sumatra: Utilizing high resolution geospatial data and reseasonable source scenarios. *Coastal Engineering*, 2.
- Sepúlveda, I., & Liu, P. L.-F. (2016). Estimating tsunami runup with fault plane parameters. *Coastal Engineering*, 112, 57 – 68. doi:https://doi.org/10.1016/j.coastaleng.2016.03.001.
- Sepúlveda, I., Liu, P. L.-F., & Grigoriu, M. (2019). Probabilistic tsunami hazard assessment in South China Sea with consideration of uncertain earthquake characteristics. *Journal of Geophysical Research: Solid Earth*, 124, 658–688. doi:10.1029/2018JB016620.
- Sharghivand, N. (2014). *Tsunami forecast modeling for Turkish coastlines*. Master's thesis Middle East Technical University Ankara, Türkiye.

- Sharghivand, N., & Kânoğlu, U. (2016). Relate the earthquake parameters to the maximum tsunami runup. In *EGU General Assembly Conference Abstracts* (pp. EPSC2016–14464). volume 18 of *EGU General Assembly Conference Abstracts*.
- Sharghivand, N., & Kânoğlu, U. (2017). Long wave maximum runup and propagation features with respect to earthquake source parameters. In *27th International Tsunami Symposium ITS 2017 Conference Abstracts*.
- Sipkin, S., Person, W., & Presgrave, B. (2000). Earthquake bulletins and catalogs at the usgs National Earthquake Information Center (NEIC). *IRIS Newsletter*, 2000, 2–4.
- Stein, S., & Okal, E. (2005). Speed and size of the Sumatra earthquake. *Nature*, 434, 581–582. doi:10.1038/434581a.
- Synolakis, C. (1986). *The runup of long waves*. Ph.D. thesis California Institute of Technology, Engineering and Applied Science Pasadena, California.
- Synolakis, C. (1987). The runup of solitary waves. *Journal of Fluid Mechanics*, 185, 523–545. doi:10.1017/S002211208700329X.
- Synolakis, C., & Kânoğlu, U. (2015). The fukushima accident was preventable. *Philosophical Transactions of the Royal Society A: Mathematical, Physical and Engineering Sciences*, 373, 20140379. doi:10.1098/rsta.2014.0379.
- Synolakis, C., Liu, P., Philip, H. A., Carrier, G., & Yeh, H. (1997). Tsunamigenic sea-floor deformations. *Science*, 278, 598–600.
- Synolakis, C. E., & Bernard, E. N. (2006). Tsunami science before and beyond Boxing Day 2004. *Philosophical Transactions of the Royal Society A-Mathematical Physical and Engineering Sciences*, 364, 2231–2265. doi:10.1098/rsta.2006.1824. Discussion Meeting on Extreme Natural Hazards, Royal Soc, London, England, Oct 26-27, 2005.
- Synolakis, C. E., & Kong, L. (2006). Runup measurements of the December 2004 Indian Ocean Tsunami. *Earthquake Spectra*, 22, S67–S91. doi:10.1193/1.2218371.

- Tadepalli, S., & Synolakis, C. (1994). The run-up of N-waves on sloping beaches. *Proceedings of the Royal Society-Mathematical and Physical Sciences*, 445, 99–112. doi:10.1098/rspa.1994.0050.
- Tadepalli, S., & Synolakis, C. (1996). Model for the leading waves of tsunamis. *Physical Review Letters*, 77, 2141–2144. doi:10.1103/PhysRevLett.77.2141.
- Tang, L., Titov, V. V., Bernard, E. N., Wei, Y., Chamberlin, C. D., Newman, J. C., Mofjeld, H. O., Arcas, D., Eble, M. C., Moore, C. et al. (2012). Direct energy estimation of the 2011 Japan tsunami using deep-ocean pressure measurements. *Journal of Geophysical Research: Oceans*, 117.
- Tinti, S., & Tonini, R. (2013). The UBO-TSUFDF tsunami inundation model: validation and application to a tsunami case study focused on the city of Catania, Italy. *Natural Hazards and Earth System Sciences (NHESS)*, .
- Titov, V., Kânoğlu, U., & Synolakis, C. (2016). Development of MOST for real-time tsunami forecasting. *Journal of Waterway, Port, Coastal, and Ocean Engineering*, 142, 03116004. doi:10.1061/(ASCE)WW.1943-5460.0000357.
- Titov, V., Moore, C., Greenslade, D., Pattiaratchi, C., Badal, R., Synolakis, C., & Kânoğlu, U. (2011). A new tool for inundation modeling: Community modeling interface for tsunamis (commit). *Pure and Applied Geophysics*, 168, 2121–2131.
- Titov, V., Rabinovich, A. B., Mofjeld, H. O., Thomson, R. E., & González, F. I. (2005). The global reach of the 26 December 2004 Sumatra tsunami. *Science*, 309, 2045–2048.
- Tsuji, Y., Namegaya, Y., Matsumoto, H., Iwasaki, S.-I., Kanbua, W., Sriwichai, M., & Meesuk, V. (2006). The 2004 indian tsunami in thailand: Surveyed runup heights and tide gauge records. *Earth, Planets and Space*, 58, 223–232. doi:10.1186/BF03353382.
- Walsh, T. J., Titov, V. V., Venturato, A. J., Mofjeld, H. O., & Gonzalez, F. I. (2004). Tsunami hazard map of the Bellingham area, Washington: Modeled tsunami inundation from a Cascadia subduction zone earthquake. *Washington Division of Geology and Earth Resources Open File Report*, 15, 36.

- Wronna, M., Baptista, M. A., & Kânoğlu, U. (2021). A new tsunami runup predictor. *Natural Hazards*, 105, 1571–1585.
- Yalçiner, A. C., Suzen, M. L., Enginar, D. T., Doğan, G. G., Kolat, C., Celikbas, B., Yalçiner, B., Cabuk, O., Bas, M., Kilic, O., Mentese, E. Y., Tarih, A., Zaytsev, A., & Pelinovski, E. (2019). Complete tsunami hazard assessment, vulnerability and risk analysis for the Marmara coast of Istanbul metropolitan area. *Geophysical Research Abstracts*, 21, 1.
- Zaytsev, A., Kurkin, A., Pelinovsky, E., & Yalçiner, A. C. (2019). Numerical tsunami model nami-dance. *Science of Tsunami Hazards*, 38.
- Zhou, H., Moore, C., Wei, Y., & Titov, V. (2011). A nested-grid boussinesq-type approach to modelling dispersive propagation and runup of landslide-generated tsunamis. *Natural Hazards and Earth System Sciences*, 11, 2677–2697.

## **CURRICULUM VITAE**

### **PERSONAL INFORMATION**

Surname, Name: Sharghivand, Naeimeh

email: na.sharghivand@gmail.com

### **EDUCATION**

<b>Degree</b>	<b>Institution</b>	<b>Year of Graduation</b>
M.Sc.	Engineering Sciences Dept., METU	2014
B.Sc.	Computer Engineering Dept., IAUT	2006
High School	Sina	2000

### **LANGUAGE SKILLS**

Azeri (Mother Tongue)

Persian/Farsi (Native)

Turkish (Fluent)

English (Proficient)

## WORK EXPERIENCE

Year	Place	Enrollment
March 2017 - May 2021	Dolfen Consulting Engineering Co. Ankara, Türkiye	Coastal Hydro- dynamics Modeler, Project Coordinator
April 2017 - Dec 2017	Engineering Sciences Dept., METU TUBITAK R&D Project, No: 116Y462	Research Assistant
Aug 2015 - July 2016	Engineering Sciences Dept., METU ASTARTE/EU Project, No: 603839	Research Assistant
Nov 2013 - Jun 2015	Engineering Sciences Dept., METU RAPSEDI/Euro-Japan collaboration	Research Assistant
Oct 2011 - Sept 2013	Engineering Sciences Dept., METU TUBITAK R&D Project, No: 109Y387	Research Assistant
Feb 2007 - Aug 2010	SofTech Ltd. Computer Software Company, Tabriz, Iran	CEO, Owner

## PUBLICATIONS

### Journal Papers

**Sharghivand, N.,** Aydın, B., & Kânoğlu, U. (2022). Tsunami Focusing Mechanism through Earthquake Source Parameters. (*In preparation*)

**Sharghivand, N.,** & Kânoğlu, U. (2022). Tsunami Initial Profile and Maximum Runup through Earthquake Source Parameters. (*Submitted to Geophysical Journal International, reference: GJI-S-22-0636*)

Aydın, B., **Sharghivand, N.,** & Bayazitoğlu, Ö. (2020). Potential Tsunami Hazard



along the Southern Turkish Coast. *Coastal Engineering*, 158, 103696.

Lynett, P. J., Gately, K., Wilson, R., Montoya, L., Arcas, D., Aytore, B., Bai, Y., Bricker, J. D., Castro, M. J., Cheung, K. F., David, C. G., Doğan, G. G., Escalante, C., González-Vida, J. M., Grilli, S. T., Heitmann, T. W., Horrillo, J., Kânoğlu, U., Kian, R., Kirby, J. T., Li, W., Macías, J., Nicolsky, D. J., Ortega, S., Pampell-Manis, A., Park, Y. S., Roeber, V., **Sharghivand, N.**, Shelby, M., Shi, F., Tehranirad, B., Tolkova, E., Thio, H. K., Velioğlu, D., Yalçiner, A. C., Yamazaki, Y., Zaytsev, A., & Zhang, Y. (2017). Inter-model analysis of tsunami-induced coastal currents. *Ocean Modelling*, 114, 14 – 32.

Harbitz, C.B., Nakamura, Y., Arikawa, T., Baykal, C., Doğan, G.G., Frauenfelder, R., Glimsdal, S., Güler, H.G., Issler, D., Kaiser, G., Kânoğlu, U., Kisacik, D., Kortenhaus, A., Løvholt, F., Maruyama, Y., Sassa, S., **Sharghivand, N.**, Strusinska-Correia, A., Tarakcioglu Ozyurt, G., & Yalçiner, A.C. (2016). Risk Assessment and Design of Prevention Structures for Enhanced Tsunami Disaster Resilience (RAPSODI)/ Euro-Japan Collaboration. *Coastal Engineering Journal*, 58, 1640012–1–1640012–37.

### **International Conference Proceedings**

**Sharghivand, N.**, & Kânoğlu, U. (2021). Tsunami Maximum Runup and Focusing through Earthquake Source Parameters. *30th International Tsunami Symposium (ITS)*, July 1-3, Sendai, Tohoku, Japan.

Kânoğlu, U., & **Sharghivand, N.** (2019). N-wave Maximum Runup with Fault Plane Parameters. *American Geophysical Union (AGU) Fall Meeting*, Dec. 9-13, San Francisco, California, USA, abstract id. NH43F-1008

Aydın, B., Bayazitoğlu, Ö., **Sharghivand, N.**, & Kânoğlu, U. (2017). Preliminary Hazard Assessment for Tectonic Tsunamis in the Eastern Mediterranean. *American Geophysical Union (AGU), Fall Meeting Dec. 11-15, New Orleans, Louisiana, USA*, abstract #NH23A-0194.

**Sharghivand, N.**, & Kânoğlu, U. (2017). Long Wave Maximum Runup and Propagation Features with Respect to Earthquake Source Parameters. *International Tsunami*

*Symposium (ITS), Aug. 21-25, Bali- Flores, Indonesia.*

**Sharghivand, N.** (2016). Tsunami Propagation Database Application for the Aegean Coastlines. *14th Estuarine and Coastal Modeling Conference (ECM14), Jun. 13-15, University of Rhode Island, Kingston, RI, USA.*

**Sharghivand, N., & Kânoğlu, U.** (2016). Earthquake Parameters and *N*-Wave Runup. *35th International Conference on Coastal Engineering, Nov. 17-20, Antalya, Türkiye.*

**Sharghivand, N., & Kânoğlu, U.** (2016). Relate the Earthquake Parameters to the Maximum Tsunami Runup. *European Geosciences Union General Assembly, Apr. 17–22, Vienna, Austria, abstracts Vol. 18, EGU2016-14464-1.*

**Sharghivand, N., & Kânoğlu, U.** (2015). Benchmarking on Tsunami Currents with ComMIT. *American Geophysical Union (AGU) Fall Meeting, Dec. 14-18, San Francisco, California, USA, abstract id. NH23A-1852.*

**Sharghivand, N., & Kânoğlu, U.** (2015). Tsunami Forecast Modeling Development for Turkish Coastlines. *26th International Union of Geodesy and Geophysics (IUGG) Jun. 22- Jul. 2, Prague, Czech Republic.*

Yalçiner, A. C., Zaytsev, A., Kânoğlu, U., Velioğlu, D., Doğan, G., Kian, R., **Sharghivand, N., & Aytore, B.** (2015). NAMI DANCE Benchmark Results. *NTHMP Mapping & Modelling Benchmarking Workshop: Tsunami Currents, Portland, Oregon, U.S.*

Kânoğlu, U., **Sharghivand, N.,** Kalligeris, N., Flouri, E., Hoto, O., Dougalis, VA., & Synolakis, C. (2014). Capacity Building in Tsunami Modeling for the Aegean Sea Shorelines. *34th International Conference on Coastal Engineering, Jun. 15-20, Seoul, Korea.*

Dougalis, VA., Flouri, E., Kalligeris, N., Oğuz, H., **Sharghivand, N.,** Kânoğlu, U., & Synolakis, CE. (2013). Tsunami Propagation Database in the Aegean Sea. *International Tsunami Symposium, Sept. 25-28, Göcek, Türkiye, and Rhodes Greece.*

## **National Conference Proceedings**

Bayazitoğlu, Ö., Aydın, B., **Sharghivand, N.**, & Kânoğlu, U. (2018). Investigation of Tsunami Hazard in the Eastern Mediterranean Region. *9th Coastal Engineering Symposium, Nov. 1-3, Adana, Turkey. (In Turkish)*

Güler, H. G., Işık, E., **Sharghivand, N.**, Baykal, C., Güler, I., Ergin, A. (2018). Evaluation of the Performance of SWASH Numerical Model for the Regular Waves. *9th Coastal Engineering Symposium, Nov. 1-3, Adana, Turkey. (In Turkish)*

**Sharghivand, N.**, & Kânoğlu, U. (2014). Tsunami Forecast Modeling for Turkish Coastlines. *8th Coastal Engineering Symposium, Nov. 7-8, Istanbul, Turkey. (Full paper in Turkish)*

## **Google Scholar Link**

<https://scholar.google.com/citations?user=cU-hZGEAAAAJ&hl=en>